Back-analysis of the 1756 Tjellefonna rockslide, Langfjorden

Gro Sandøy

NTNU
Det skapende universitet

MASTERKONTRAKT
- uttak av masteroppgave

1. Studentens personalia

Etternavn, fornavn	Fødselsdato
Sandøy, Gro	**05. jul 1986**
E-post	Telefon
	97154127

2. Studieopplysninger

Fakultet	
Fakultet for Ingeniørvitenskap og teknologi	
Institutt	
Institutt for geologi og bergteknikk	
Studieprogram	Studieretning
Geofag og petroleumsteknologi	**Ingeniørgeologi og bergteknikk**

3. Masteroppgave

Oppstartsdato	Innleveringsfrist
10. jan 2012	**10. jun 2012**

Oppgavens (foreløpige) tittel
Volumberegning og numerisk modellering av Tjellefonnaskredet, Langfjorden

Oppgavetekst/Problembeskrivelse
This master assignment is representing a follow-up of the project work conducted by the candidate during the autumn semester 2011, where geological mapping and characterization of Tjellefonna slide area and nearby rock slopes were done. The master work is to cover volume estimation and stability analysis of the Tjellefonna rock slide, with particular focus on:
• Reconstruction of original, pre-event topography and volume estimation of the rock slide based on onshore data and bathymetry/seismic data of the sea floor close to the slide area.
• Mapping of necessary field data (JRC, JCS) for estimating the shear strength of discontinuities.
• Numerical modeling based on Phase2, including sensitivity tests for the different model input parameters and supplemented by other numerical models (UDEC for example) if required and if time permits.
• Analysis of potential trigging factors for the 1756 Tjellefonna slide.
The master project is organized in co-operation with NGU, with Thierry Oppikofer as contact person and external co-supervisor.

Hovedveileder ved institutt	Medveileder(e) ved institutt
Professor Bjørn Nilsen	
Ekstern bedrift/institusjon	Ekstern veileder ved bedrift/instutisjon
NGU	**Thierry Oppikofer**
Merknader	
1 uke ekstra p.g.a påske.	

4. Underskrift

Student: Jeg erklærer herved at jeg har satt meg inn i gjeldende bestemmelser for mastergradsstudiet og at jeg oppfyller kravene for adgang til å påbegynne oppgaven, herunder eventuelle praksiskrav.

Partene er gjort kjent med avtalens vilkår, samt kapitlene i studiehåndboken om generelle regler og aktuell studieplan for masterstudiet.

13.01.2012
....
Sted og dato

Gro Sandøy
....
Student

....
Hovedveileder

Abstract

The 22nd of February 1756 the largest historically recorded rockslide in Norway took place at Tjelle in Langfjorden, Møre & Romsdal County. Three displacement waves of up to 50 meters were created in Langfjorden by the impact of the failed rock mass constituting the Tjellefonna rockslide. A total of 32 people were killed, and 168 houses and 196 boats around the fjord were destroyed.

This thesis is continuation of a project assessment carried out in 2011, and comprises a back-analysis of the Tjellefonna rockslide. The ante-rockslide topography (ART) is reconstructed and a detailed volume calculation of the rockslide is carried out using two modern techniques: the Slope Local Base Level (SLBL) and a manual ART reconstruction in the PolyWorks software. The reconstructed pre-rockslide topography is then used in the 2D numerical modelling software Phase^2, for a detailed study of the parameters and trigger factors that affected the slope stability.

The volume of the deposits (on- and offshore) is calculated to be around 11 million m^3, giving an initial volume of the rockslide between 9 to 10 million m^3. This is less than the earlier calculations of 12 to 15 million m^3, and could have consequences for previous rockslide-generated tsunami modelling (e.g. for the Åknes rock slope).

The Phase^2 analyses include shear strength reduction (SSR) investigations and sensitive parameter tests. It is demonstrated that the failure of the Tjellefonna slope must have required strain softening in combination with triggering factors, where high groundwater is an essential feature. Earthquake, on the other hand, is ruled out as a triggering factor. Additionally, the analyses show that a sub-horizontal structure is critical in order to induce slope instability. This could be represented either by the J5 joint set or an observed sub-horizontal fault, although fieldwork and modelling indicates that the fault is the most important.

The sliding surface has been evaluated using the Phase^2 and SLBL results. It is concluded that the Tjellefonna rockslide was not composed of a uniform plane, but of a complex surface consisting of joints, faults, foliation and intact rock bridges. Moreover, it is obvious that the Tjellefonna failure was closely related to the tectonic deformation of the rocks in this area. The failure was likely also a consequence of progressive accumulation of rock weakening (strain softening), acting to degrade the equilibrium state of the slope. This could have generated a hillside creep explaining the growing tension cracks observed at the present crown prior to the rockslide.

Sammendrag

Norges største historiske fjellskred fant sted 22. februar 1756 på Tjelle ved Langfjorden, Møre & Romsdal. Fjellskredet, som går under navnet Tjellefonna, utløste totalt tre flodbølger på opptil 50 meter, som slo innover Langfjorden. I alt ble 32 mennesker drept, samt 168 hus og 196 båter rundt fjorden ble ødelagt.

Denne masteroppgaven er en oppfølgning av fordypningsprosjektet fullført i 2011, og inneholder en tilbake-analyse av fjellskredet Tjellefonna. Det er utført en rekonstruksjon av topografien (ART) og en detaljert volumberegning ved hjelp av to moderne teknikker: Slope Local Base Level (SLBL) og ved en manuell rekonstruksjon i programmet PolyWorks. Den rekonstruerte topografien er videre brukt i en 2D numerisk modell i programvaren Phase^2, hvor det er utført detaljerte studier av parametere og utløsende faktorer som påvirker skråningsstabiliteten.

Avsetningens volum (land og i fjorden) er kalkulert til å være rundt 11 millioner m^3, som gir fjellskredet et opprinnelig volum på mellom 9 og 10 million m^3. Dette er mindre enn foregående estimater på rundt 12 til 15 millioner m^3, og kan ha konsekvenser for tidligere fjellskred-genererende tsunami modellering (f.eks. det ustabile Åknes fjellpartiet).

Phase^2 analysene er basert på "shear strain reduction" (SSR) og en sensitiv testing av parametere. Det er påvist at Tjellefonna må ha bestått av tøyningsavherding i kombinasjon av utløsende faktorer, hvor høyt grunnvann er en svært vesentlig komponent. Jordskjelv, på den andre siden, er utelukket som en utløsende årsak. I tillegg viser analysene at en sub-horisontal struktur er avgjørende for stabiliteten. Denne strukturen er representert som enten sprekkesett J5, eller en sub-horisontal forkastning, hvor felt observasjoner og modelleringer indikerer at forkastningen er viktigst.

Karakteren til glideplanet har blitt evaluert ved bruk av Phase^2 og SLBL resultatene. Det er konkludert med at Tjellefonna ikke var oppbygd av et uniformt plan, men heller av komplekse overflater bestående av sprekker, forkastninger, foliasjonen og intakte bergmasser ("rock bridges"). Dessuten er det tydelig at ustabiliteten til Tjellefonna var relatert til den tektoniske deformasjonen av bergmassene i området. Fjellskredet var også mest sannsynlig en konsekvens av progressiv akkumulasjon av svekkende faktorer (tøyningsavherding), som virket degraderende på skåningsstabiliteten. Dette ville ha generert krypbevegelser i skråningen, som forklarer de voksene tensjonssprekkene observert i tiden før fjellskredet.

Acknowledgments

This thesis is a part of my master degree study in engineering geology and applied rock mechanics at the Department of Geology and Mineral Resources Engineering, Norwegian University of Science and Technology (NTNU). My supervisor Bjørn Nilsen from NTNU, and co-supervisor Thierry Oppikofer from the Norwegian Geological Survey (NGU) helped to formulate the structure of this thesis. Oppikofer taught the techniques and software's for the reconstructions and volume estimations, while Nilsen helped with the numerical modelling.

I would first of all like to thank my co-supervisor Oppikofer for all the time he has devoted to give guidance, advice and reviews, showing a genuine interest in my thesis. Thanks for all of your knowledge and for the valuable feedbacks you have given me, lifting the quality of this master thesis. You have challenged me to expand my knowledge, and encouraged me to take things to the next level by learning new softwares and methods. Secondly, I would like to thank my supervisor Nilsen. I am very grateful for your advices and for the time you have used for discussions. I have always felt welcome to come to your office, anytime! Through lessons and fieldwork in the recent years you have encourage me to learn more.

Additionally, I would like to thank NGU for offering me a summer job (fieldwork) at Lyngen in 2010, which inspired me to learn more about large-scale rockslides. I am also grateful to Martina Böhme (NGU) who as given me advice regarding Phase^2 modelling, and always had time to answer my questions. Furthermore, I thank Tim Redfield (NGU) for the discussions with him, and for showing his curiosity in my work.

Thanks also to my boyfriend, Espen Torgersen, for his help to review this thesis. During this final year you have supported me around the clock, and challenged me to improve. Finally, this thesis would not be the same without my brother Torgeir and my parents for supporting me throughout these years. I would especially thank my brother, as he has guided me through my engineering study with advices, encouragements and inspiration.

Too all my fellow students, thanks for all good laughter and our time together!

Trondheim 31 May, 2012

Gro Sandøy

x

Contents

1.   Introduction

1.1. Tjellefonna – Norway's largest historical rockslide

The study object Tjellefonna is located between Molde and Sunndalen, in the municipality of Nesset in Møre & Romsdal County (Figure 1). On 22nd of February 1756 the largest historically recorded rockslide in Norway occurred at Tjelle creating displacement waves of around 40 - 50 meters in the Langfjorden (Jørstad, 1968; Morsing, 1756). A total of 32 people were killed, and 168 houses and 196 boats around the fjord were destroyed (Furseth, 2006a; Jørstad, 1968; Morsing, 1756).

Unstable rock slope failures represent a major geological hazard, which have caused destructive natural disasters in many parts of the world, also in Norway (Table 1).

Table 1: Some of the historic landslide disasters in the counties Møre & Romsdal (M&R) and Sogn & Fjordene (S&F), with related displacements waves (H_{DW}) and casualties (Jørstad, 1968; Røsjø, 2005) .

Year:	Location:	Volume [m^3]:	H_{DW} [m]:	Fatalities:
1731	Skafjellet S&F	> 0.1 x 10^6	30	17
1756	**Tjelle, M&R**	**9 x 10^6 **** ~ 15 x 10^6 *	**~ 40 – 50**	**32**
1905	Loen, S&F	0.5 x 10^6	40	61
1934	Tafjord, M&R	1.5 x 10^6	62	40
1936	Loen, S&F	1 x 10^6	74	74

* = calculated 1934, ** = re-calculated 2012

This type of large rock slope failures pose a significant geotechnical challenge because there is often a large degree of geological complexity as well as large volumes involved. In Norway unstable rock slopes are of especially high risk due to the possible secondary effects of landslide damming up of a valley or producing displacement waves (tsunami) if the debris hit a water body such as a fjord or a lake. A better understanding of these large slope failures is important in order to detect future rockslides and to mitigate the secondary effects of tsunami.

The Geological Survey of Norway (NGU) has created a geohazard database (Figure 1) containing historical avalanche events, both with and without generation of displacement waves (Blikra et al., 2006b). The historical event database covers more than 3000 landslides, and includes numerous large-scale events. The counties of Møre & Romsdal, Sogn & Fjordene and Troms clearly stands out in this database with a much larger frequency than the others. This is closely related to the high topographic relief related to the fjords and glacial valleys in these areas (Blikra et al., 2006b). NGU and Norwegian

Geotechnical Institute (NGI) have through historical sources carried out analyses of these records, and estimated a frequency of two to four large rockslide each century (Høst, 2006).
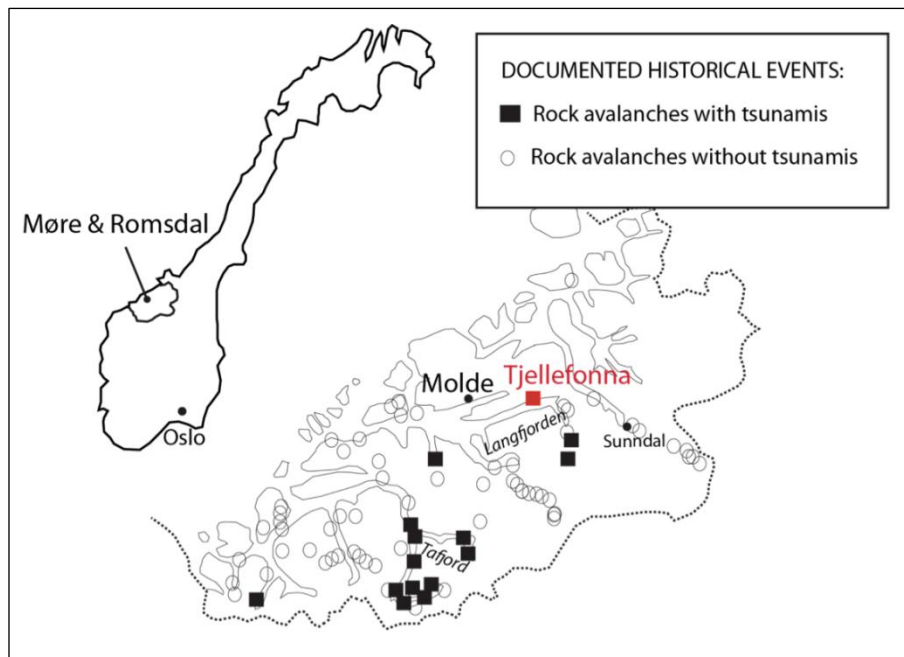
Figure 1: The location of Tjellefonna, Møre & Romsdal. The figure also gives an overview of historical rock avalanches with and without displacement waves (tsunamis). Figure is based on NGU – Geohazard database, and modified from Blikra et al. (2006b).

1.2. The aims of this thesis

This master thesis is a follow-up of the project work conducted during the autumn semester 2011, where geological mapping and characterization of Tjellefonna rock scar and nearby rock slopes were done (Sandøy, 2011b). This master thesis particularly focuses on a back-analysis of the Tjellefonna failure, and includes:

- Reconstruction of original, pre-event topography and volume estimation of the rockslide based on onshore data and bathymetry/seismic data of the sea floor close to the slide area.
- Mapping of necessary field data (JRC, JCS) for estimating the shear strength of discontinuities.
- Numerical modelling based on Phase^2, including sensitivity tests for the different model input parameters.
- Analysis of potential trigging factors for the 1756 Tjellefonna slide.

1.3. Available data

An overview of available data for this thesis is listed below with belonging sources:

Table 2: Available data for this master thesis.

Available data:	Sources:
• Project assessment about Tjellefonna: Includes an overview of geological factors affecting the slope stability and additional laboratory work.	(Sandøy, 2011b)
• Existing papers on Tjellefonna	(Redfield and Osmundsen, 2009; Redfield et al., 2011)
• Laboratory tests	(Sandøy, 2011a, b)
• Digital Terrain Model (DEM)	Statens kartverk
• Bathymetry	NGU

1.4. Previous work

An eyewitness, Christian Morsing (the Personel Capallen of the area) described the rockslide one year after the event. Morsing (1756) describes long sounds of heavy rumbles, and that the earth shivered. The shaking is defined to be particular strong near the fjord, where household objects were shaken down on the floor. Morsing describes this as an earthquake preceding the rockslide (Jørstad, 1968; Morsing, 1756). Immediately after the heavy rumble, the ocean raised and three following waves destroyed the littoral zone of Langfjorden, Eresfjorden and areas as far away as Gjermundnes (40 km from Tjelle) (Furseth, 2006a).

Captain Johan Chr. Von Richelieu defined the rockslide in more detailed in "Topografisk Journal" only 5 years after the event (but published 1784), and completed the first drawing of the Tjelle rockslide (Figure 2). The area where the initial failure took place had similar topography as the rest of the mountain-side (20 - 30°). There were also a mountain pasture at the top of the crag, which was described as flat and a quite good location to place farm houses (Svendsen and Werswick, 1961). Note also the dark lines crossing at mid-height in Figure 2, which may be a fault-like feature (Redfield et al., 2011).

Schøning (1778) describes a growing tension crack located at the mountain pasture. Additionally, a marsh located on the top of the mountain further add running water down the tension crack (Svendsen and Werswick, 1961). Prior to the rockslide there had been two weeks of heavy rainfall, and storm was building up on the day of the event (Furseth, 2006a).
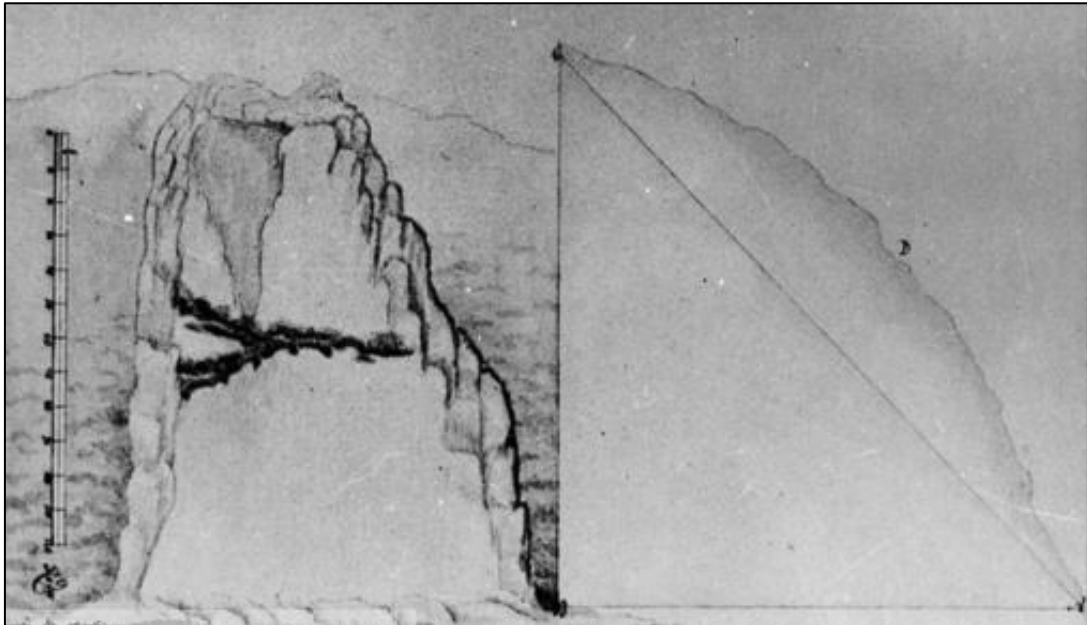
Figure 2: First drawing of the Tjelle landslide in 1761, by Captain Johan Chr. von Richelieu, Romsdalsmuseets fotoarkiv (Austrigard, 1976). Note the drawn dark lines crossing at mid-height, which may be a fault-like feature (Redfield et al., 2011).

Geologist Arne Bugge (NGU) did an inspection of the rockslide area in September 1934. Bugge evaluated Tjellefonna to cover an area of 600 x 250 meters, and being 100 meters high. This estimate give a total volume of about 15 million m^3 (Furseth, 2006b). Further, Bugge (1936) explains briefly the possible failure structures at Tjelle. Bugge proposes that Tjellefonna and Loen consist of similar structures; steep fracture sets that opened as tension crack downwards until they reached a large and less steep fracture-set with gouge material.

Jørstad (1965) from NGI, also conducted volume estimation in 1965. Jørstad evaluated the failure area to be 600 x 200 meters, with a height of around 100 meters. The new volume was calculated to be around 12 million m^3. The Tjellefonna fault system has been the focus of a study by Redfield and Osmundsen (2009). With this contribution they place the 1756 event within the framework of the tectonic and erosional development of the Norwegian passive margin. They speculate that an earthquake on a nearby fault may have caused the already weakened Tjelle slope to fail. Redfield and

Osmundsen (2009) have also looked briefly on the structural architecture of the slide scar combined with aerial photographs, Digital Elevation Model (DEM) and on-site field observation. They interpreted the Tjellefonna scar to represent the main hanging-wall damage zone of the Tjelle fault.

The Møre-Trøndelag Fault complex (MTFC) was also subject to an integrated study project by NGU, which ended in 2010. The project focused on imaging the MTFC at depth. This project was combined with two PhD students; Aziz Nasuti and Emil Lundberg.

Bauck (2010) carried out a master thesis with the title "Fault Rock Assemblages and Fault Architecture in The Møre-Trøndelag Fault Complex". The thesis presents detailed descriptions of fault architecture and brittle fault rocks along the Tjellefonna fault, and is a contribution to the MTFC project. Bauck has mapped and briefly described the Tjelle fault close to the back scarp, and proposes that the fault likely played an important role in the landslide release in 1756.

NGI has worked on modelling of the displacement waves from the Tjellefonna slide in the unpublished report of Harbitz et al. (2011). The report presents the final results from the numerical modelling on tsunamis generated from potential rockslides from Åknes and Hegguraksla in Storfjorden, Møre & Romsdal. In the report they also describe the historical rockslide event at Tjelle, to test the accuracy of the model. The rockslide dimensions are mainly determined by inspecting the bathymetries as well as the release areas. The used dimensions of Tjelle are a height of 60 meters (of deposits), a width of 500 meter and a length of 500 meters (volume of 15 million m^3). As a conclusion, the calculated waves close to the sliding area, as well as the inundation distance at Nesset Rectory, is close to that observed in 1756 (Figure 3).
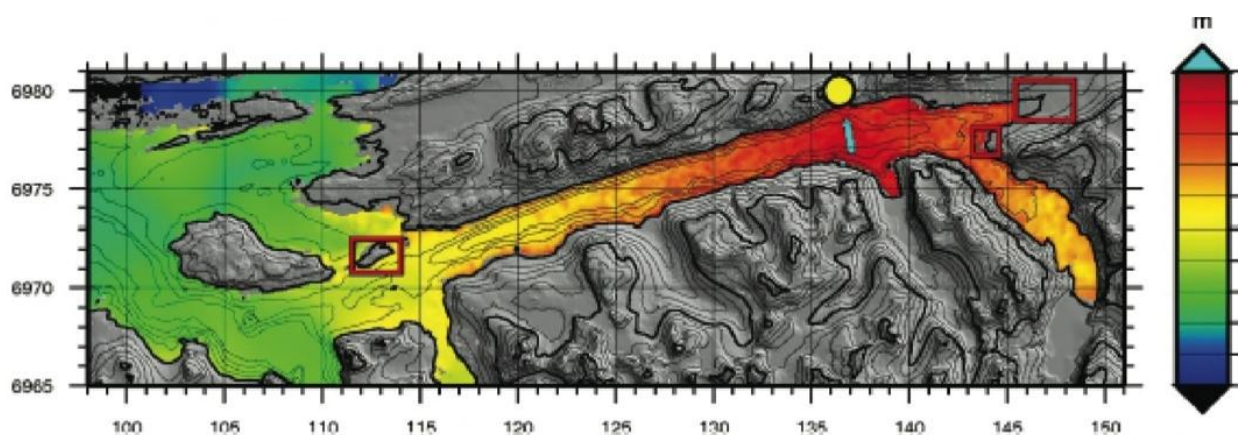

Figure 3: The result of the back-calculation of tsunami generated by the Tjellefonna rockslide (15 million m^3). The release area is marked with yellow, and the red rectangles are areas of run-up calculation (West to east: Veøy, Nesset Rectory and Eidsvågen (Harbitz et al., 2011)

1.4.1. Conclusions in the 2011 project assignment

The project assignment "Tjellefonna – Mapping of factors affecting slope stability" was completed in December 2011 (Sandøy, 2011b) at the Department of Geology and Mineral Resources Engineering, NTNU. The project was in co-operation with supervisor Professor Bjørn Nilsen (NTNU) and co-supervisor Thierry Oppikofer (NGU). The project presents detailed fieldwork, laboratory tests, Terrestrial Laser Scanning (TLS) data, bathymetry data, kinematic analysis and GIS analysis to get a better understand the factors affecting the rock slope stability at Tjellefonna.

Some of the main conclusions are listed below:

- Laboratory results reveal that the rock mass strength is high to very high for the granitic to granodioritic gneiss. It is obvious from the results that the rock mass has to be affected by other geological factors like joints, faults and folds, in order to failure take place.

- The foliation (155/69, 338/70), the faults and joint sets J1 (157/59) and J3 (352/47) are all sub-parallel to each other, as well as to the Langfjorden and the MTFC lineament. A combination of these structures makes up the back-scarp of the Tjellefonna crown. Lateral boundaries of the scarp are defined by joint set J2 (076/81), locally in combination with joint set J4 (211/88).

- Field investigations of the deposits show that the blocks have both undulating and planar surfaces. It is seen that where the foliation has been well developed the blocks have been separated along the banding. This shows that the foliation could act locally as a sliding surface. However, to create the large-scale Tjellefonna failure the combination of all structures appear to be the most important.

- The kinematic analyses illustrate that there are no clear failure mechanism (planar, toppling and/or wedge), even when using a low friction angle of 29° (fault gouge). This supports the theory that Tjellefonna is a complex failure, with several geological and possible non-geological factors affecting the stability.

2. Tectonic and geological setting

2.1. Western Gneiss Region (WGR)

The study area is situated in the Precambrian bedrock-province referred to as the Western Gneiss Region (WGR) (Figure 4). This region crops out west of the Caledonian nappe, and stretches from Sogn & Fjordane to Nord – Trøndelag county.
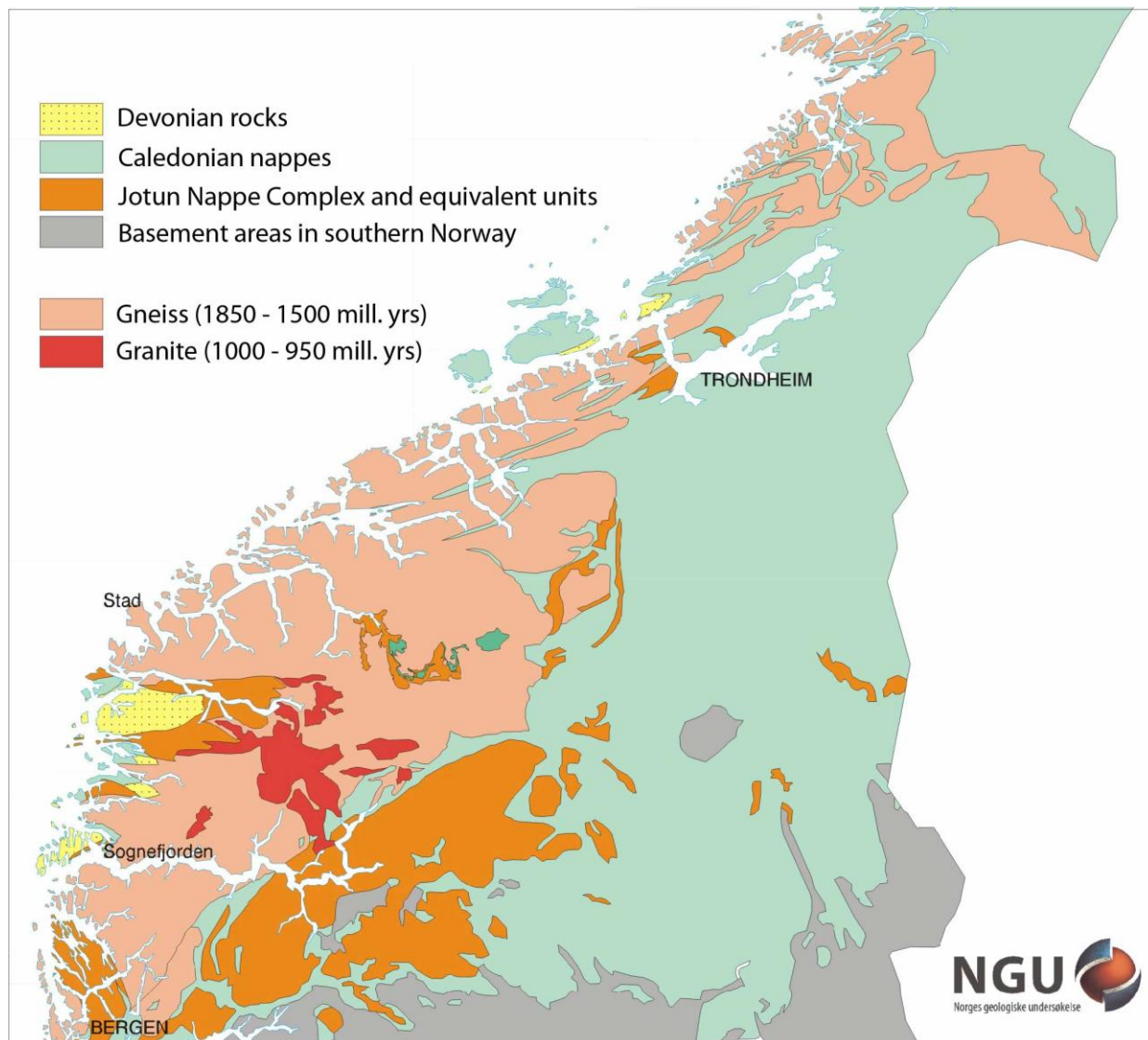

Figure 4: The map shows the distribution of rocks in the Western Gneiss Region (WGR). The major part of the WGR consists of granitic gneisses and migmatites developed between 1700 and 1500 million years ago. The Jotun Nappe Complex, and other Caledonian napes, overlies the gneisses. The map is draw by Arne Solli (Nordgulen and Andresen, 2007).

The major part of the WGR consists of granitic gneisses and migmatites formed about 1700 – 1500 Ma. The bedrock between Molde and the mouth of Trondheimsfjorden are dominated by gabbroid gneiss, granitic gneiss, migmatic gneiss and granite formed around 1686 – 1653 Ma. The rocks cropping out in the region south of Moldefjord – Romsdalen are influenced by the Sveconorwegian orogeny between 1200 and 900 Ma. The most important rock types in this region are various kinds of granitic gneisses and migmatites, which often have lenses and layers of micaceous gneisses and amphibolite (Nordgulen and Andresen, 2007).

Most of the geological structures seen in this region are a result of the Caledonian orogeny, with the collision between Laurentia and Baltica in the Silurian/Early Devonian times (Gee, 1975; Nordgulen and Andresen, 2007). During this event the Precambrian rocks along the western part of Baltica were forced down to great depths and underwent high-grade metamorphism (Nordgulen and Andresen, 2007).

Later in the Devonian and Early Carboniferous, the WGR was exhumed as a part of a megascale, late- to post-Caledonian extension or transtensional system (Andersen and Jamtveit, 1990; Krabbedam and Dewey, 1999). A number of NE-SW trending regional scale double plunging upright folds characterize the Western Gneiss Region (Redfield and Osmundsen, 2009). These are cut at a low angle by the Møre-Trøndelag Fault Complex (MTFC) (Figure 5) striking ENE – WSW (Watts, 2001).

2.2. Møre – Trøndelag Fault complex (MTFC)

An overview of the Møre – Trøndelag Fault Complex (MTFC) is shown in Figure 5. MTFC is a long – lived steeply dipping zone of fault-related deformation traced from Snåsa to Stadt (Watts, 2001). It consists of a ~ 50 km wide and ~ 300 km long penetrating fault section in a ENE – WSW trending direction (Saintot and Pascal, 2010; Watts, 2001). These faults stand out as several large fault strands, e.g. Tjellefonna, Hitra – Snåsa and Verran faults (Figure 5), that cut through the central parts of Norway (Grønlie and Roberts, 1989).

The fault zone is clearly seen on satellite photographs and digital elevation models as a set of NE – SW trending lineaments (Figure 5). This fault complex is one of several large fault zones that transgress to the shelf from the mainland, striking parallel to the coastline of Mid-Norway and separating the northern North Sea basin system from the deep Mesozoic Møre basin (Brekke, 2000).

The presence of mylonites, superimposed cataclasites, breccias and gouge reflect a long and complex evolution of the fault zones (Grønlie et al., 1991; Watts, 2001). The fault cores themselves are generally not exposed, and can often only by seen as lineaments. Because of this their true extent, dip direction and widths are not known (expect of Hitra-Snåsa and Verran fault) (Grønlie and Roberts, 1989).
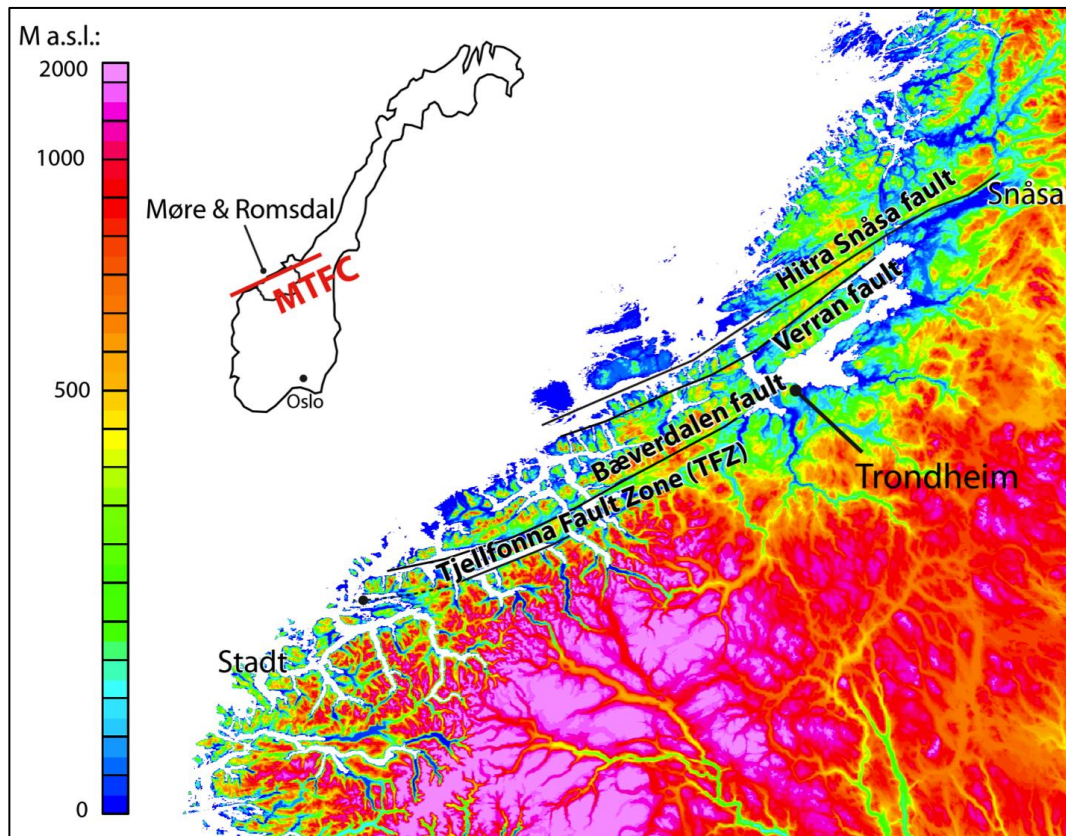
Figure 5: Map of the topography in central Norway, with proven and suggested fault strands of MFTC trending NW – ES. The figure illustrates how the relief is changing from the coastal area (green and blue colour) towards more alpine landscape inland (red and pink colour). The figure is modified from Redfield and Osmundsen (2009).

Saintot and Pascal (2010) recognized a steep, parallel and planar ENE – WSW striking ductile fabric that they attributed to the Caledonian deformation. Tight to open folds with axes trending ENE – WSW were also formed during this phase (Hacker et al., 2010). The structures have since been repeatedly reactivated by several periods of brittle faulting (Late Devonian/Early Carboniferous, Permo-Carboniferous, Post – Mid – Jurassic, Late Jurassic to Early/Late Cretaceous) (Watts, 2001). Previous work indicates that the steep fold flanks were consequently exploited to sinistral strike-slip in Devonian (Grønlie et al., 1991; Séranne, 1992; Watts, 2001), and normal dip slip in post-middle Jurassic times (Grønlie et al., 1994). The MTFC is still relatively active today, and appears to divide two regional stress fields (Pascal et al., 2010).

2.2.1. The Tjellefonna Fault Zone (TFZ) and Tjelle Fault

The topographic lineament strongly indicates the trace of the Tjellefonna Fault Zone (TFZ) along Langfjorden and northeast past Mulvik (Figure 5). Apatite fission-track (AFT) ages across the fault provide evidence for post Cretaceous normal-offset across the TFZ. Quaternary deposits and the sea (Langfjorden) cover the major trace of the Tjellefonna fault. However, several damage zones, which are interpreted to be related to the Tjellefonna fault, are exposed north of the main normal fault (Redfield and Osmundsen, 2009). One of these damage zones is called the Tjelle fault, which crops out in the back scarp of the Tjellfonna slide (Bauck, 2010).

The kinematics of the Tjelle Fault has been mapped by Bauck (2010). It is described as a steep south – dipping fault, which is sub-parallel to the main hillside gneissic foliation. The youngest lineations seem to indicate normal dip-slip movement. The Tjelle Fault is directly on strike with the more exposed normal fault at Rød, and may be a linked structure (Redfield et al., 2011).

2.3. Geological setting

Figure 6 gives an overview over mapped geological structures and rock types conducted by NGU. The northern side of Langfjorden, and the study object Tjellefonna is dominated by granitic to granodioritic gneiss. The map describes that the gneiss on the southern side is mainly quartzdioritic to granitic. The southern side also hosts bands of more amphibolitic layers (amphibolite, layered amphibolite, and amphibolite rich gneiss), "augengneiss", and more mica rich rocks (micaschist, micagneiss, and granite-mica schist). In general, the geological map shows that the area is characterized by uplifted high-grade metamorphic rocks.

Field mapping from Sandøy (2011b) revels that the bedrock at Tjelle consists of a generally medium-grained granitic to granodioritic gneiss. It is locally banded with mafic layers rich in biotite and amphibole, and felsic layers rich in quartz and feldspar (Figure 7A). In certain areas the bedrock is more fine-grained and very rich in amphibole, as shown in Figure 7B-C. From the geological map the foliation on the southern side of Langfjorden dips constantly to the south, in contrast to the northern side where the foliation is more complexly folded. Based on fieldwork carried out last year the gneiss is best described as a LS-tectonite, as it is both foliated and lineated (Figure 7E). Locally also pure L-tectonites were observed, in which the lineation is defined by rods of feldspars and amphiboles (Figure 7D). When

the banding/foliation is seen it is often folded into open to tight recumbent folds. The foliation varies between two mean directions of 155/69 and 338/70, changing between near-lying outcrops.
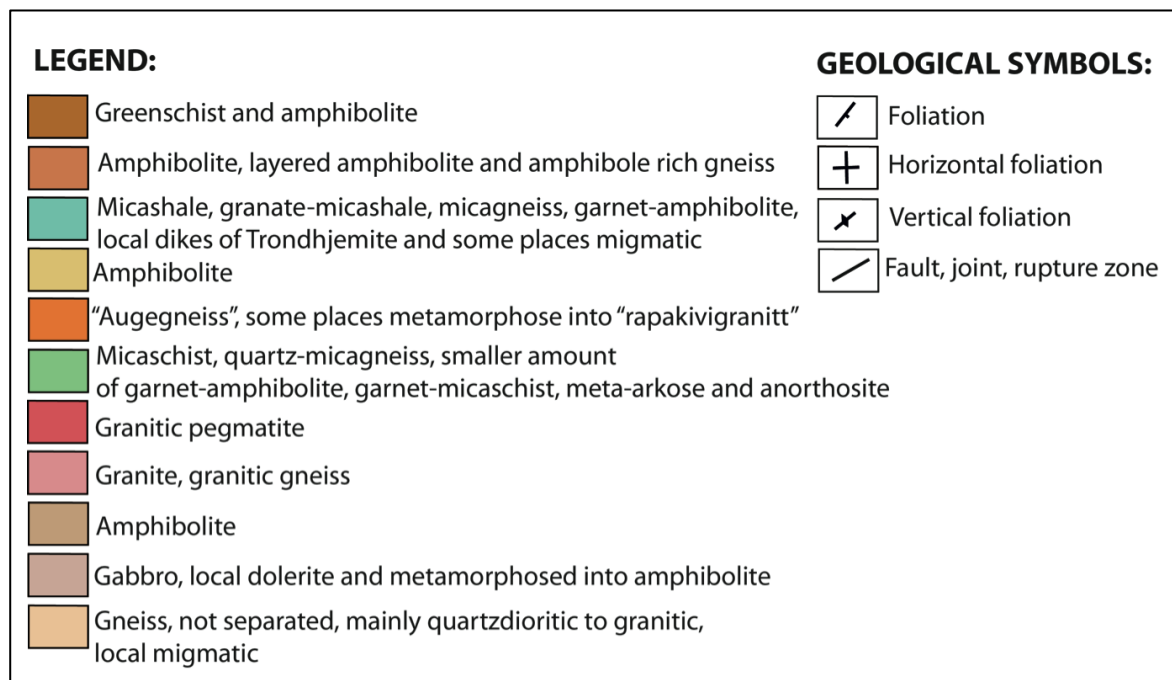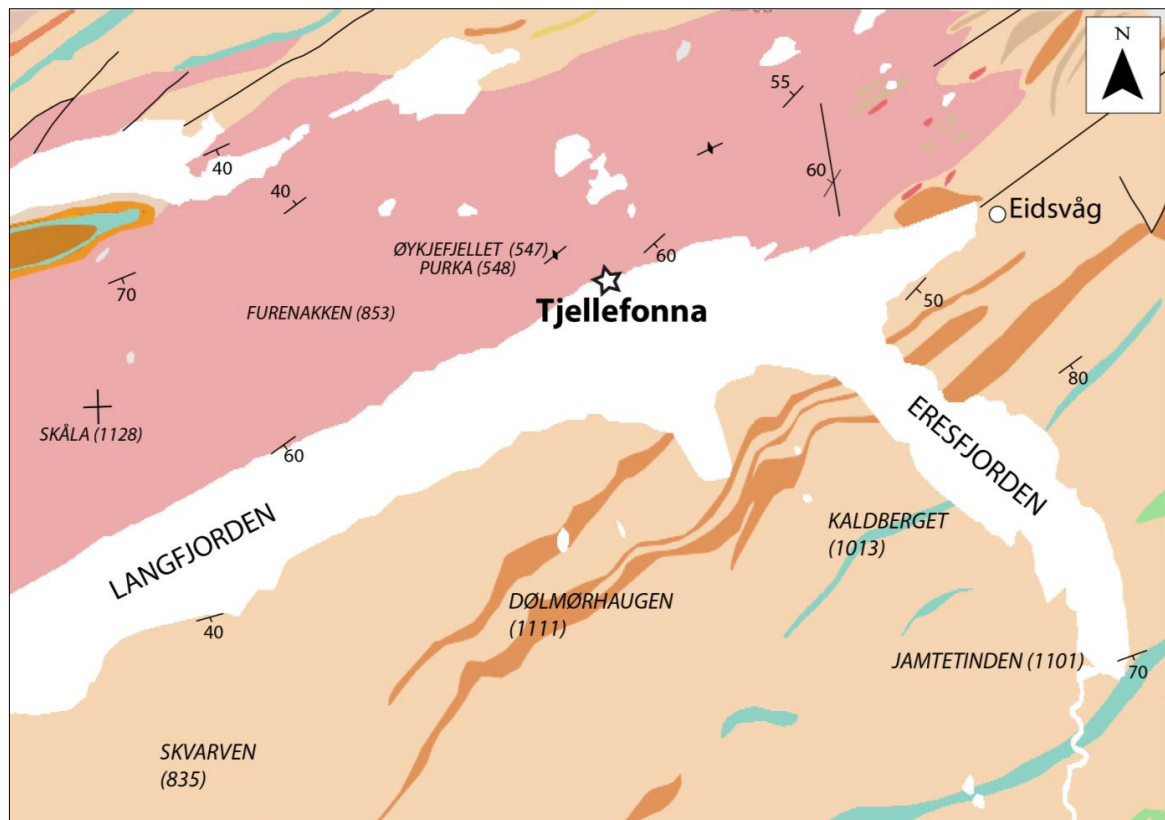
Figure 6: Geological map of Langfjorden modified by Lutro et al. (1996). The study object Tjellefonna is dominated by granitic to granodioritic gneiss

Figure 7: Observed lithologies at the Tjellefonna area; A) medium-grained granitic to granodioritic gneiss, B-C) gneiss more fine grained and rich in amphibole, D) in many places a mineral stretching lineation is more developed (L-tectonite) than the foliation, and E) observed also LS-tectonite, as it is both foliated and lineated. Figures are from Sandøy (2011b).

3. Site description

3.1. Topography

The topography of Langfjorden varies from an elevation of around 1000 m a.s.l. on the southern side to about 530 m a.s.l. at Purka. The Tjellefonna crown in located at around 380 m a.s.l (Figure 8). The Langfjorden makes up a sharp lineament that separates the coastal plains on the northern side from the alpine relief on the southern side (Etzelmüller et al., 2007). Nevertheless, on the northern side the altitude increases gradually towards south-west, with the highest mountain 'Skåla' (1128 m a.s.l.) located near Molde (Figure 6 and Figure 8).
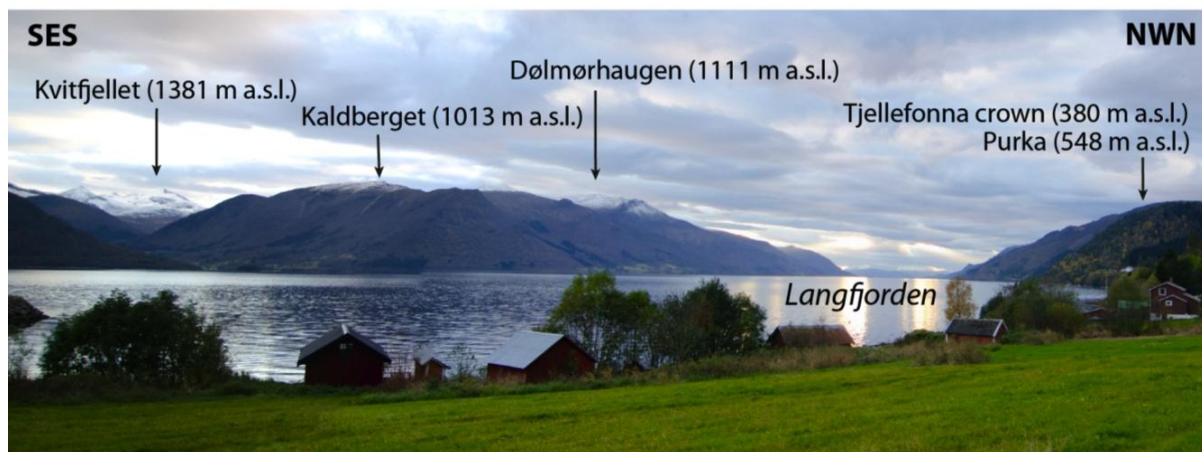
Figure 8: Langfjorden makes up a sharp lineament that separates the northern coastal plains, with the Purka mountain and the Tjellefonna, and the southern side which has an alpine relief (Sandøy, 2011b).

The slope gradient of the Langfjorden area is visualized in Figure 9 by a Digital Elevation Model (DEM). As can be seen, the slope gradients around Langfjorden vary from < 10° to > 40°. It should be noted that while the slopes on the southern side of the fjord have typical U-profiles, with steadily increasing gradients from the fjord, the northern side have high gradients (+30°) already close to the fjord. The study object, Tjellefonna (Figure 10), have slope gradients between 20° to 30° on the northeast side of the slide area, and 30° to 40° southwest of the slide (Figure 9 and Figure 10). The mean slope gradient from main scarp to the fjord (before the rockslide at 1756) is estimated to have been about 30°.
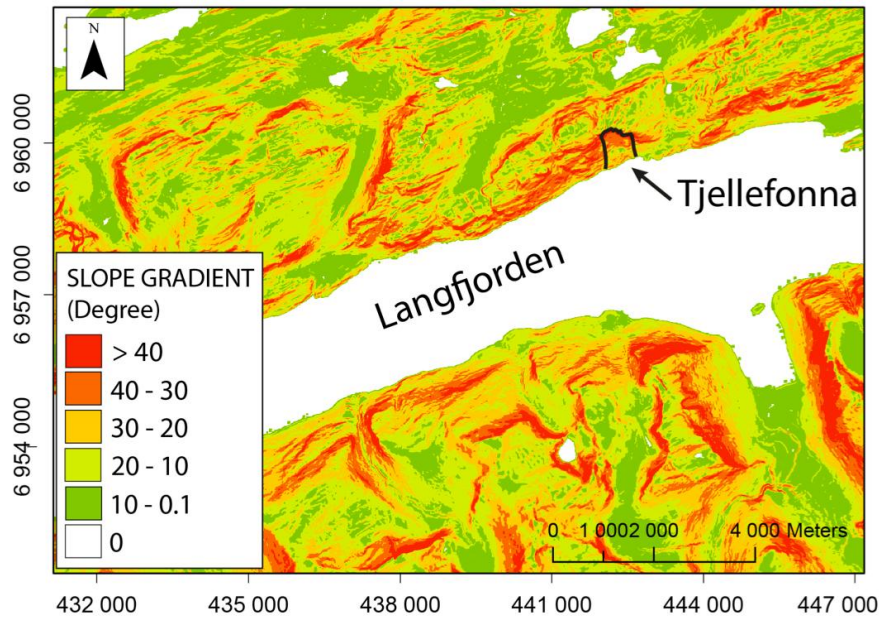
Figure 9: Slope gradient image based on a DEM. Note the difference between the slop gradients of southern and northern Langfjorden (Sandøy, 2011b).
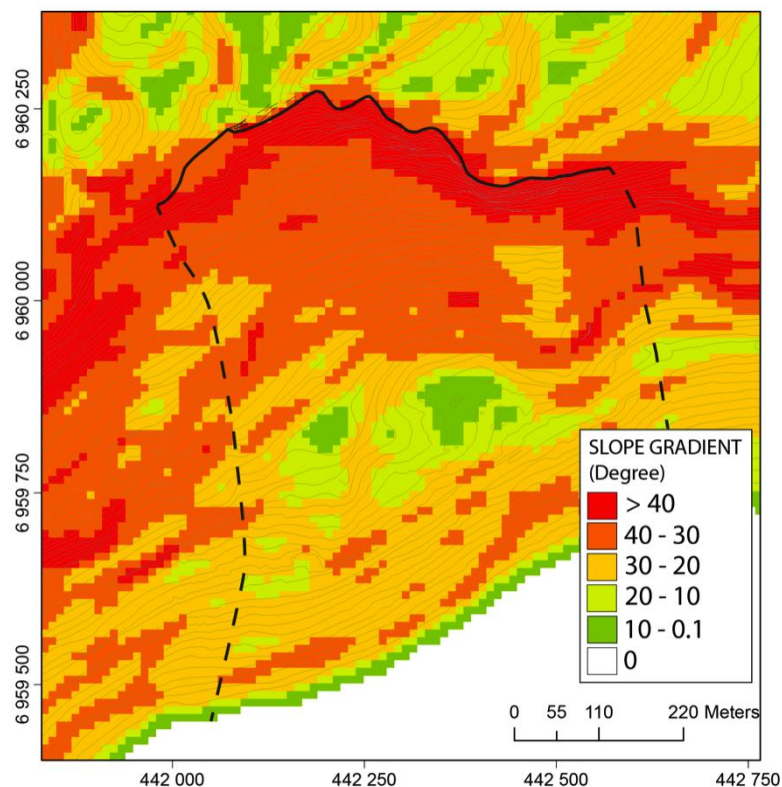
Figure 10: Slope gradient of Tjellefonna with contour lines of 5 meters, and the main scarp and lateral border in black. The mean slope gradient from main scarp to the fjord is estimated to have been about 30°(Sandøy, 2011b).

3.2. Hydrogeological conditions

There is no detailed sources or maps with mapped local hydrogeological conditions. To get an impression of the local hydrology, a map from Statens Kartverk (2011) is studied and modified as Figure 11. On the top of the landslide crown there are some areas with marsh. There is no river running through the landslide and down towards Langfjorden. However, there is small stream connecting the march lying further away from the crown area towards the northern lake "Gammelsetervatnet" (Figure 11).
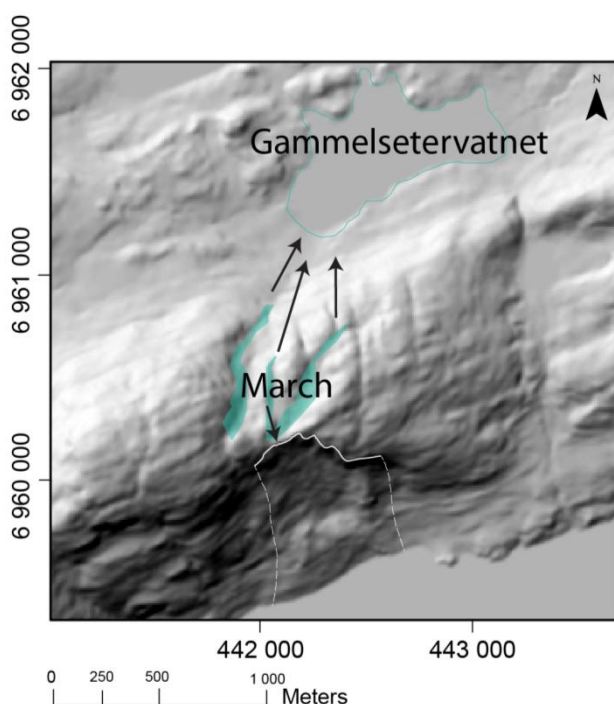
Figure 11: An overview of some near lying marches, modified from Statens Kartverk (2011). The march seems to be connected to the lake "Gammelsetervatnet". Furthermore, historical sources also observed that the near laying march at Tjellefonna added running water to the tension cracks (see chapter 1.4).

3.2.1. Annual precipitation from 1957 – 2009

The recorded daily precipitation data from 1957 to 2009 is collected from SeNorge.no (2011), and comes from the nearest weather station located in Eresfjorden (in the fjord arm to Langfjorden). Figure 12 gives an overview of the annual precipitation (total mm) from 1957 to 2009. The linear trendline reveals that the precipitation has increased about 300 mm in average from 1957 (1300 mm) to 2009 (1600 mm).

To fully understand the rain conditions, a more detailed analysis is conducted in Table 3. The results show that the area only has very few episodes of heavy rain, e.g. since 1957 it has only rained more than 100 mm on one day (0.02 days pr. year). There is further only 3.2 days pr. year with more than 37.5 mm of rain, and only 1.1 day with more than 75 mm. It appears that the amount of precipitation at the Tjelle area is not abnormally high, however, days of extremely heavy rain (e.g. > 100 mm) may happen.
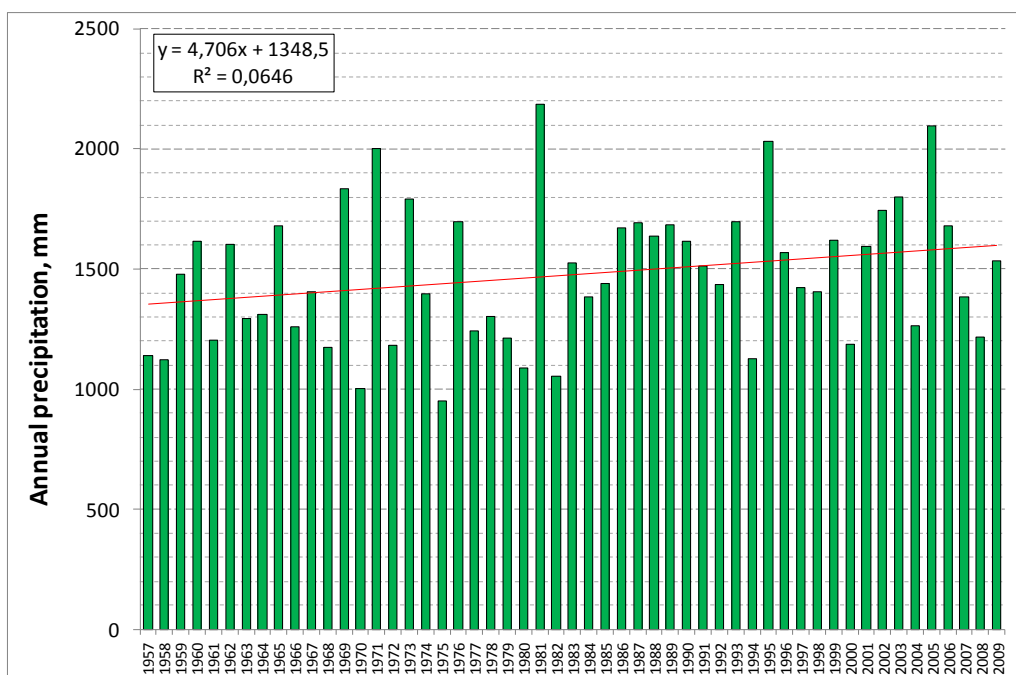
Figure 12: Annual precipitation (mm) per day from 1957 to 2009. Data modified from SeNorge.no (2011), weather station Eresfjorden. Notice that the annual precipitation has increased about 200 mm from 1957 to 2009 (Sandøy, 2011b).

Table 3: Precipitation analysis from 1957 to 2009 (Sandøy, 2011b).

Precipitation:	Number of days:	# pr. year:	% of total period:
> 100 mm	1	0,02	0,01 %
> 75 mm	9	0,2	0,05 %
> 50 mm	58	1,1	0,3 %
> 37,5 mm	168	3,2	0,9 %
> 25 mm	560	10,6	2,9 %
> 10 mm	2686	50,7	13,9 %
> 5 mm	4650	87,7	24,0 %
> 1 mm	7861	148,3	40,6 %
> 0 mm	10374	195,7	53,6 %
No rain	9013	170,1	46,6 %

16

4. Theory

4.1. Common causes of slope instabilities

Previous studies show that the driving forces and deformation mechanisms involved in rock slope failures can be divided into short-term factors (e.g. seismic activity, water pressure) and long-term factors. An important long-term factor is the gradual change in mechanical properties (shear resistance) of a sliding plane in the rock mass (Braathen et al., 2004). Figure 13 gives a summary of causes that are related to large rock slope failure.

Geological
- Role of discontinuities and foliation
- Shear strength of discontinuities and intact rock
- Faults and shear zones
- Weathered material
- In situ stress conditions

Morphological
- Slope topography
- Tectonic or volcanic uplift
- Glacial rebound

Physical
- Seismic activity
- In situ stress conditions
- Precipitation
- (Ground)water pressure
- Freeze-and-thaw weathering

Figure 13: An overview of common factors that influence the stability and rate of movement in large rock avalanches, modified from Grøneng (2010).

When it comes to the geologic features, some causes are more significant than others (Kanji, 2004). The stability of a rock slope will vary with the inclination of discontinuity surfaces within the rock mass, such as faults, joints and foliation. Highly unfavourable conditions arise when discontinuities dip towards the slope face with angles between 30° and 70° (e.g. simple sliding can occur). The presence, or absence, of discontinuities plays an essential role upon stability of a rock slope (Hoek and Bray, 1981).

The potential sliding planes are defined by the discontinuity sets, and the shear strength of the discontinuities represents the resistance against slope failure (Grøneng, 2010). The shear stress will reduce as the normal stress increases (Kanji, 2004). Also internal causes, such as weathering and pore fluids will lead to a decrease of the shearing resistance (Popescu, 2002).

A fault plane in a rock mass normally has a much lower friction coefficient compared to the rest of the rock mass. Faulting of a rock mass leads to the formation of continuous discontinuity planes, often combined with fragmentation of the rock mass. As a consequence, water may percolate in to the fractured rock mass and further reduce its shear strength (Kanji, 2004).

When it comes to the morphological factors the effect of glacial rebound on stability of mountain slopes is thought to be the most important factor at high latitudes. The glacial processes influence the rock stability by over-steepening the slopes. Several authors argue that the load of the glacier produces high internal stresses on the valley floor and slopes. During the phase of glacial rebound there is a release of elastic strain energy that may result in propagation of joint network and later cause failure (Braathen et al., 2004). In Norway there are only a few described cases where rockslides were deposited directly on top of glaciers. This indicates that the effect of glacial rebound on slope stability can be considerably delayed due to time-depended dissipation of residual stresses within the rock mass (Ballantyne, 2002; Wyrwoll, 1977).

Numerous rockslides have been triggered by seismic activity in historical times in the world. In Norway there are no certain examples of earthquake-triggered slope failure, but the mechanism has been suggested for the offshore Storegga slide (Blikra et al., 2006a). Figure 14 givens an overview of micro- and macro-seismic events recorded between 1980 and 2000 (yellow circle) and historical events (blue circle) in Norway (Redfield and Osmundsen, 2009). The figure shows a high concentration of activity in Møre & Romsdal with a mean magnitude of 2.26. Table 4 shows the recorded earthquakes in Møre & Romsdal between 1981 and 2010, which gives a mean magnitude of 2.67. According to Jibson (1994) and Keefer (1984) a minimum magnitude of 6.0 is required to trigger a rock avalanche, however, an earthquake magnitude larger than 5.5 is not common in Norway (Braathen et al., 2004).

A study by Keefer (1984) shows that deep-seated landslides are triggered by stronger and longer-lasting shaking, in difference to shallower rock slides and rock falls, which are susceptible to short, high-frequency shaking. The importance of earthquakes as rockslide triggers is observed from the concentration of pre-historical rock avalanches and rock-slope failures in areas of large earthquake activity (Blikra et al., 2002). Earthquake trembling is therefore suggested to be a semi-regional trigger, which is also supported by the occurrence of a series of subsequent rock slides events, rather than just one major event (Blikra et al., 2006a).

Table 4: Overview of recorded earthquakes in Møre & Romsdal (1981 - 2010) from NORSAR (2010). The mean magnitude is 2.7 (Richter scale).

Date:	Magnitude:	Location:	Date:	Magnitude:	Location:
01.03.81	2,60	Ålesund	29.05.99	3,9	Måløy
18.03.81	1,7	Volda	07.08.99	2,2	Stryn
15.10.82	2,9	Volda	14.10.99	1,8	Volda
15.12.82	3,9	Selje	13.03.00	2,2	Ørsta
15.08.83	2	Nordfjordeid	05.07.00	2,2	Volda
05.02.86	4,6	Selje	06.07.00	3,1	Ålesund
29.03.90	2,9	Volda	15.02.04	1,6	Selje
11.03.92	2,6	Ålesund	04.02.05	1,9	Volda
28.06.92	2,2	Ålesund	21.01.07	3,5	Ålesund
07.07.92	2,8	Ålesund	22.02.07	2	Molde
27.07.94	4,1	Selje	23.04.07	1,7	Selje
14.03.95	2	Selje	19.05.09	3	Selje
16.04.96	3,1	Selje	14.06.09	2,9	Ålesund
28.04.97	2,8	Selje	01.03.10	2,1	Måløy

Another essential component regarding slope stability is the presence of water. During periods of snow melting and heavy rainfall, water pressure increases, especially in well developed fracture sets. Grøneng (2010) listed different ways that groundwater may affect slope stability:

- By reducing the normal stress; groundwater pressure will reduce the normal stress acting on the sliding plane(s) and by this reduce the friction along the sliding plane(s).

- By acting as driving force; the groundwater may act directly as a driving force in tension joints.

- By reducing the internal friction; the groundwater may reduce the internal friction i.e. the strength of joint filling material and possibly also cause swelling of gouge material.

- Due to expansion by freezing; water expands by approximately 10% when freezing, which may cause considerably displacements and forces reducing the stability.

- By causing erosion; in weak rock, flowing water may cause washout and erosion reducing the stability.

In general the presence of faults and well developed discontinuity sets increase the effect of water on the rock mass stability (Bauck, 2010). The combination of increased water pressure, freezing-thawing processes and the gradual reduction in shear resistance of discontinuities is recognized as an especially critical aspects for the stability of rockslide areas. In such settings, seismic activity may be the final trigger, leading to failure for all types of rock slope failures (Braathen et al., 2004).
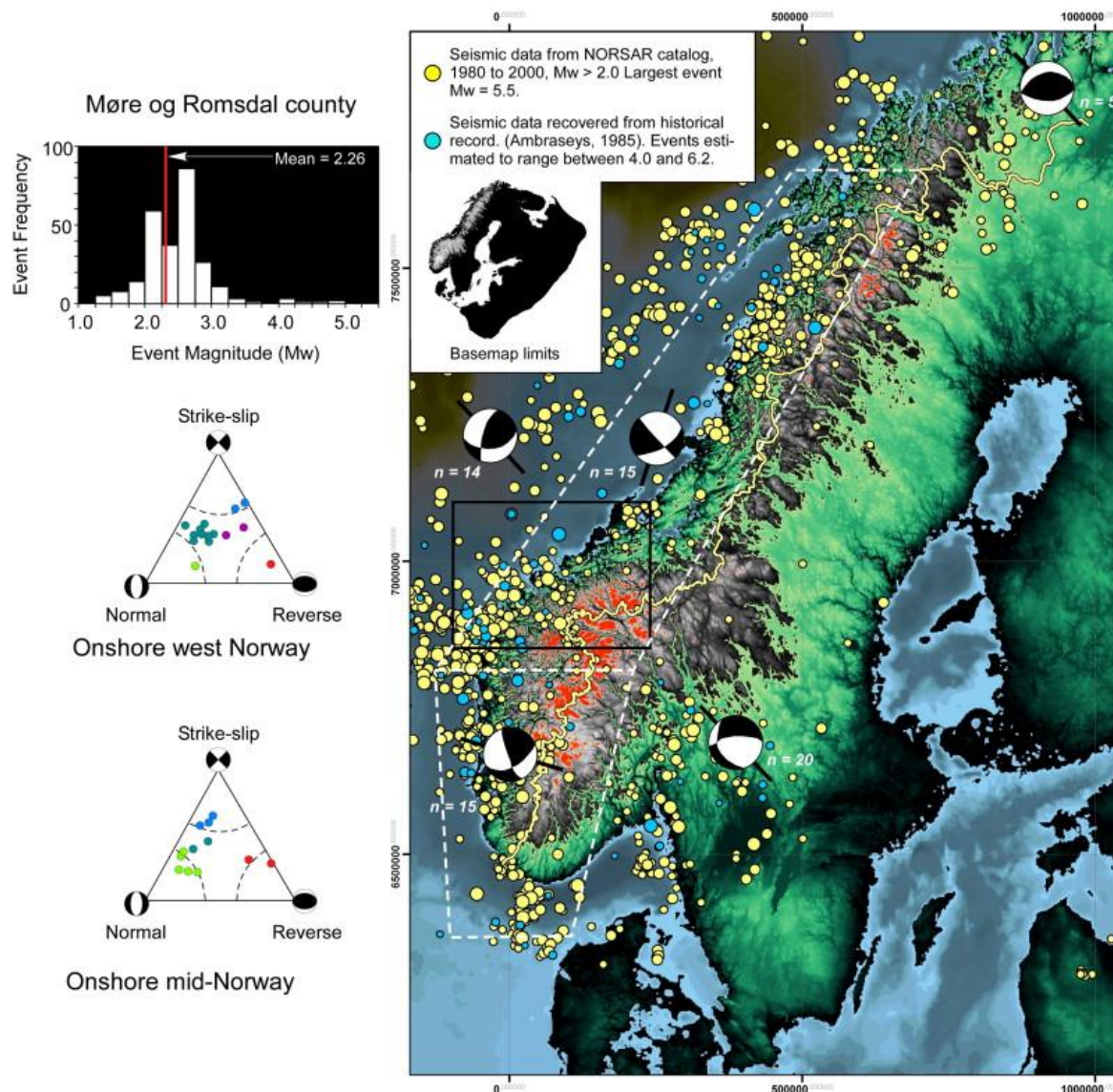
Figure 14: The main figure above shows the seismic epicentreplot for Scandinavia. The data is collected from NORSAR earthquake catalogue (http://jordskjelv.no/NORSAR.html). The yellow circles illustrate micro- and macroseismic events recorded between 1980 and 2000, and blue circles represent event relocated from historical records. The black rectangle locates Tjellefonna, MTFC and Langfjorden. Note the seismic cluster in regions known for rock avalanche are Møre & Romsdal, Troms, and Sogn & Fjordene. The histogram at upper left corner is defined by NORSAR, and displays the near-normal distribution, with Mw = 2.26, n (frequency) = 278. The two lower left triangles shows the available focal plane solutions from Hicks et al., (2000). Both the onshore figure for west and mid-Norway have a majority plotted in the normal/strike-slip side of the ternary diagrams. Figure as a whole is from Redfield and Osmundsen (2009).

4.1.1. Progressive reduction of safety factor

When it comes to causes that lead to failure of a slope, it is important to include both conditions and processes. Geological factors are influential as conditioning features, but are not the triggering causes. They are part of the conditions necessary to develop failure, but additional environmental criteria, like stress release pore water pressure and temperature, are needed for failure to take place. Failure will only occur if there is an effective underlying process (e.g. heavy rainfall, seismic activity) acting enough to change the static ground conditions sufficiently to cause failure (Popescu, 2002).

Figure 15 illustrates that seasonal factors, like rainfall, is reflected in variation in safety factor of a slope. If there is a long-term trend in groundwater level, or changes in strength (e.g. weathering), these will also show up as a trend in the graph. Sudden factors, like variability of rock mass strength or acting forces, give short-term variations in the graph (Popescu, 2002) and decrease of the safety factor. This figure clearly illustrates that a landslide can rarely, or never, be attributed to a single factor (Varnes, 1978).
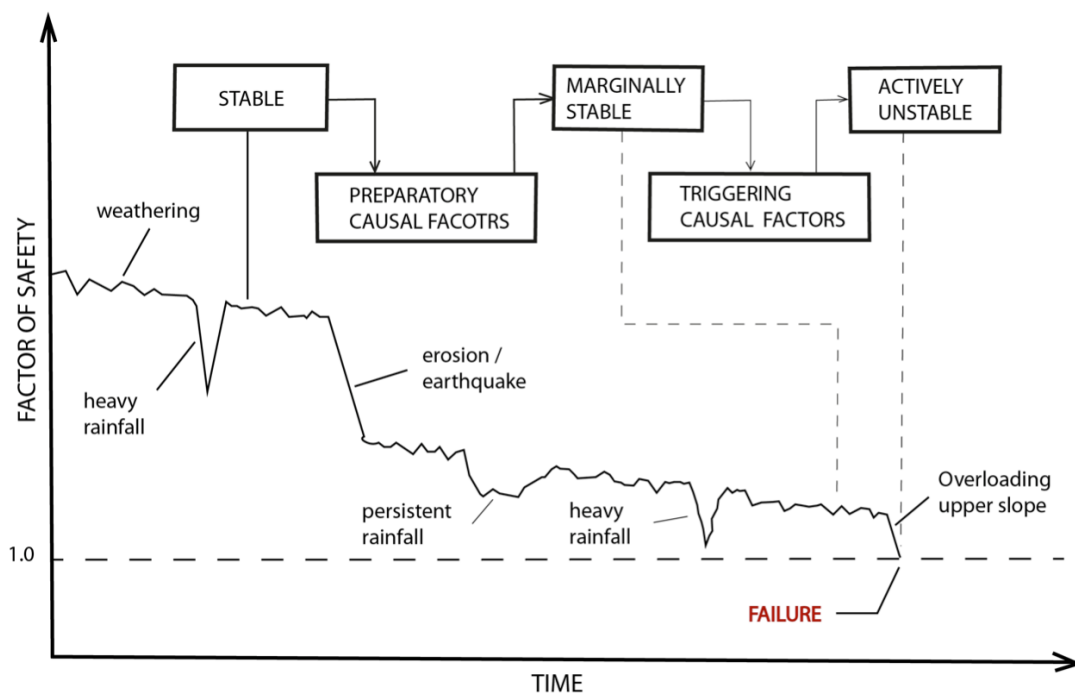
Figure 15: The figure is modified from Popescu (2002), and shows an example of safety of factor as a function of time to better understand the different landslide causes. The figure illustrates that a landslide can rarely be attributed to a single factor.

4.2. Mobility of rock slide deposits

Experience shows that rock avalanches are excessively mobile, and that the degree of mobility appears to increase to the logarithm of the volume of the event. The main hypotheses of this phenomena are listed below, and comes from Hungr and Evans (2004).

- Mobilization by an air cushion, overridden and trapped beneath the mass of the rock avalanches.
- Fluidization by similar trapped air or by stream generated by vaporization of groundwater.
- Fluidization by dust dispersions.
- Rock melting or dissociation by the heat of friction.
- "Mechanical fluidization": understood as a process of spontaneous reduction of friction angle at high rates of shearing.
- Acoustic fluidization: reduction of the friction angle from acoustic-frequency vibrations at the base of the flowing mass.
- Increase in areal dispersion of debris as a result of fragmentation.
- Lubrication by liquefied saturated soil entrained from the slide path.

It is found that there is an initial volume increase when a rock mass disintegrates and fragments from a coherent mass and transforms into a rock avalanche. There are only a few studies of this behaviour in literature, where the results estimate an increase of volume between 7 and 26% (Hungr, 1981). Field estimations of source and deposit volumes are difficult, and from Hungr and Evans (2004) it is assumed that fragmentation produces a volume increase of $\sim$ 25%. The assumption is based on the mean of the typical range (18 – 35 %) of measured porosities of well-graded loosely crushed rock from (Hungr and Evans, 2004; 1963).

Hungr and Evans (2004) introduced the following equation to describe the total volume of the landslide deposit:

$$V_{Tot\_Deposits} \; = \; V_R(1 + F_F) + \; V_E \qquad\qquad \textit{Equation 1}$$

Where V_R = Volume of initial rockslide

            F_F = Fraction amount of volume expansion due to fragmentation (0.25).

            V_E = Volume of debris entrained from the path

4.3. Stability analysis

There are several methods that can be used for analysis and calculation of slope stability (Nilsen and Broch, 2009):

1) Kinematic (empirical analysis)
2) Limit equilibrium
3) Numerical analysis (continuum, discontinuum, hydride finite -/discrete element with fracture)

Figure 16 shows that the preferred analysis method (e.g. kinematic or continuum) depends on the degree of failure complexity (Stead et al., 2006). The kinematic analysis has been carried out in the project assignment during fall 2011, and showed that the Tjellefonna failure is to complex to be addressed with only simple kinematic analysis.
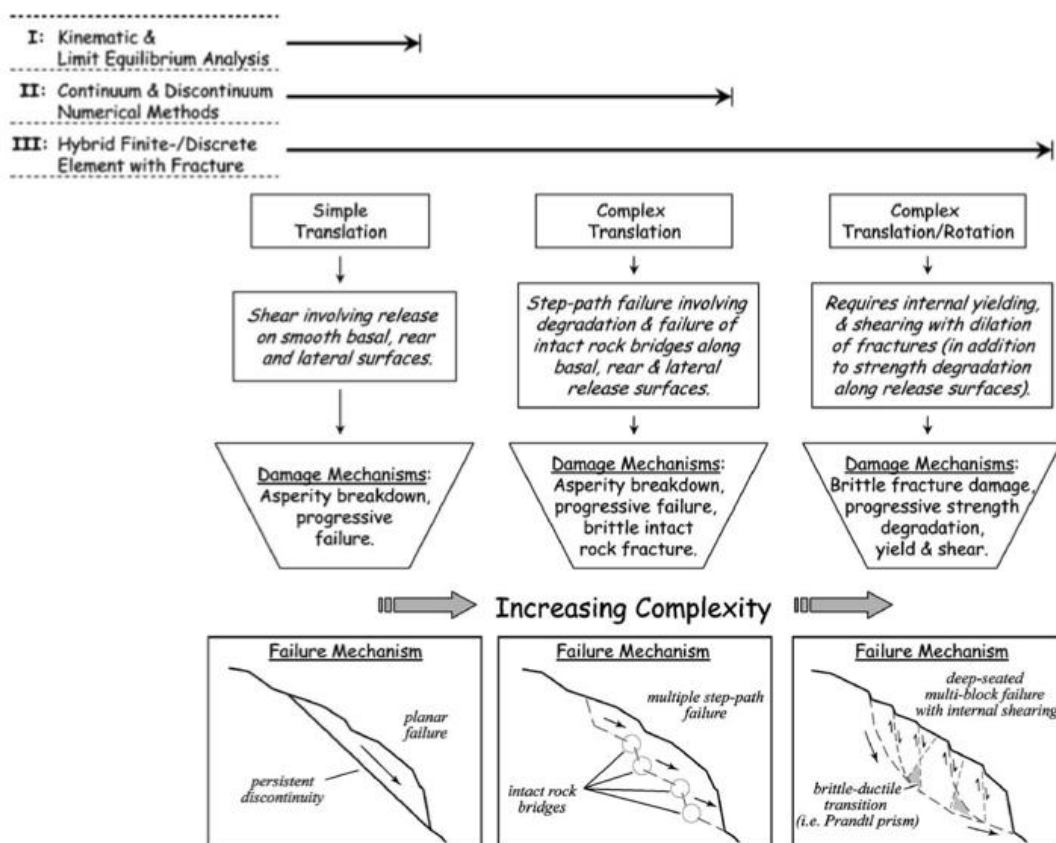
Figure 16: An illustration of three levels of landslide analysis with increasing complexity of failure mechanism (Stead et al., 2006).

4.3.1. Limited equilibrium method (LEM)

Traditional deterministic analysis has been widely used in rock slope analysis, based on calculation of stabilizing and driving forces (Nilsen et al., 2011). The stability of a slope can be quantified by the ratio of the resisting and driving forces, called the factor of safety (FS) (Wyllie and Mah, 2004).

The factor of safety can be expressed as:

$$FS \ = \ \frac{resisting\ forces\ (R_d)}{driving\ forces\ (F_d)}$$

<div align="right">Equation 2</div>

Failure will theoretically occur when the driving forces (like gravity and water pressure) are larger than the resisting forces (i.e. when FS < 1.0). The traditional analysis involves the assumption or delineation of a two-dimensional slide surface (Figure 17), and a back-analysis performed to determine the force/moment equilibrium conditions existing on the surface at failure (Eberhard, 2003).
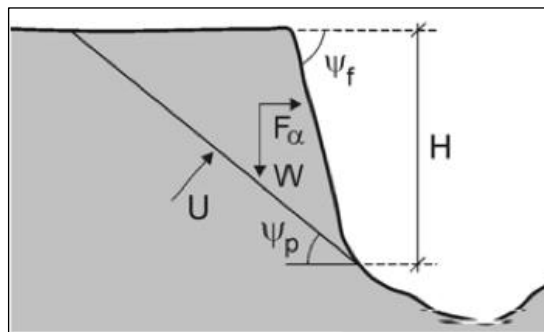
Figure 17: Illustration of limit equilibrium on a slope geometry, where additional trigger forces as water (U) and earthquake (Fα) (Nilsen and Broch, 2009).

Where:	R_d	[N]	$(W\cos\psi_p - U - F\alpha\sin\psi_p)tg\varphi_{ca}$
	F_d	[N]	$(W\sin\psi_p + F\alpha\cos\psi_p)$
	φ_{ca}	[°]	Characteristic active friction angle
	U	[N]	Force resultant of water pressure
	$F\alpha = m \cdot \alpha$	[N]	Force caused by earthquake ground acceleration α
	W	[N]	Weight of potential sliding rock mass
	H	[m]	Height of slope
	ψ_p	[°]	Dip of the sliding plane
	ψ_f	[°]	Dip angle of slope

4.3.2.   Numerical modelling

Numerical modelling is today routinely used in civil and mining engineering in stability analysis (Moraes, 2011). Numerical modelling approximate solutions to problems and indicate failure mechanisms (stresses, triggers factors and discontinuities), which would otherwise not be solvable using conventional techniques like limit equilibrium. Figure 18 gives a general classification of analytical methods (Eberhard, 2006).

Continuous: Differential models	Discontinuous: Block models	Hybrid modelling
•Best suited for the analysis of slopes that are comprised of massive, intact rock, weak rock and soil-like or heavily jointed rock masses. •Procedure exploits approximations to the connectivity of elements, and continuity of displacements and stresses between elements.	•Appropriate for slopes controlled by discontinuity behaviour. •Rock mass represented as an assemblage of distinct interacting blocks. •Blocks are subdivided into a deformable continuum mesh following linear or non-linear stress-strain laws.	•Involves the coupling of continuum and discontinuum to maximize their key advantages

Figure 18: Three main models used in numerical analysis, where continuous models represent FDM and FEM methods. Figure modified from Eberhard (2006).

The continuous approaches treat the rock mass as a continuum material that is divided into a finite number of elements. The method includes finite-difference (FDM) and finite-element methods (FEM). Both methods produce a set of algebraic equations to solve. However, in FEM the set of equations is solved implicitly (static solution is found by using matrix form), while in FDM the set of equations are solved with a time-marching scheme.

Continuous models have a disadvantage compared to discontinuous models, since they are not able to handle general interaction, as intersecting joints (Willie and Mah, 2004). The discontinuous modelling is more appropriate when the rock slope is composed of multiple joint sets, which control the mechanism of the failure (Eberhard, 2003), as the rock mass is divided into discontinuous blocks. The joints are presented explicitly and movement of the rock mass occurs as sliding, rotating and separation of blocks

(Willie and Mah, 2004). Additionally, this methodology is collectively referred to as the discrete-element method (DEM), and exists in several variations (e.g. discontinuous deformation analysis (DDA) and particle flow codes) (Eberhard, 2003).

4.4. Digital Elevation Model (DEM) analyses

Digital Elevation Model (DEM) is a powerful tool to illustrate the Earth´s surface in three dimensions for both interpretation and visualization. DEM represents the topography in 3D as a raster (grid of square cells with a constant cell size), or as a triangular irregular network (TIN) based on vectors (Oppikofer, 2009). Each specific cell in the DEM will have a value which represents the elevation of the area (Elgin, 2005).

Morphological structures related to landslides (e.g. faults, open cracks, bulges) can be investigated by using DEM. It is very important though that the resolution of the DEM should be selected on the basis of the purpose of the analysis (Sandøy, 2011c). The main uses of DEM regarding rockslides are listed below:

- Slope angle and slope aspect
- Shaded relief maps (or hillshade); visualize the terrain
- Hydrological tools; perform hydrogeological analysis on the regional scale. Can be used to e.g. identify sinks and find flow networks.
- Coltopd3d: software that allows structural analysis to be performed on DEM. The principle is that this software gives each grid cell a colour representing the main orientation (dip direction and dip) of discontinuities.
- Kinematic stability assessment by using Matterocking. This software is developed to compare geological structural data with the topographic DEM surface to determine potential failures (i.e. planar, wedge or toppling).
- Finding potential unstable volume with Slope Local Base Level (SLBL)
- Regional rockfall analysis by using critical slope angle, SLBL method (to identify erodible areas) and the present of discontinuities that can develop failure (planar, wedge or toppling failure).

DEMs are today frequently produced from remote sensing data, for instance Interferometry Synthetic Aperture Radar (InSAR), Shuttle Radar Topography Mission (SRTM), and Light Detection Ranging (LiDAR), including Aerial Laser Scanning (ALS) and Terrestrial Laser Scanning (TLS) (Oppikofer, 2009).

The choice of grid cell size is one of the major sources of uncertainty, since the accuracy of analysis is depending on type and spatial resolution of the raw data. The grid cell size normally varies from around 30 meter down to 0.1 meter depending on the source (Oppikofer, 2009). The raw data may also include buildings and vegetation, in which it is defined as a Digital Surface Model (DSM). A filtering of these features from the raw data gives a DEM that represents the "bare" earth surface (Elgin, 2005; Köthe, 2000).

4.4.1. Ante-rockslide topography (ART) and volume calculations

Volume calculation of ancient rockslide may be feasible through (Oppikofer, 2009):

- Aerial photographs   (Mora et al., 2003)
- Topographic maps   (Evans et al., 2001)
- Surface reconstruction based on contour lines (outside and   (Brückl, 2001)
  within the scar area)
- Interpolation methods (inverse distance weighting or kriging)   (Gorum et al., 2008)

Historical rockslides, like Tjellefonna (1756), are too ancient to obtain information as pre-aerial photographs and topographic maps. Furthermore, previous work from Oppikofer (2009) shows that both contour lines and interpolation methods provide not sufficient constrains for volume calculations. Two different approaches are used in this master thesis, both based on DEM, to create the ante-rockslide topography (ART) based on methods and guiding from Oppikofer (2009, 2012):

1) Manual construction in 3D by software PolyWorks
2) Sloping Local Base Level (SLBL) technique implemented in the software CONEFALL (Jaboyedoff, 2003)

4.4.2. Slope Local Base Level (SLBL)

Unstable volumes of rockslides can be estimated with the slope local base level (SLBL) technique, which locates the lowest sliding basal surface for a given topography (Jaboyedoff et al., 2005; Jaboyedoff et al., 2004). SLBL is a simplification of the geomorphological definition of a "base level" (Jaboyedoff et al., 2004), where base level is defined as the lowest level that can be eroded by a stream (Jaboyedoff et al., 2004; Strahler and Strahler, 2002). The classical base level is not useful for landslide characterization, as the creation of a peneplain includes all erosion processes and has a time scale far beyond the scope of landslide hazard assessment. The SLBL is a short-term (~ 50 000 years) concept used in landslide analyses to define basal surfaces where rock masses are prone to be eroded (Jaboyedoff et al., 2004).
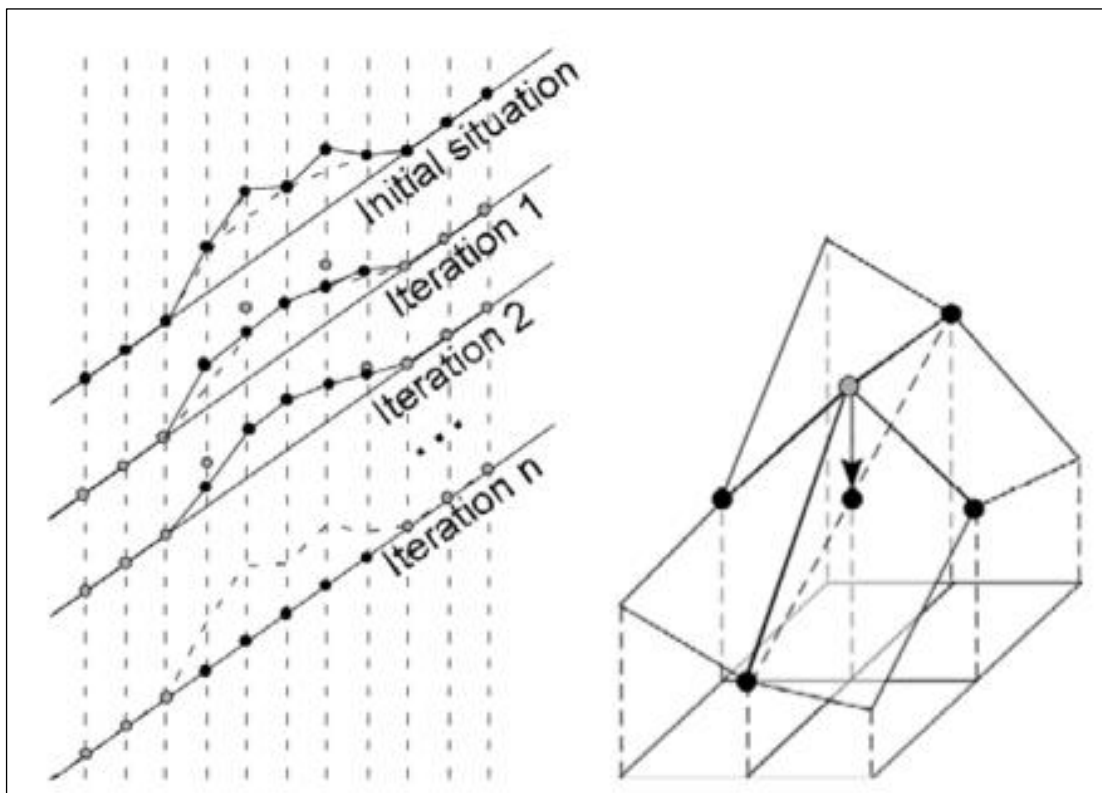
Figure 19: A schematic illustration (left) of the steps in the computation of the SLBL for a 2D slope containing a spur, where the spur is lowered to a straight line after n iteration. The illustration on the right shows the SLBL computation in 3D where the arrow indicates that the central point is lowered to the mean value of the minimum and maximum values of its four neighbours (Jaboyedoff et al., 2004).

The ART is computed by an iterative procedure, which flattens and lowers the spurs and spikes between defined fix points (Figure 19). All points located above the mean (maximum and minimum) of their two neighbours are replaced by the mean value of the two (±tolerance), which results in a straight

line (Figure 19). However, introducing a tolerance value, *curvature (c),* leads to a second degree curve (Jaboyedoff et al., 2004) as a convex (negative curvature) or concave surface (positive curvature). Curvature is calculated from the formula below (Jaboyedoff and Derron, 2005):

$$\Delta c = \pm \left(\frac{4h_{max}\Delta x^2}{L^2} \right)$$

<div align="right">Equation 3</div>

Where: $hmax$ =   Difference between curvature value zero (c=0) and interpreted thickness of deposits or reconstructed topography.

Δx =   Grid cell size

L =   Profile length

One important issue regarding this method is that some points need to be fixed for the computation of the SLBL; otherwise the result is a flat elevation (corresponding to the old concept of base level). Such fixed points are manual defined by using features such as rivers (drainage network), geomorphic features (Jaboyedoff et al., 2005; Jaboyedoff et al., 2004), or the limits of a rockslide (Derron et al., 2005).

5. Methodology

The back-analysis presented in this thesis includes a reconstruction of the topography (i.e. ART), volume estimations and a stability study based on numerical modelling. Table 5 gives an overview of the different methods and the software's used.

Table 5: Overview of different methods and software's used in this thesis.

Software and methods:	Tasks:
• SLBL method implemented in the CONEFALL software • The PolyWorks software	Reconstruction and volume estimations
• Numerical modelling by the Phase^2 software using shear strength reduction (SSR)	Stability analysis, parameter study and evaluation of triggering factors

5.1. Input for numerical modelling

5.1.1. Laboratory work

A week of laboratory experiments was conducted between the 10th and the 15th of October 2011 as a part of the depth-study topic "TGB4505 Engineering Geological Laboratory Methods". The laboratory work strictly followed the ISRM standards and NTNU/SINTEF standards.

Two different rock samples from Tjellefonna were used in all the experiments. The rock samples were collected from the rockslide deposits, and represent the main granitic to granodioritic rock type of Tjellefonna. The results of these experiments can be found in Sandøy (2011b), and Table 6 lists the standards used in this master thesis.

Table 6: Laboratory test and standards.

Tests:	Source:
Tilt test	(NTNU, 2009)
UCS	(ISRM, 2007a)
Young's modulus	(ISRM, 2007b)

5.1.2.   Field work – r/R, JCS and JRC

A one-day field investigation was accomplished (25.feb 2012) to collected parameters to estimate the shear strength of discontinuities based on the empirical Barton-Bandis relationship.

The residual angle for rock joints with rock-to-rock contact may be estimated based on the equation (Barton and Choubey, 1977):

$$\varphi_r = \varphi_b - 20 + \left(20 \times \frac{r}{R}\right)$$

Equation 4

Where φ_b is the basic friction angle and r/R is the Schmidt-hammer rebound ratio.

Furthermore the discontinuities shear strength can be estimated by the equation (Barton and Choubey, 1977):

$$\tau = \sigma_n \tan\left(\varphi_r + JRC log_{10}\frac{JCS}{\sigma_n}\right)$$

Equation 5

In this equation JCS represent the joint compressive strength and JRC the joint roughness coefficient. The logarithmic function $\left(JRC log_{10} \frac{JRC}{\sigma_n}\right)$ represent the amount of surface irregularities effecting the shear strength and corresponds to the dilation value (i). The ratio $\frac{JRC}{\sigma_n}$ tends to approach infinity at low stress levels, and in order to predict realistic shear strength the useful range of the ratio is 3 to 100 (NTNU, 2009; Willie and Mah, 2004). However, the shear strength is dramatically reduced when part, or all, of the surface is filled with gouge and is controlled by the shear strength of gouge material (Barton et al., 1974). The equations above are only used with unfilled rock joints.

The Schmidt hammer determines the rebound hardness of a test material, where a spring-loaded mass is released against a plunger when pressed onto a hard surface. The height of rebound of the mass is measured on a scale and gives an estimation of the rock mass hardness. The field work was conducted with a L-hammer having an impact energy of 0.74 Nm (ISRM, 1978). At Tjellfonna, the Schmidt hammer was used on both rebounds values (r,R) and estimation of JCS.

Barton and Choubey (1977) recommends that the each rebound value consists of total of 10 readings (in different locations), in which the mean of the five highest readings represent the value used. Furthermore, JRC is given by a total of 20 measurements (separated by at least the diameter of the

plunge) as described in ISRM (1978), where the mean value of the ten highest is to be used. The lower readings may be influenced by factors that do not reflect real hardness of the rock (Kveldsvik et al., 2007).

All measurements of r, R and JCS were conducted perpendicular to the joint surfaces, and the results were afterwards transformed into horizontal-values by using the transformation curves from the manufacturer (NTNU, 2009). See Appendix 1 for more details about field performance.

Estimations of JRC are conducted through amplitude measurements of the joint surfaces in several directions (along the dip direction, along the strike and $\pm 45°$ to the dip direction) by using a straight ruler of 50 cm, as well as supplementing 10 cm long profiles. The final JRC value is estimated from the ratio of the amplitude and profile length. Refer to NTNU (2009) standards for details and standard graphs.

5.2. Landslide analysis using Digital Elevation Model

5.2.1. Digital elevation model (DEM)

This digital elevation model of Langfjorden is an indisputable investigation tool in order to analyse the 1756 rockslide, as quite heavy vegetation and steep mountainsides makes it hard to see the large-scale morphologies in field. The DEM has been used both for the reconstruction of the pre-landslide topography and for estimations of the landslide volume.

Figure 20 illustrates the 10-meter grid (pixel cell size) DEM of Tjellefonna and the associated hillshade. The hillshade creates a hypothetical illumination of the surface by setting a position for a light source and calculate the illumination values of each cell in relation to neighbouring cells (ESRI, 2011).
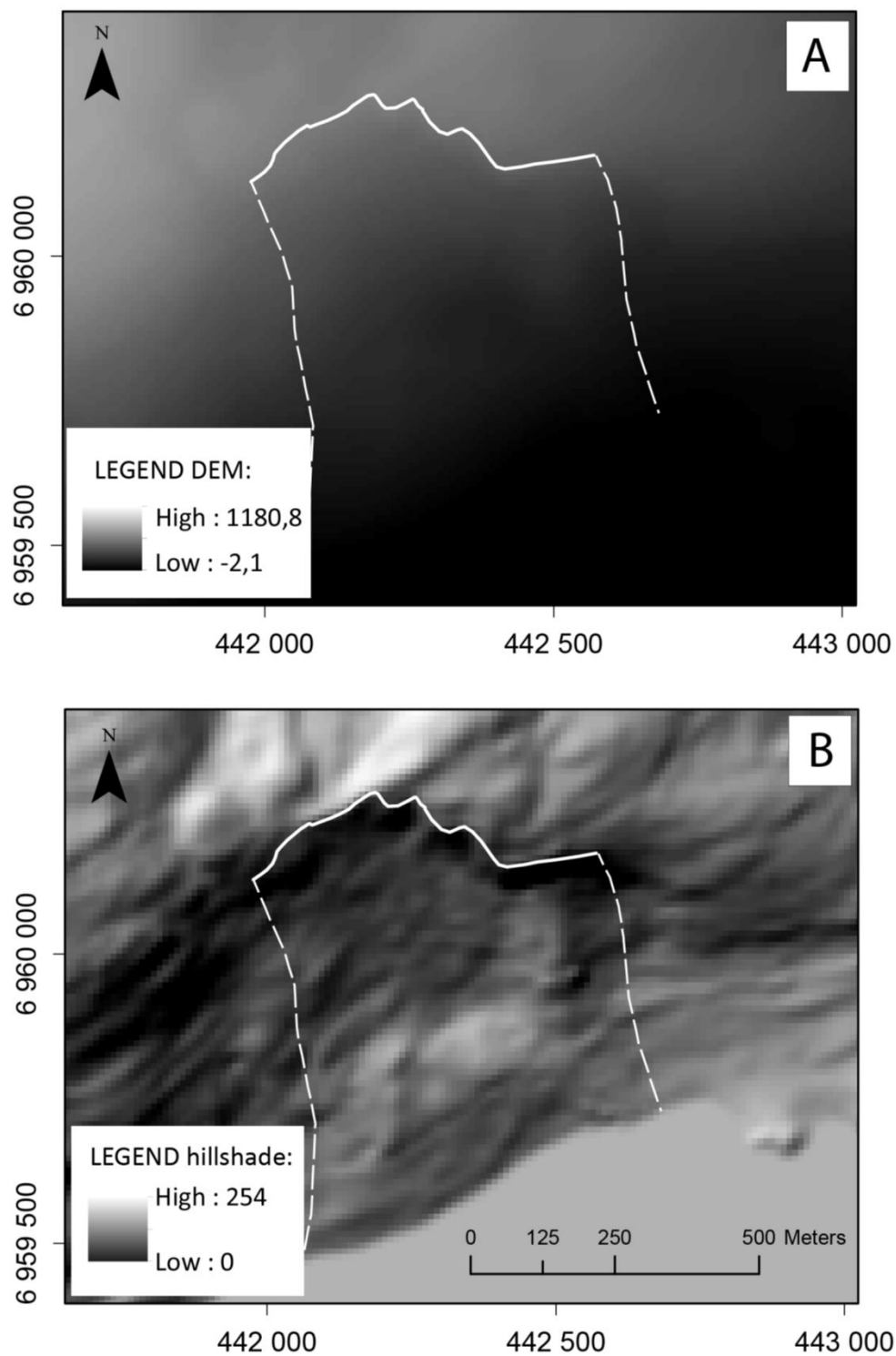
Figure 20: A) 10 meter grid DEM of Tjellfonna, where white dashed and continues lines represent the rockslide limits. Each grid cell contains information about the elevation at that point. B) The produced hillshade. This view takes into account the azimuth (angular direction of the sun) and altitude (slope or angle of illumination source) (ESRI, 2011).

5.2.2.   Ante-rockslide topography (ART) and volume calculations

A reconstruction of the ante-rockslide topography (ART), basal surface and estimate volumes have been conducted though using the SLBL and PolyWorks techniques. See chapter: 4.4.1 for more information.

The reconstructions of ART and volume estimations are based on an interpretation of the SW - NE trending slope morphology (Figure 23), which divides the mountainside into two parts: an upper steeper part rising against the back walls and a lower flatter part towards the fjord. The failed area of Tjellefonna is interpreted to belong to the steeper morphology.

PolyWorks

The software PolyWorks (version 11.0.4) from InnovMetric is used to recreate the 3D topography in the module IMInspect (InnovMetric, 2007). PolyWorks is a useful tool for analysing terrestrial laser scans (TLS), and to recreate the rockslide topography based on point clouds or DEMs (Oppikofer, 2009).

In this thesis the manual ART reconstruction in PolyWorks uses the DEM of Tjellefonna as the raw data. Figure 21 illustrates two different approaches toward reconstructing the ART. It is important in both cases that the polylines or planes generated lay below the rockslide surface in order to complete the reconstruction (Oppikofer, 2009, 2012).

Method 2 was chosen for the reconstruction of the pre-landslide surface, as the first method did not provide satisfying results (Figure 21). Fitting planes were to challenging due to large elevation differences across the slide. The ART of Tjellefonna is constructed by a combination of mapped field observations (fix points) and detailed study of the DEM. The final polylines from PolyWorks is added into ArcGIS and used to create a TIN surface representing the interpreted ART. Furthermore, the TIN was converted into a DEM with the purpose of calculating the volume (see chapter 5.2.3).

Reconstruction methods in PolyWorks

METHODE 1:

1) Fitting planes forming the ancient rockslide surface before the failure

2) Create vectors between intersections of two planes

3) Place points in the intersections between three planes

4) Create polylines based on points from step 3

5) Select polylines (step 4) to export into ArcGIS and create a TIN, which represents the ART

METHODE 2:

1) Place manual points over the area which is determine to be recreated. These points will be the base of the new topography.

2) Create polylines based on step 1

3) Select polylines (step 2) to export into ArcGIS and final create a TIN, which represents the ART

Figure 21: Overview of different manual reconstruction methods applied in software PolyWorks.

Slope Local Base Level (SLBL)

The Tjellefonna reconstructed ART and volume (reconstructed ART and deposits) are determined using the Slope Local Base Level (SLBL) technique implemented in the CONEFALL software. A flowchart overview of the SLBL procedure is given in Figure 22. Note that there is a clear separation between the ART reconstructed surfaces and the deposit (onshore and fjord) surfaces, where the ART reconstruction gives the reconstruction of the failed area (ART) and the corresponding volume, while the deposit (onshore and fjord) surfaces give the basal surface and the deposit volumes.

As an example of the ART reconstruction, Figure 23 illustrates the first step of this approach, which is the creation of polylines of the rockslide limits. Polygons are then created based on these polylines, representing the deposit areas (total deposits onshore and deposits restricted by the ART) and the reconstructed ART area. The landslide limits are defined as fixed points where value -1 and 1 is set depending upon the polygons (ART or Deposits), see Figure 24A-B. These raster data are then exported as ASCII (grid text format) files, which is the standard input and output files in the CONEFALL

software (Jaboyedoff, 2003). The next step is to create a new DEM (as an ASCII), which is manual defined to have area larger than the rockslide. However, for the reconstruction of the ART this DEM needs to be inverted (multiplied with -1), since the SLBL algorithm is only able to lower the surface. SLBL can thereafter be estimated based on the new DEM, polygons and fixed points limits (Oppikofer, 2009, 2012).
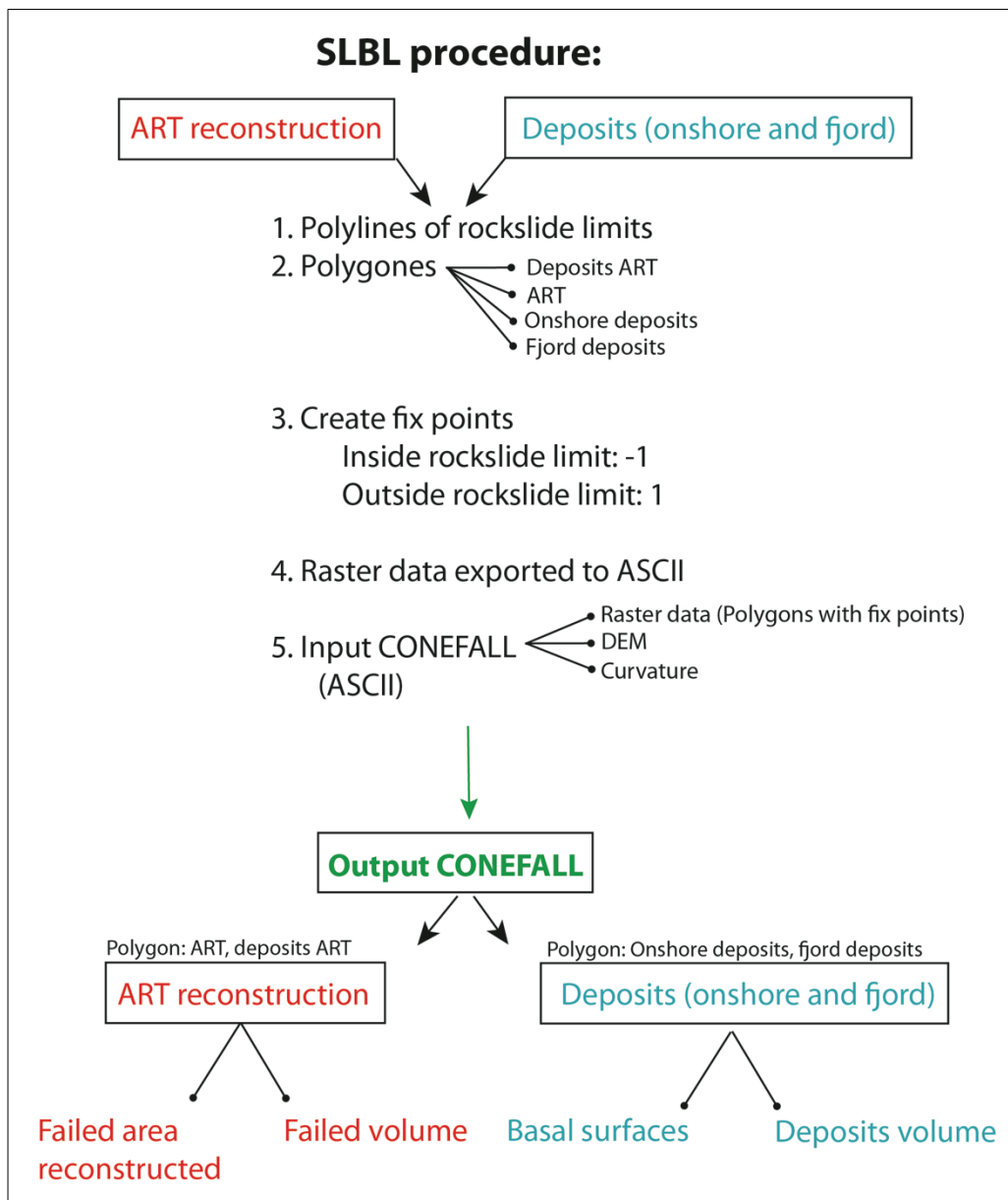
Figure 22: A flowchart of the SLBL procedure for ART reconstructed and deposits (onshore and fjord).
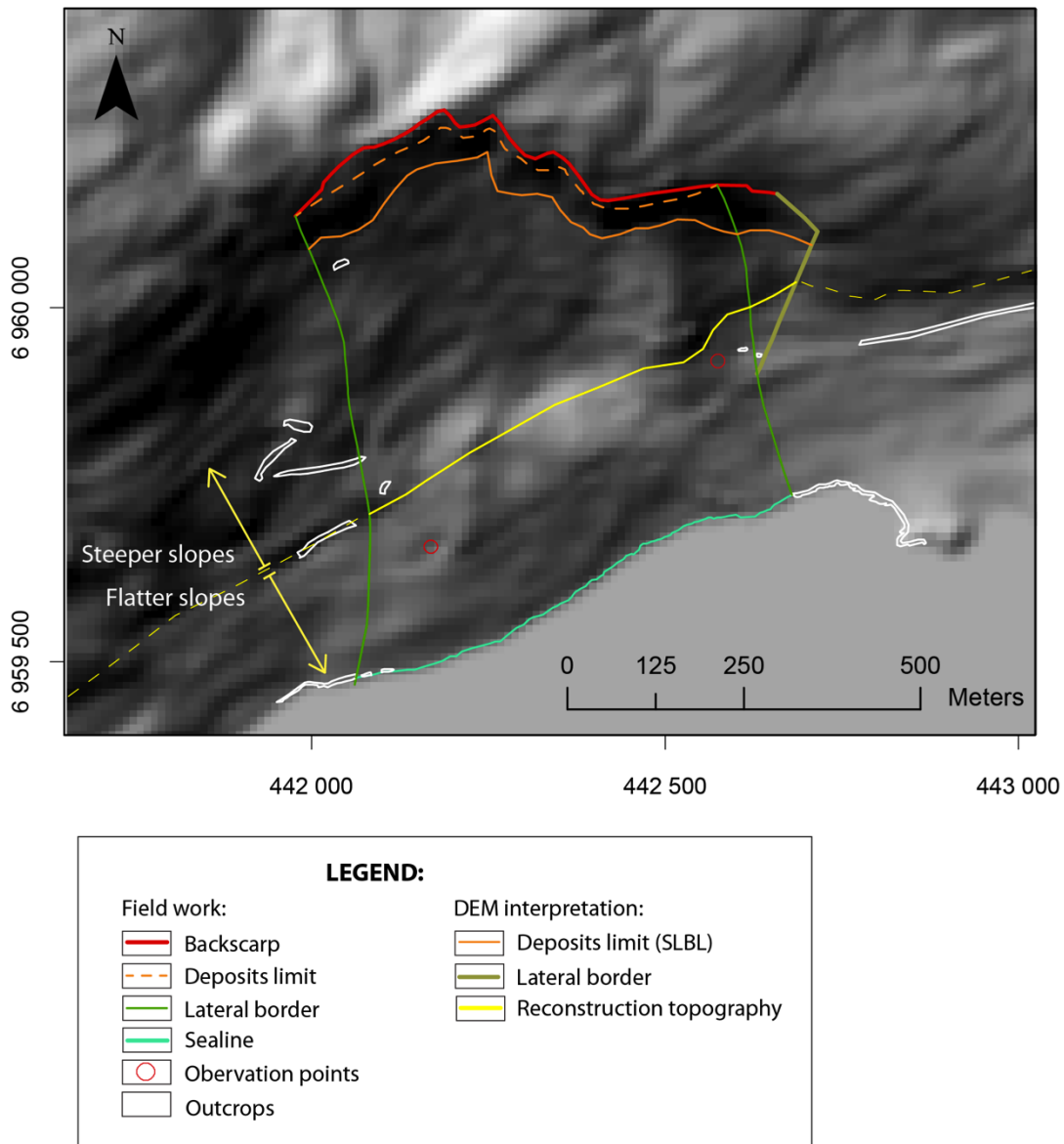
Figure 23: An overview of the drawn polylines from ArcGIS. The figure shows a clear boundary between steeper and flatter slopes making up the boundary of the reconstructed area (yellow border). The polylines result from interpretation of fieldwork and DEM. These polylines are further converted into polygons used in SLBL analysis by software CONEFALL.
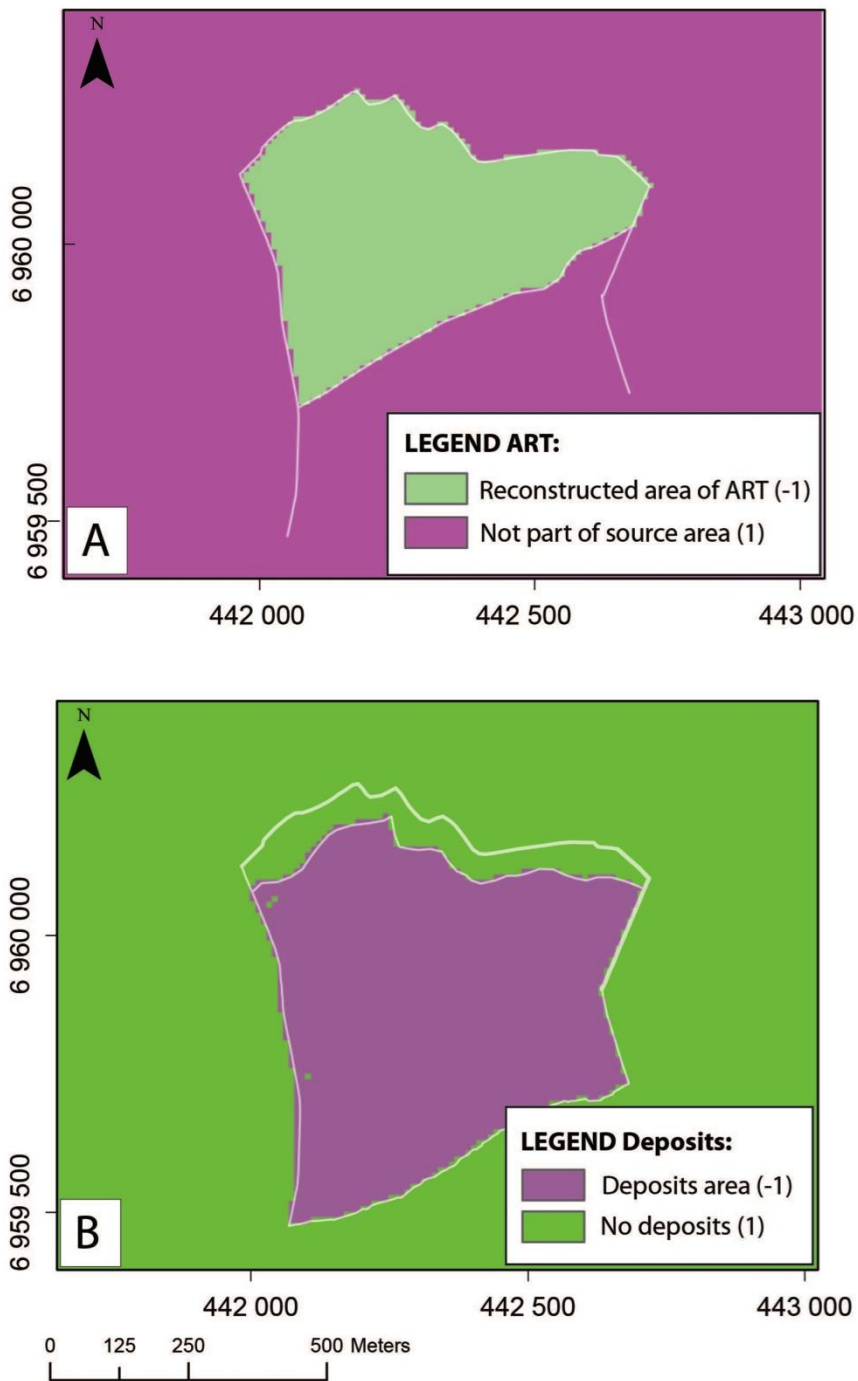
Figure 24: Defined fix points of the reconstruction (A) and deposits (B). Value of 1 represents stable areas with no deposits.

The SLBL algorithm is implemented into the CONEFALL software, where the lateral limits are the fixed-point files (source points). The software uses text grid files (ASCII) for the DEMs (both the normal DEM for the deposit volume estimations and the inverted DEM for the ART reconstruction) and the source points (deposits polygons and ART polygons) (Jaboyedoff and Labiouse, 2003). The tool "base level

simple" compute the base level surface using curvature tolerance (c), maximum thickness and input restrictions (e.g. iteration tolerance) as input parameters (Oppikofer, 2009).

The input values (h max/min/mean and length L) of the curvature (Figure 25, equation 3) are estimated based on a total of 6 profiles from ArcGIS combined with a straight line (c=0), see Figure 25. In the last step CONEFALL runs with the final average estimated curvatures (min, max and mean), and these output files are added into ArcGIS. The same procedure is also performed on the offshore part of the deposits using the bathymetry data of the Langfjorden.
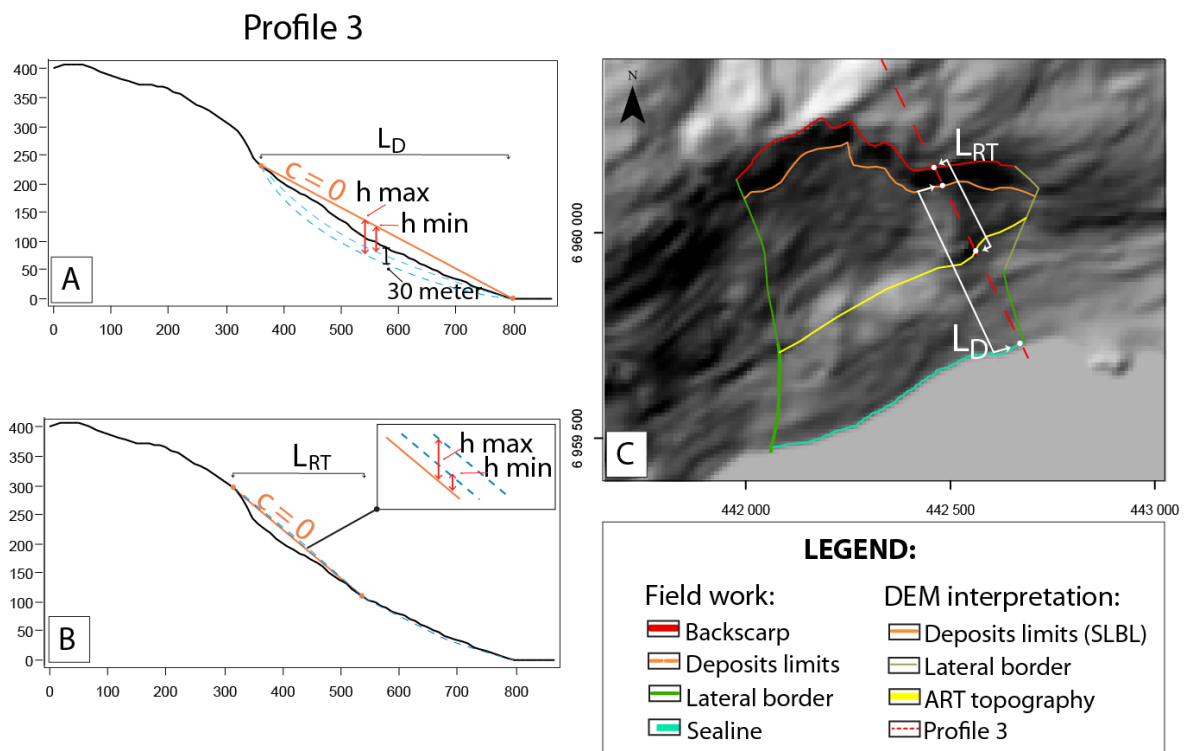
Figure 25: The parameter set up of SLBL using profile 3 as example, see dashed red line in C) for profile location. A) Shows interpretation of deposits thickness, and B) reconstruction of ART. A) and B) illustrate how parameters is decided in equation 3, where $L_{D/RT}$ = profile length of deposits/reconstruction topography, and h max/min= interpreted maximum/minimum thickness between the bedrock surface and a straight line (c = 0). Field observation was also included in the process of estimate the basal surface, as seen in A) included a field observation of deposits thickness 30 meters.

5.2.3. Volume calculation

The chosen curvature value for the reconstructed ART and for the deposit areas (onshore and offshore) is in the next step used to estimate the final volume of the rockslide. The estimations are conducted using zonal statistics in ArcGIS. Zonal statistics sums the values of a raster within the zones of another dataset and reports the results to a table. In this study the zonal input data is the respective polygons (Figure 27) and the estimated curvature values.

The height difference between the input rasters is summarized in a SUM table. The volume (V) of each polygon is calculated by multiplying the SUM value from the zonal output table with the DEM cell size (Oppikofer, 2012):

$$V = SUM \ \times \ 10m \ \times \ 10m \ [m^3]$$

<div align="right">Equation 6</div>

The total volume of Tjellefonna (V_{TOT}) is calculated based on the main polygons (Figure 26, Figure 27) combined with an equation from Oppikofer (2012):

$$V_{TOT} = (V_{ART} + V_{D\_ART}) \times 1.25\% = V_{D\_ONSHORE} + V_{D_{FJORD}}$$

<div align="right">Equation 7</div>

Where: V_{ART} = Volume of reconstructed ART

V_{D_ART} = Onshore deposits volume limited by the ART area

$V_{D\_ONSHORE}$ = Volume of total onshore deposits

V_{D_FJORD} = Volume of deposits in Langfjorden

Figure 26 is a profile sketch of the various volumes in equation 7. The reconstructed ART (V_{ART}) gives the volume of the initial rockslide, while the deposit ART area (V_{D_ART}) is the onshore deposit on top of the initial rockslide-gliding surface.
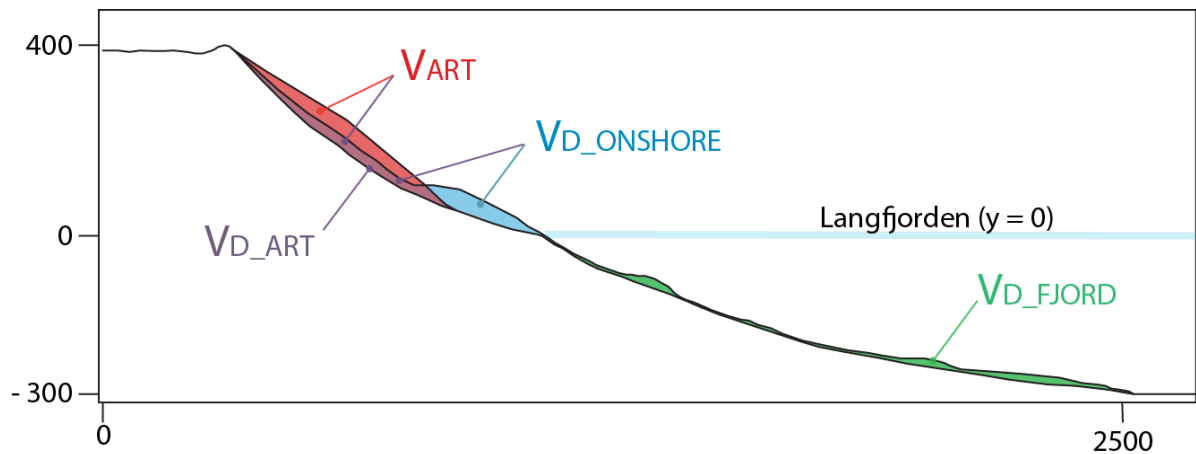
Figure 26: A profile sketch of the different volumes onshore and fjord. Note that the volume of the initial rockslide is composed of V_{ART} (reconstructed ART) and V_{D_ART} (onshore deposits volume limited by the ART area).
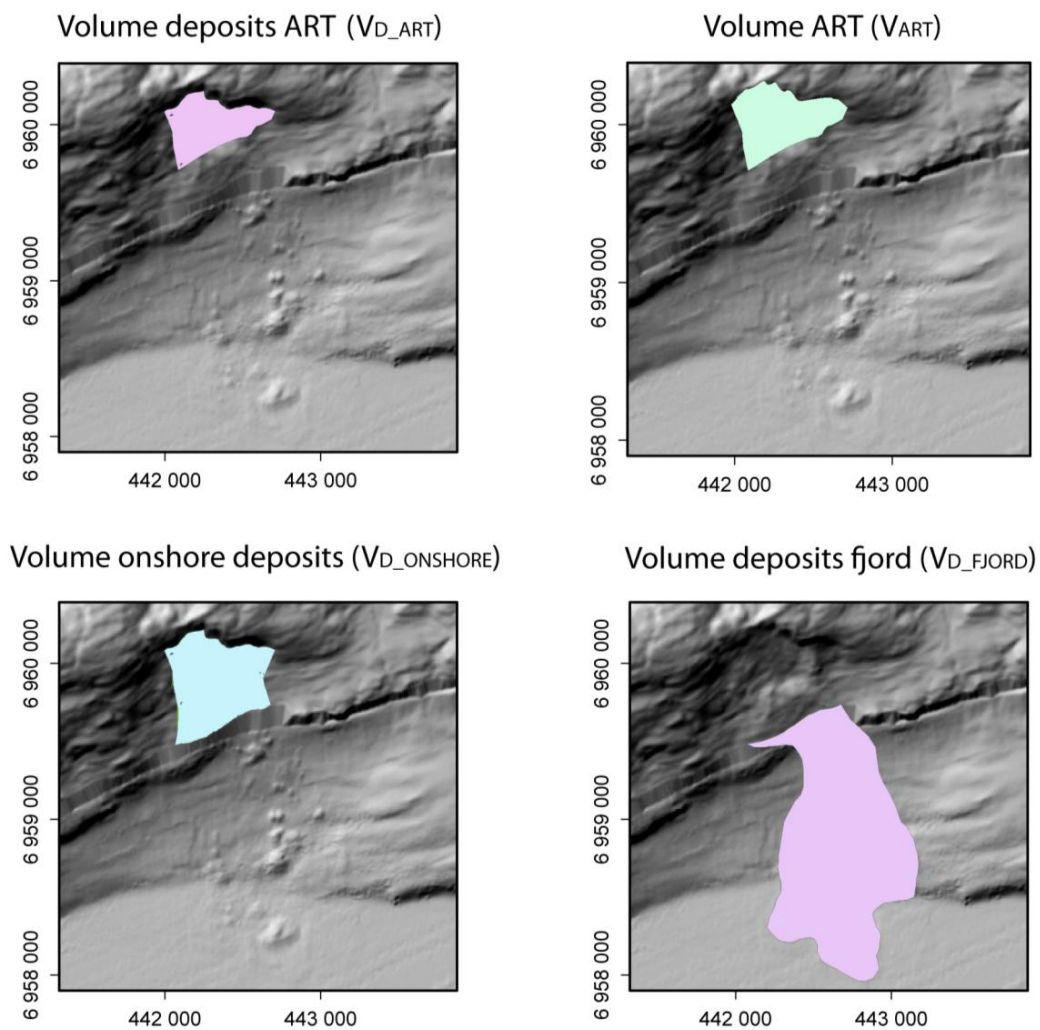
Figure 27: An illustration of the polygons used to estimate the total volume of Tjellefonna.

5.3. Numerical modelling: Phase^2

The numerical modelling of Tjellefonna is performed using the software Phase^2 (version 8.008) from Rocscience. Phase^2 is a continuous model using a elasto-plastic FEM, which may be used for a wide range of engineering purposes (e.g. support design, finite element slope stability, groundwater seepage and probabilistic analysis) (Rocscience, 2011). Phase^2 FEM divides the rock mass into small elements, which are connected to each other at certain points ("nodes"). The stresses are calculated inside these elements, while the displacement are related to the nodes (Scheldt, 2002). The resulting deformation and stresses are depending on the forces from the surrounding elements. Figure 28 shows the range of models offered in Phase^2, and a more detailed description of the applications and material models are given in the tutorial from Rocscience (2011).
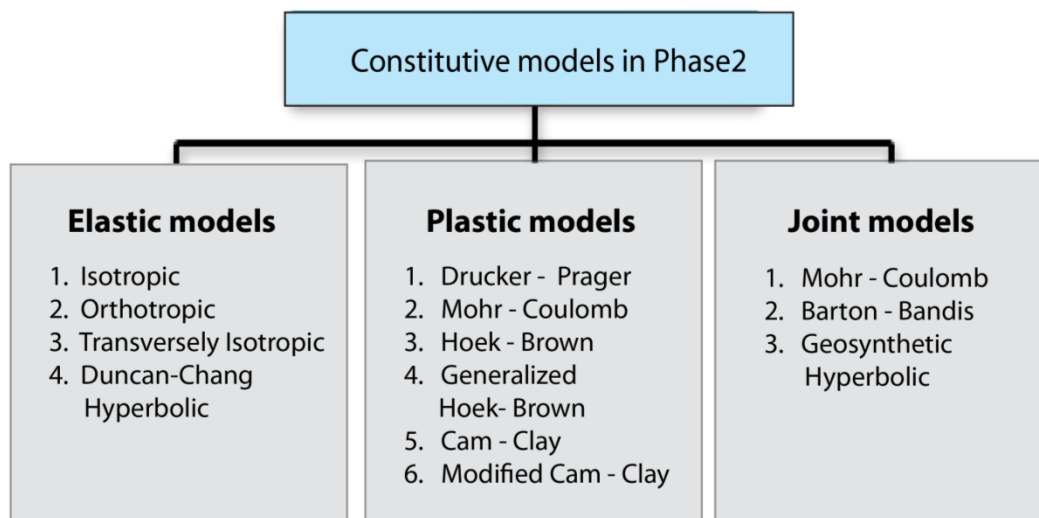
Figure 28: An overview of the models offered in Phase^2. Figure is modified from Grøneng (2010).

Shear strength reduction (SSR)

Phase^2 uses the Shear Strength Reduction (SSR) method to determine the Strength Reduction Factor (SRF) of a slope, which is equivalent to the factor of safety (FS). This option can be used with either Mohr-Coulomb or Hoek-Brown strength parameters. Phase^2 gives an opportunity to perform parameter studies based on the critical SRF of a slope (Rocscience, 2011). The safety factor in the FEM analysis is defined similarly as in the traditional limit-equilibrium analysis (Duncan, 1996).

Slope stability analyses with the SSR method are run for a series of increasing trial factors of safety (f)
SRF until failure occurs. The cohesion (c) and friction angle (φ) are reduced for each trial according to
the equations by Willie and Mah (2004):

$$c_{trial} = \left(\frac{1}{f}\right) c$$

Equation 8

$$\phi_{trial} = \tan^{-1}\left(\frac{1}{f}\right) \tan \varphi$$

Equation 9

The SSR method reduces the shear strength until the slope becomes unstable, and failure is defined as
the point when the FEM does not converge to a solution, i.e. when equilibrium cannot be maintained.
The critical SRF is the SRF value at failure. If the model consists of several stages, SSR will only be
carried out for the last stage of the model (Rocscience, 2011). An SSR search area may be applied if it
is necessary to restrict the stability analysis to a special area of the model.

5.3.1.   Model set up

The model consists of two stages: 1) an initial stage as a box and 2) excavation reflecting glacial
erosion based on recommendation from Böhme (2012).

The chosen profile size (Figure 29) is based on recommendations by Wyllie and Mah (2004) to avoid
boundary effects, since artificial boundaries do not exist in reality. Artificial boundaries may influence the
analysis by prescribed displacement, or prescribed stress. Table 7 gives an overview of the boundaries
set up of Tjellefonna. Figure 30 shows the final profile used in Phase[2,] and the location of the profile is
illustrated in Figure 31. The manual reconstructed profile is based on a combination of ART from SLBL
and PolyWorks. A SSR search area is applied to restrict the analysis to the 1756 failure area.

The analyses are conducted with a mesh set up of 6-node triangles, based on recommendation from
Hammah et al. (2006). The mesh is build up of 800 elements, which are recommended from
Rocscience (2011). The stresses are simulated with a tolerance of 0.001 and the maximum amount of
iterations is set to 500 (Gaussian type).
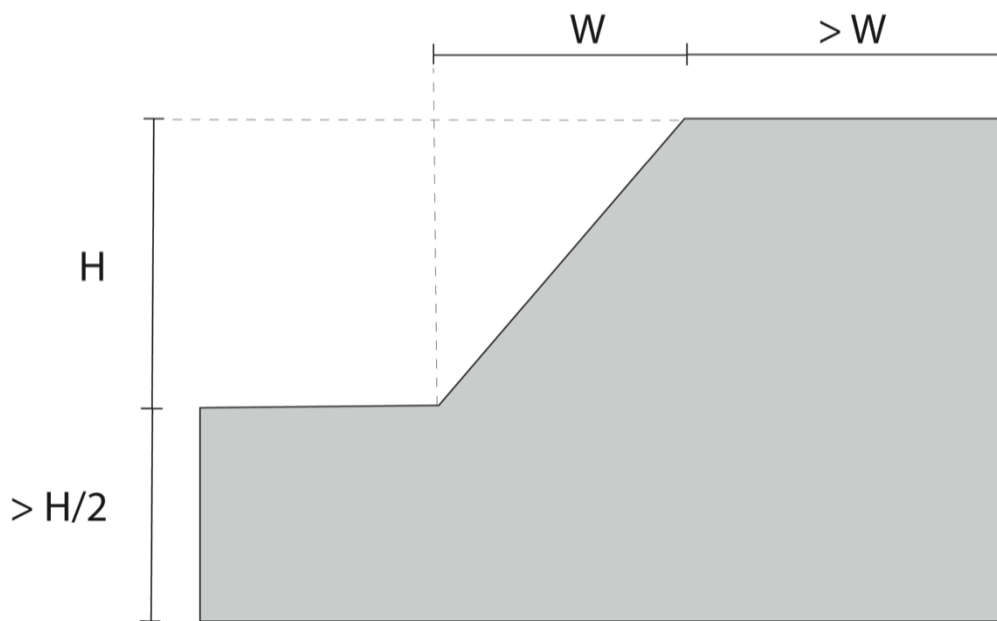
Figure 29: Recommendations on model size to avoid artificial boundaries. The illustration is modified from Wyllie and Mah (2004).

Table 7: Boundary setup of the Tjellefonna rockslide.

Boundary conditions:	Recommendations:
• Surface of the model free to move in all direction	(Rocscience, 2011)
• The left and right vertical boundaries are allowed to move in the *vertical* (y) direction, but not in the horizontal (x). This allows deformation and prevents stress concentration.	(Farsund, 2011; Grøneng, 2010; Sandøy, 2011c)
• Additionally bottom line locked vertically, but the lower corners where free to move *horizontally.*	(Grøneng, 2010; Sandøy, 2011c)
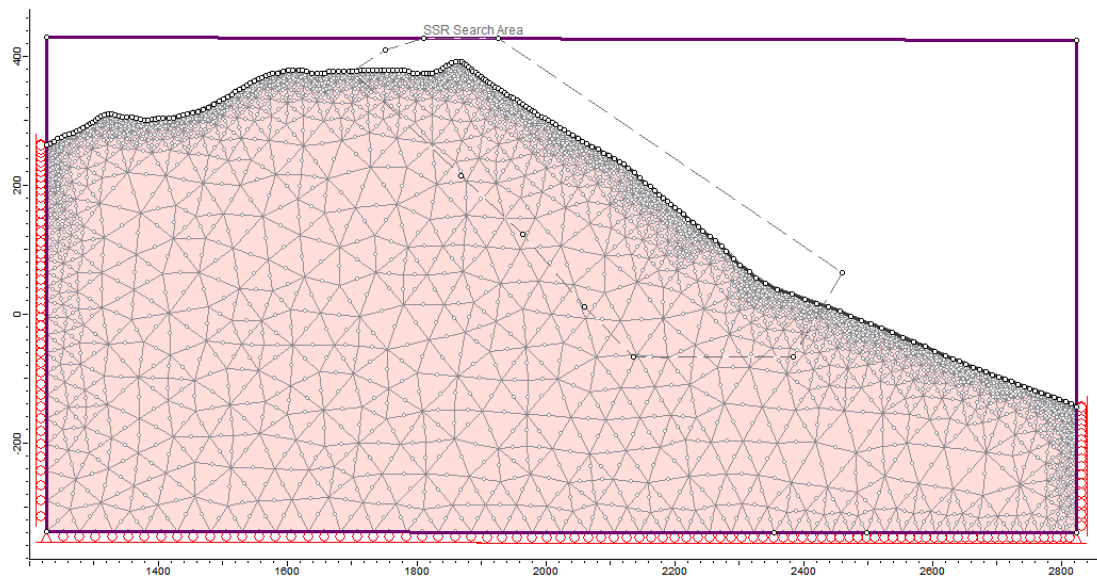
Figure 30: The final profile chosen for Phase[2] with SSR search area. Reconstruction of the topography is based on PolyWorks and SLBL profiles.
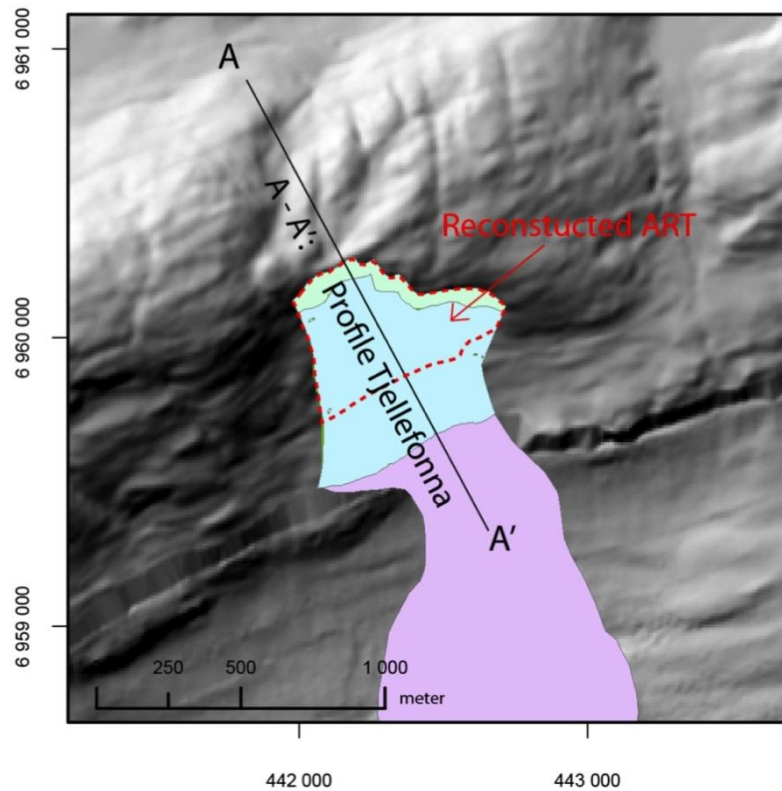
Figure 31: The location of profile A – A' used in phase[2]. The red stippled lines show the interpreted ART (failed area).

5.3.2.   Rock mass parameters

Failure criterions

There are several failure criterions to describe the strength and deformation capability for rock mass in modelling, where classical linear Mohr-Coulomb criterion is the most applied (Hoek, 2007):

$$\tau = c + \sigma_n \tan \varphi$$

<div align="right">*Equation 10*</div>

Where: τ = Shear stress
c = Cohesion
σ_n = Normal stress acting
φ = Friction angle of the material

Phase[2] also allow the non-linear empirical Hoek-Brown failure criterion (Rocscience, 2009). This criterion is more suitable for predicting failure of rock masses compared to the Mohr-Coulomb criterion (Hammah et al., 2004). The generalized Hoek-Brown criterion for jointed rock mass is (Hoek, 2007):

$$\sigma'_1 = \sigma'_3 + \sigma_{ci} \left(m_b \frac{\sigma'_3}{\sigma_{ci}} + s \right)^a$$

<div align="right">*Equation 11*</div>

Where: σ'_1 and σ'_3 = minimum and maximum effective principle stresses at failure

σ_{ci} = uniaxial compressive strength of the intact rock mass

m_b = value of the Hoek-Brown constant m for the rock mass,
given by $m_b = m_i e^{\left(\frac{GSI-100}{28-14D}\right)}$
s and a = constant which depending upon the rock mass characteristics,
given by: $s = e^{\left(\frac{GSI-100}{9-3D}\right)}$ and $a = \frac{1}{2} + \frac{1}{6}\left(e^{-GSI/15} - e^{-20/3}\right)$

The Hoek-Brown criterion assumes isotropic rock mass and therefore needs to be applied in a rock mass with sufficiently number of closely spaced discontinuities. The closely spaced discontinuities must have similar surface characteristics and isotropic failure behaviour. However, when one of the discontinuity sets is significantly weaker than other, or if few (one or two) discontinuities dominate the rock mass, the Hoek-Brown criterion should not be used (Hoek, 2007).

Conversion from Hoek-Brown to Mohr-Coulomb criterion using RocLab

Hoek-Brown criterion is preferred in this thesis because the basal surface is unknown, and the criterion suits best the fractured rock mass at Tjellefonna (Nilsen, 2012). Unfortunately a SSR analysis with Hoek-Brown criterion is not easy to analyse based on the input data (m_b, s and a) in Phase[2]. However, the generalized Hoek-Brown criterion can still be used according to (Hammah et al., 2004), by converting the parameters into Mohr-Coulomb failure envelope using RocLab, and then applying the equivalent cohesion and friction angle in the standard SSR. Unfortunately there are some challenges to obtain the friction angle and cohesion. The so-called active friction angle is not a constant, but highly variable depending on the actual normal stress level (Nilsen, 2000). It is important to be aware of that the relationship between shear strength and normal stress is non-linear, which means that the normal stress needs to be calculated before the cohesion and friction angle may be determined (Nilsen et al., 2011). The non-linear relationship is taken into consideration with the "Instantaneous Mohr-Coulomb" calculated in RocLab (Loftesnes, 2010), which estimate the peak strength parameter from the specific normal stress (Appendix 2). A mean value of normal stress is calculated based on the rock mass unit weight (γ), overburden to basal surface (z) and the basal surface angle (α_{slope}) using following equation:

$$\sigma_n = \gamma z \cos \alpha_{slope}$$ *Equation 12*

The reconstructed overburden range from about 10 meter to 65 meters (mean 38 meter), with an average dip of 30° obtained from the SLBL. A density of 2770 kg/m^3 results in a normal stress of 0.2 – 1.5 MPa with mean value of 1 MPa (Profile 2 in Figure 40; chapter 6.1.3).

Table 8 gives an overview of input and output parameters in RocLab, where the peak cohesion and friction angle is based on the Hoek-Brown parameters. Results from Sandøy (2011b) reveal that the geological strength index (GSI) have an average value of 50. This average rock mass quality corresponds to a blocky structure defined by discontinuity surfaces, where the surface is smooth and moderately weathered and altered. The intact rock parameter (m_i) is estimated as a mean value from granite, gneiss and diorite in RocLab. The disturbance factor (D) expresses the mechanical stresses that the rock mass have been exposed to, e.g. weathering, erosion and glaciation. The parameter is chosen after recommendations of Loftesnes (2010) to be equal to 0.5, as smooth blasting have a D-value of 0.7.

Table 8: Input parameters needed to estimate Hoek-Brown criterion parameters for Phase2. Instantaneous Mohr-Coulomb peak friction and cohesion is given from a mean normal stress of 1 MPa (Appendix 2).

	Parameters:	Symbol:	Values:	Source:
Input	Uniaxial Compressive Strength (UCS)	σ_{ci} [MPa]	161	Laboratory tests 2011 (Sandøy, 2011b)
	Intact rock parameter	m_i	26	RocLab estimations (Sandøy, 2011b)
	Geological Strength index	GSI	50	Field work 2011 (Sandøy, 2011b)
	Disturbance factor	D	0.5	(Loftesnes, 2010)
	Young's modulus	E_i [GPa]	63	Laboratory tests 2011 (Sandøy, 2011b)
	Mean normal stress	σ_n [MPa]	1	Estimation based on Equation 12, and interpretation of sliding plane.
Output	Deformation modulus	E_m [MPa]	9257	RocLab estimations
	Peak Friction angle	ϕ_{peak} [°]	62	RocLab estimations, 1 MPa
	Peak cohesion	c_{peak} [MPa]	0.8	RocLab estimations, 1 MPa
	Tensile strength	σ_t [MPa]	-0.085	RocLab estimations, 1 MPa

Elastic and plastic material

Hoek-Brown and Mohr-Coulomb uses peak shear strength to describe failure within the rock mass (Figure 32), as peak strength parameter describe failure within *elastic* rock mass, and residual values within *plastic*. Previous shear stress experiments show that as the displacement continues, the shear stress will fall to some residual value that will stay constant (even for large displacements) (Hoek, 2007).

Phase2 allows elastic and/or plastic analysis of slope stability. Numerical modelling of Tjellefonna is run both with an elastic-plastic model (peak values equal residual)., and with various strain-softening models. These analyses were performed with stain-softening reduction of both cohesion and friction angle in the order of 10, 30 and 50 % of peak values.
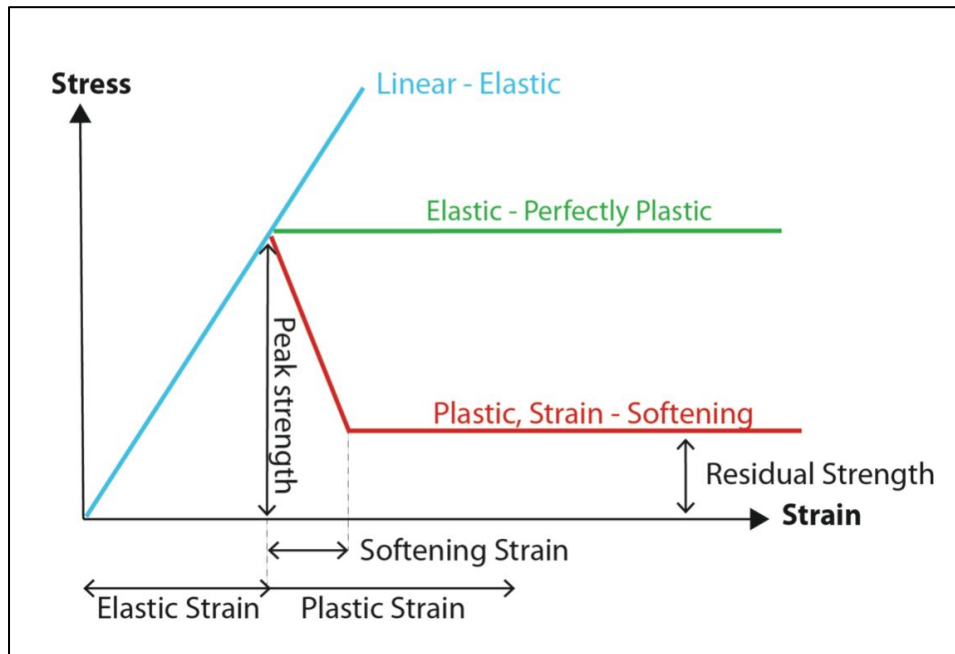
Figure 32: Stress – Strain relationship modified from Sjoberg (1999). The figure shows the difference between elastic and plastic behavior, where residual strength represent the plastic strain-softening model.

5.3.3. Structural settings

The importance of discontinuities and tectonic structures like faults have been included based on the fieldwork described in Sandøy (2011b). The numerical modelling includes the main setup of two joint sets (J1, J5) as well as two parallel discrete fault zones (Fault-set 1). Also a sub-horizontal fault (Fault-set 3) is included in the modelling in the last analysis. The back walls are built up of a combination of a well persistent joint set J1 (157/59) and the parallel faults. A wider-spaced shallow-dipping joint set J5 (160/27) is included, although rarely seen in field. Taking long computing times into consideration, the real spacing of J1 is exaggerated from around 1 meter to 30 meter. The real spacing distance of J5 is harder to define because of the scarcity of these structures in field. Because of this the spacing of J5 is analysed with both 300 meter and 30 meter spacing.

Mohr-Coulomb cohesion and friction angle are still the most applied parameters to calculate the SRF. However, since 1970 it has been recognised that the relationship between shear strength and normal stress for discontinuities is better represented by non-linear Barton-Bandis relationships. This relationship is not expressed in terms of cohesion and friction angles, which are required in Phase^2 joint parameters. The Barton-Bandis parameters (φ_r, JRC, JCS) are recalculated into Mohr Coulomb

instantaneous cohesion (c_i) and friction angle (φ_I) based on the equations from Hoek (2007). The calculations are given in Appendix 3, and the results listed in Table 9.

Table 9: instantaneous cohesion c_i and friction angle φ_i.

Normal stress: 1 MPa	J1:	J5:
Shear strength [MPa]	0.62	0.92
φ_i [°]	35.5	45
c_i [KPa]	58	127

Fault parameters are set equal the ones found in Grøneng (2010) for gouge-filled faults in gneiss, giving a mean of $\varphi = 25$ and $c = 0$. The influence of the weakness zones on the slope stability is tested, as well as the effect fault widths: Fault-set 1 (inserted as two joints; Figure 33) and Fault-set 2 (two material of around 1-2 meter wide; Figure 35)

An additional joint parameters included in Phase[2] are the normal and shear joint stiffness (Table 10). The joints elastic behaviour is specified by joint normal (k_n) and shear (k_s) stiffness (linear or piece-wise linear). The stiffness of J1 and J5 are estimate from the rock mass modulus (E_m), the intact rock modulus (E_i) and the joint spacing. Please refer to Rocscience (2011) for more details and Appendix 4. Fault stiffness values are based on the recommendations from Böhme (2012) and Wines and Lilly (2003).

Table 10: Estimation and assumed values of joint stiffness.

Joint stiffness:	J1:	J5:	Fault:
k_n [MPa/m]	7234	2170	100
k_s [MPa/m]	2989	897	100

5.3.4. Stresses

The importance of in-situ stresses has traditionally been ignored in slope analysis, and some possible reasons for this are listed below (Wyllie and Mah, 2004):

- Stresses in rock masses are not routinely measured for slopes
- Widely use of limit equilibrium, which cannot include the effect of stresses
- Main part of rock slides are gravity driven and the in-situ stresses are interpreted to be minimal

The results from numerical analyses by Lorig (1999) show that in-situ stresses have no major effect on the SRF. However, the in-situ stresses have significant influence on the *deformation,* and because of this also on the stability. If the slope is build up of materials that weaken as a results of internal deformation, then the in-situ stresses have a vital and important role in reducing strength and affecting stability (Hoek et al., 2000).

In Phase[2] the stress field can be defined either as a constant or as gravity. Gravity field stress option is used when an in-situ stress field varies with depth, and is regularly used for surface or surface excavation (like slopes) (Rocscience, 2011). The state of the stress is determined by the current loading and geological history of the area (Hanssen, 1998). In a relaxed environment, where the rock mass behaves elastic, the vertical component are given by the unit weight (γ) and depth (z) (Sheorey, 1994):

$$\sigma_v = \gamma z \qquad\qquad\qquad Equation\ 13$$

The horizontal component is given by the poisons ratio (ν) and vertical component (σ_v) (Sheorey, 1994)::

$$\sigma_h = \frac{\nu}{1 - \nu}\sigma_v \qquad\qquad\qquad Equation\ 14$$

The equations above are not the best approach in Norway, since the horizontal component are influenced by tectonic forces (like faulting, isostasy and erosion) (Nilsen, 2012). It therefore seems that the ratio between σ_h and σ_v is not constant with depth (Goodman, 1989). In equation 15 these factors are summed as (σ_l) and may act as an addition to the horizontal stress (Sandøy, 2011c):

$$\sigma_h = \frac{\nu}{1 - \nu}\sigma_v \pm \sigma_l \qquad\qquad Equation\ 15$$

Tjellefonna clearly lies in a tectonically active area (related to the MTFC), and using Equation 14 would underestimate the in-situ stresses. Table 11 gives an overview of stress measurements at two nearby localities (Rødsand and Hustad), and the mean values used for the modelling: σ_H of 9.3 MPa and σ_h of 3.2 MPa. The major horizontal component represents the in-plane stresses with similar orientation as Tjellefonna dip direction (~160°), with only a minor out-of plane component.

Table 11: Overview of measured of major (σ_H) and minor (σ_h) horizontal component of the measured 3D stress field, and additional the major orientation. The values are modified from Hanssen (1998).

Locality:	σ_H [MPa]:	σ_H [°]:	σ_h [MPa]:	σ_h [°]:	σ_v [MPa]:
Rødsand gruver, Nesset Kommune	10.9	158	6.5	68	10.2
Hustad, Fræna Kommune	7.7	171	3.2	81	5.3
Tjellefonna mean:	**9.3**		**4.9**		**7.8**

5.3.5. Water

It is not observed any lakes or river in the rockslide area, but a large marsh area is located on the crown. Historical sources describe observations of water running into tension cracks of the present-day crown area (see chapter 1), which may have led to a build up of water pressure in the fractured rock mass. These sources also state that it had been raining heavily for 14 days before the event. Because of this the modelling is carried out with three scenarios:

- Dry slope
- Moderately saturated slope (normal groundwater table)
- Extremely saturated slope (high groundwater table)

5.3.6. Effect of earthquakes

Phase[2] allows the user to apply a pseudo-static seismic load. This load is defined by entering horizontal and/or vertical seismic coefficient. The effect of an earthquake is modelled as a permanent body force applied vertically, added to each element in the mesh. The seismic force F_s is given by (Rocscience, 2011):

$$F_S = kW_{FE}$$

Equation 16

Where W_{FE} is the weight of each finite element and k is the seismic coefficient expressed by Jibson (2011):

$$k_{h,v} = {a_{h,v}}/{g} \qquad\qquad \textit{Equation 17}$$

Equation 17 involves the horizontal (a_h) or vertical (a_v) ground acceleration caused by the seismic activity and g, the acceleration of the Earth's surface. The study of Jibson (2011) reveals that the effect of vertical forces tend to average out to near zero when using a psudostatic seismic analysis, due to the simplification of the earthquake shake as a permanent body force. The recommendations for selecting k values are listen in Table 12 (Jibson, 2011):

Table 12: Recommended values of seismic coefficient, depending on the earthquake magnitude from varies studies. Table modified from Jibson (2011).

Seismic coefficient (k):	Earthquake magnitude:		Source:
0.10	R-F*: IX	Extremely strong shock	Terzaghi (1950)
0.20	R-F: X	Shock of extreme Intensity	
0.50	R-F > X		
0.10	M** = 6.50		Seed (1979)
0.15	M = 8.25		
0.15	N/A		CDMG" (1997)

R-F* = Rossi-Forel earthquake intensity scale

M** = Earthquake magnitude

CDMG" = California Division of Mines and Geology

Based on a mean seismic magnitude of 2.7 in the Møre & Romsdal area a seismic horizontal coefficient of 0.044 is used in the model, and as a worst-case scenario of magnitude 8.25 a k value of 0.15 is used. The vertical seismic coefficient is chosen to be ¼ of the horizontal coefficient throughout all analyses. The model is tested with different combinations and directions of horizontal and vertical k after recommendations from Rocscience (2011). The chosen direction is based on the worst-case results. The seismic load is applied at the final stage of the excavation.

5.3.7. Summary of scenarios and input parameters

Model set up

Table 13 shows the three main structural settings that were applied to the modelling.

Table 13: Different model settings used in the numerical analyses.

Model:	Set up:	Spacing J1/J5 [m]:	Illustration:
1	J1, Fault-set 1	30/ -	Figure 33
2	J1, J5, Fault-set 1	30/300	Figure 33
3	J1, J5, Fault-set 1	30/30	Figure 34

Scenarios

The Phase^2 analyses were conducted through a total of 5 main analyses. An overview is listed below:

- **Analysis 1**: Elastic – perfectly plastic model, peak values equal residual   values.

    Analysis 1.1: Faults

    Analysis 1.2: Elastic – perfectly plastic models.
    Setup of Model 1 and Model 2.

- **Analysis 2:** Strain softening model (residual = 10, 30 and 50 % of peak friction angle and cohesion), k = 0. Setup of Model 2.

- **Analysis 3:** strain softening model (residual = 10, 30 and 50 % of peak friction and cohesion), k = 0.044. Setup of Model 2.

- **Analysis 4:** The role of discontinuity set J5 on slope stability (Parameter study of friction angle, cohesion and spacing).

Analysis 4.1: SRF influence of friction angle (φ) and cohesion (c). Setup of Model 2.

Analysis 4.2: J5 spacing and friction angle (φ) reduction. Setup of Model 2 (spacing 300 meters) and Model 3 (spacing of 30 meters).

Analysis 4.3: Triggers influence of various spacing and friction angle (φ). Set up of Model 2 (spacing of 300 meters) and Model 3 (spacing of 30 meters).

- **Analysis 5:** Influence of sub-horizontal fault. Fault-set 3 is included in Model 1 and Model 2.

Trigger factors like earthquake and groundwater are variably applied in the different analyses. The analyses consist of mainly two models: model 1 (J1, Fault-set 1) and model 2 (J1, J5, Fault-set 1) (Figure 33). Also the impact of the fault zone width has been investigated with comparison of Fault-set 1 (Figure 33) and Fault-set 2 (Figure 35). Table 14 gives an overview of the parameter studies:

Table 14: An overview of analyses and models run with different parameter studies.

Analyses:	Model:	Including:	Parameter study (incl. trigger factors):
2 - 3	1	J1, Fault-set 1, gw	Rock mass, J1 (φ_{res} and c_{res})
2 - 3	2	J1, J5, Fault-set 1, gw	Rock mass, J1, J5 (φ_{res} and c_{res})
4	3	J1, J5, Fault-set 1	J5 (spacing, φ_{peak}, c_{peak})
5	2	J1, J5, Fault-set 1, Fault-set 3	Flat laying fault (Fault-set 3)
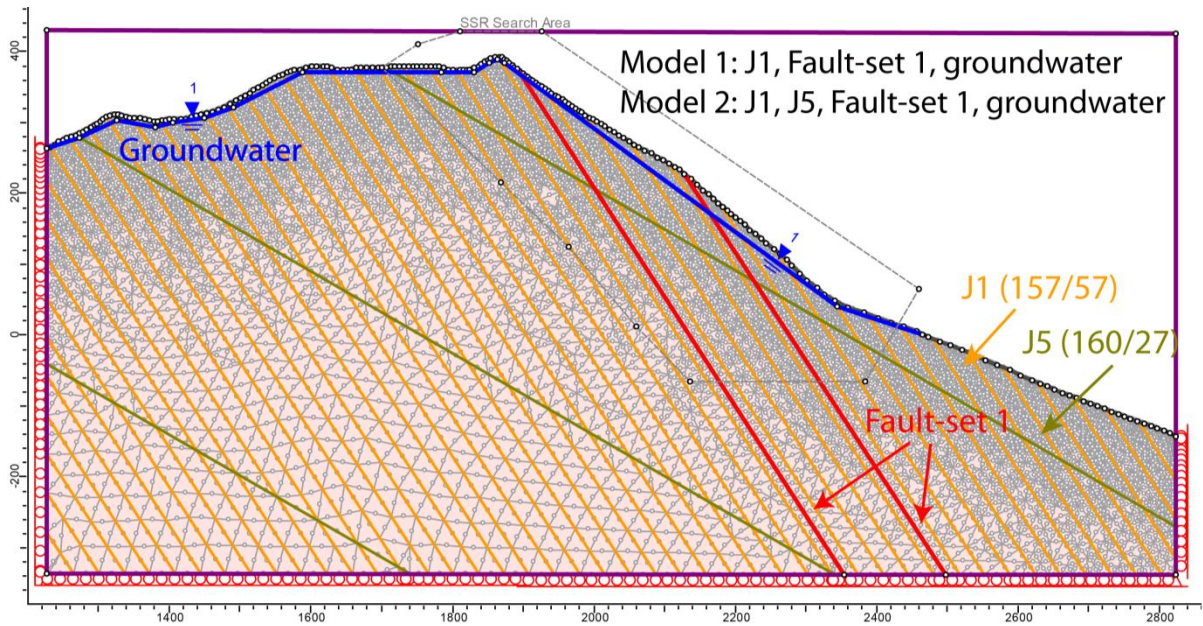
Figure 33: The investigation of SRF was mainly run with model 1 (J1, Fault-set 1) and model 2 (J1, J5, Fault-set 1). Also with higher groundwater, earthquake and wider fault zones (Fault-set 2). Note that J5 have a spacing of 300 meters.
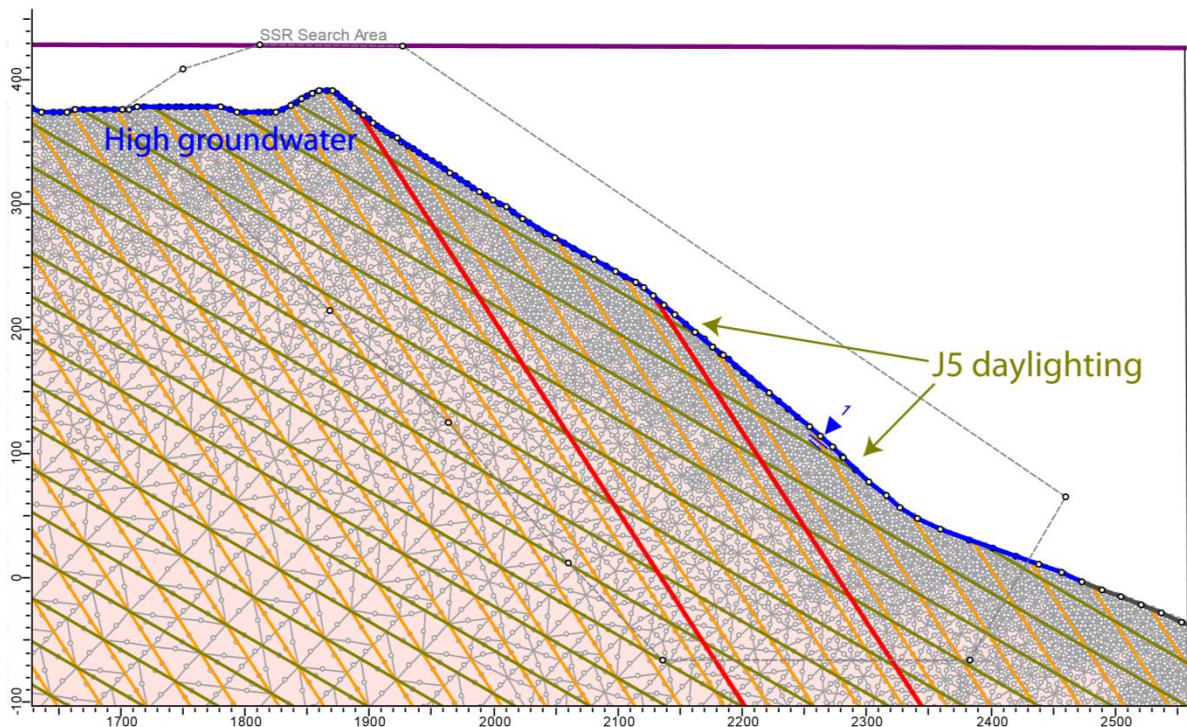
Figure 34: Set up of Model 3, where J5 has a spacing of 30 meters (equal to J1). Notice that J5 is now daylighting the slope face.
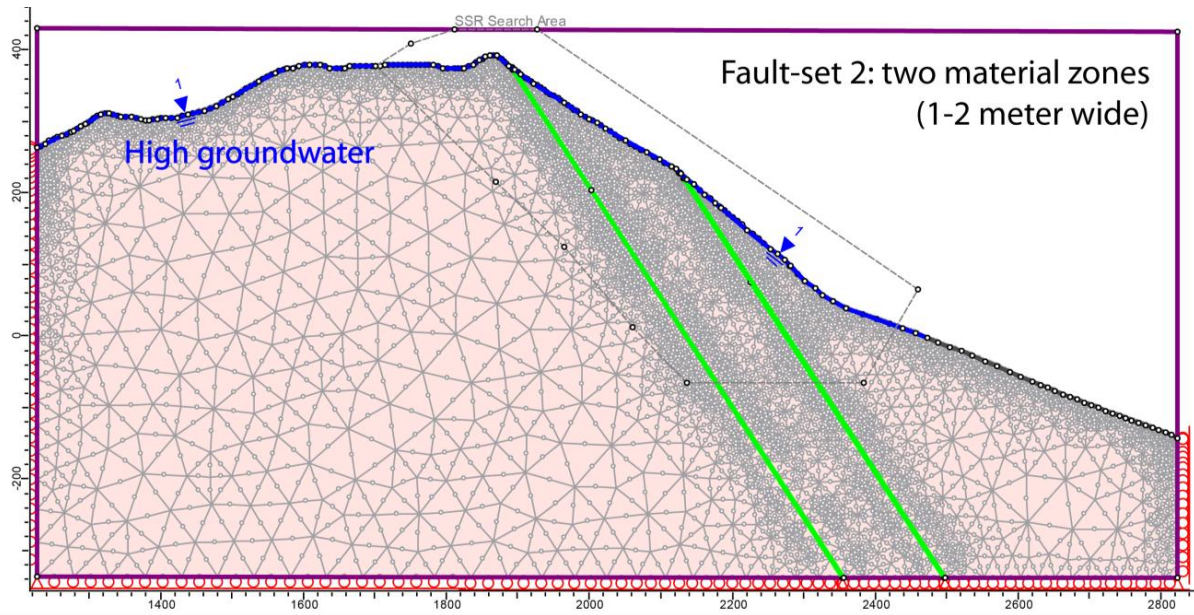
Figure 35: Illustration of higher groundwater and thicker fault zones drawn as material boundaries of 1 – 2 meter wide.
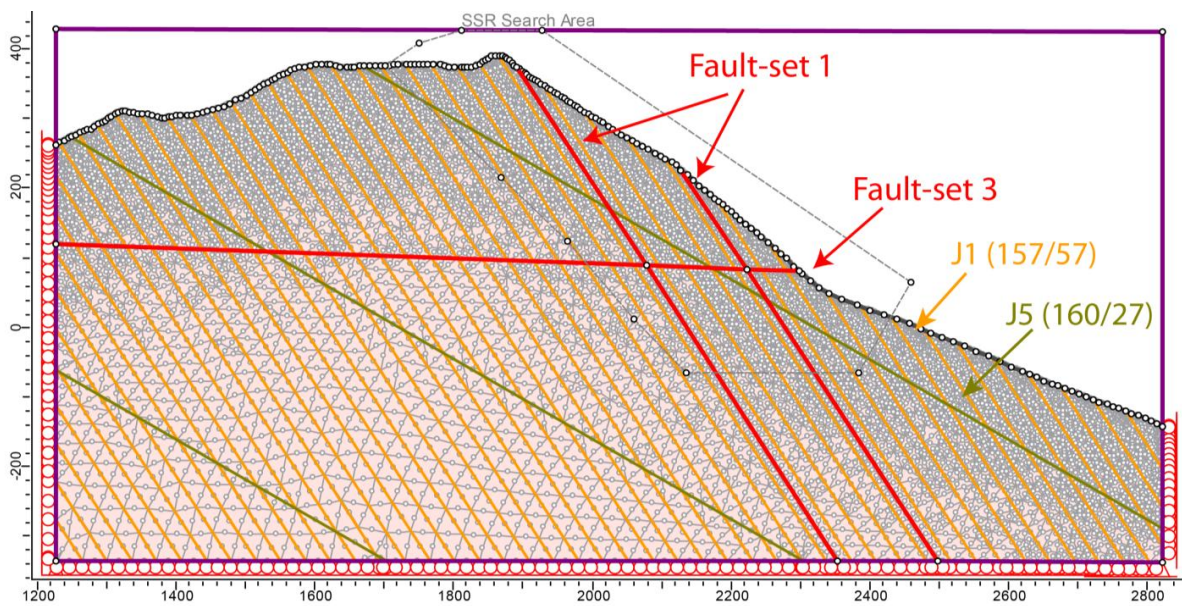
Figure 36: Set up of Model 3 including same geological settings as Model 2, and additional a sub-horizontal fault (Fault-set 3).

General settings and parameters:

Table 15: General settings in Phase[2] .

General settings of Tjellefonna modelling		
Analysis type:		Plane strain
SSR	Stop criteria:	Square root energy
	Tolerance:	0,001
	Maximum number of iterations:	500
Convergence type:		Absolute energy
Mesh	Type	Graded
	Element type	6 noded triangles
	Number of excavation nodes	800
Boundary conditions		Bottom: restrain y
		Left: restrain x
		Right: restrain x
		Top (surface): free
		Lower corners: restrain x,y
Stresses	Gravity	Unit weight: 0.027
		Total stress ratio (σ_H/σ_v) <u>in plan</u>: 9.3/7.8 =1.2
		Total stress ratio (σ_h/σ_v) <u>out-of-plane</u>: 4.9/7.8 = 0.6
		Locked-in-horizontal stress: 0

Table 16: Input parameters granitic to granodioritic gneiss. The RocLab results are based on fieldwork from 2011.

Parameters (Tjelle bedrock):					Source:
Young's modulus (Rock mass)	E_m[GPa]	9.3			From RocLab
Poissons ratio	ν	0.21			Laboratory analysis
Peak values	c_{peak}	0.8			From RocLab
$\sigma_n = 1$ MPa	φ_{peak}	62			From RocLab
	σ_t	-0.085			From RocLab
Residual values	c_{res}	56	43	31	
	φ_{res}	0,72	0,56	0,4	10, 30, 50 % of peak
	σ_t	0,077	0,06	0,04	

Table 17: Input parameters of J1 and J5.

Parameters:	Joint set J1:			Joint set J5:			Source:
c_{peak} [Mpa]	58			127			Field work and Hoek
φ_{peak}	35			45			(2007)
c_{res} [Mpa]	0.052	0.04	0.03	0.11	0.089	0.063	10, 30, 50 % of c peak
φ_{res}	32	25	18	41	32	23	10, 30, 50 % of φ peak
k_n [MPa/m]	7234			2170			Field work and RocLab
k_s [MPa/m]	2989			897			

Table 18: Fault input parameters.

Parameters:	Fault values:	Source:
c_{peak}	0	(Grøneng, 2010)
φ_{peak}	25	
K_n [MPa/m]	100	(Böhme, 2012; Wines and Lilly,
K_s [MPa/m]	100	2003)

6.   Results

6.1. Reconstruction and volume estimation of Tjellefonna

Two modern techniques are used in this master thesis to reconstruct the failed topography and to calculate the volume of the Tjellefonna rockslide: Slope Local Base Level (SLBL) implemented in the CONEFALL software and the PolyWorks software (see Chapter 5.2.2)

6.1.1. Curvature values

The curvatures (min, max, mean) are estimated from equation 3, based on 6 profiles from both the onshore and the offshore parts. The final chosen curvatures are based on a recommended 25 % volume increase of the deposits due to fragmentation, and is in the final step implemented into CONEFALL.

Figure 37 shows the SLBL results based on curvature values: -0.01238 (reconstructed topography), -0.08159 (deposits onshore) and -0.0066 (deposits in the fjord). The failed rock mass, shown as reconstructed topography in Figure 37, has a peak elevation (50 to 70 meters) concentrated in the middle parts of the area. Furthermore, the onshore deposits have a zone with highest elevation (40 to 70 meters) just above the shoreline, which can be recognized in Figure 38 representing an area of deposit accumulation with flatter slopes. Notice that the SLBL results of the offshore part has a curvature that does not cover the whole area (Figure 37), yet the deposits have smaller zones with large deposit thicknesses, ranging from 20 to 40 meters. The final curvature values used in the SLBL model are chosen based on an expected volume increase of the deposits of 25% (including onshore and fjord). It was found that a volume increase of 24 % was best fitting for Tjellefonna (Appendix 5) when the deposits onshore had a curvature of -0.08159. This criterion will be discussed later.
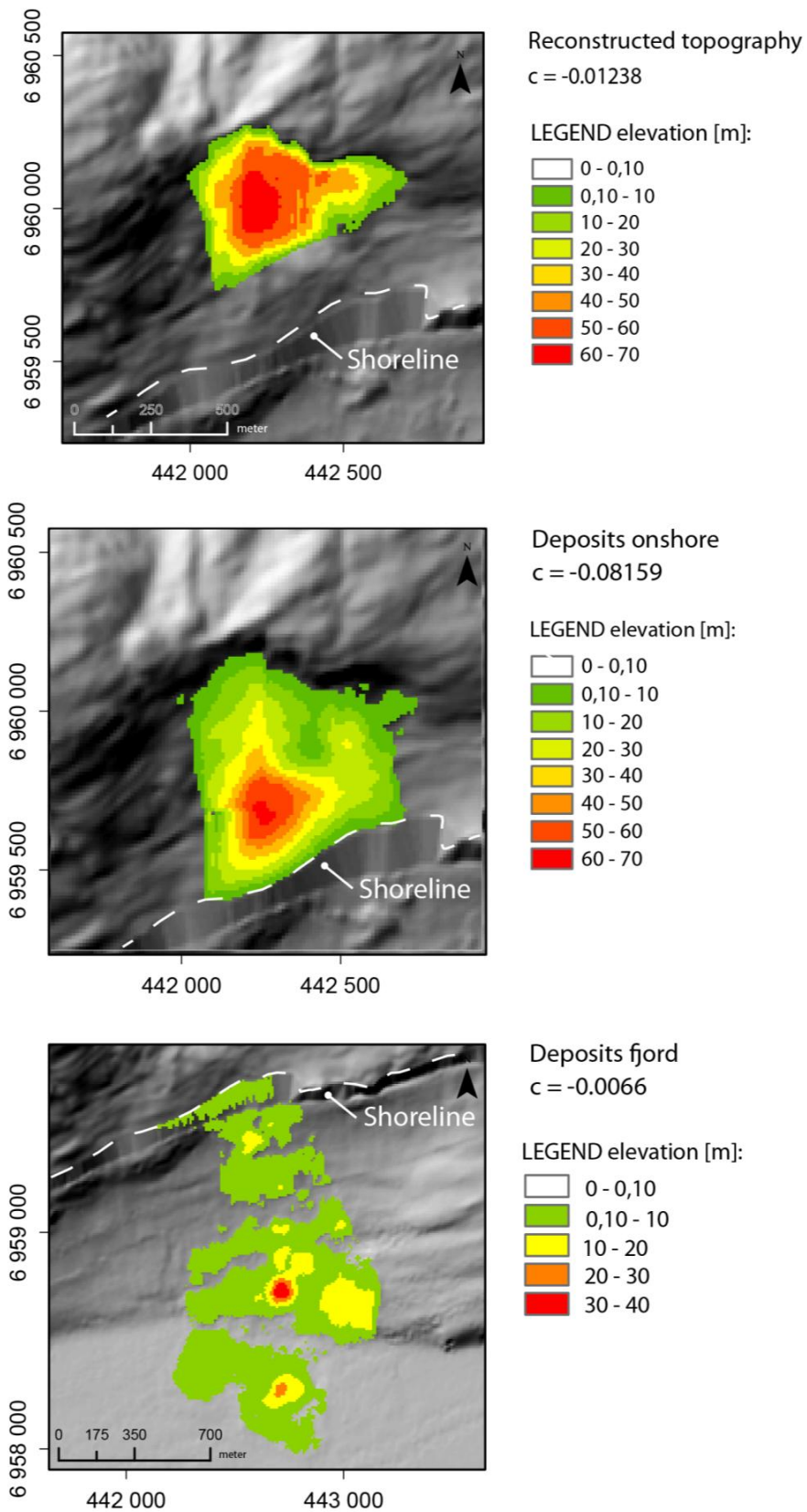
**Figure 37: The resulting surfaces using the SLBL method in CONEFALL.
These curvatures are based on the total volume estimations.**
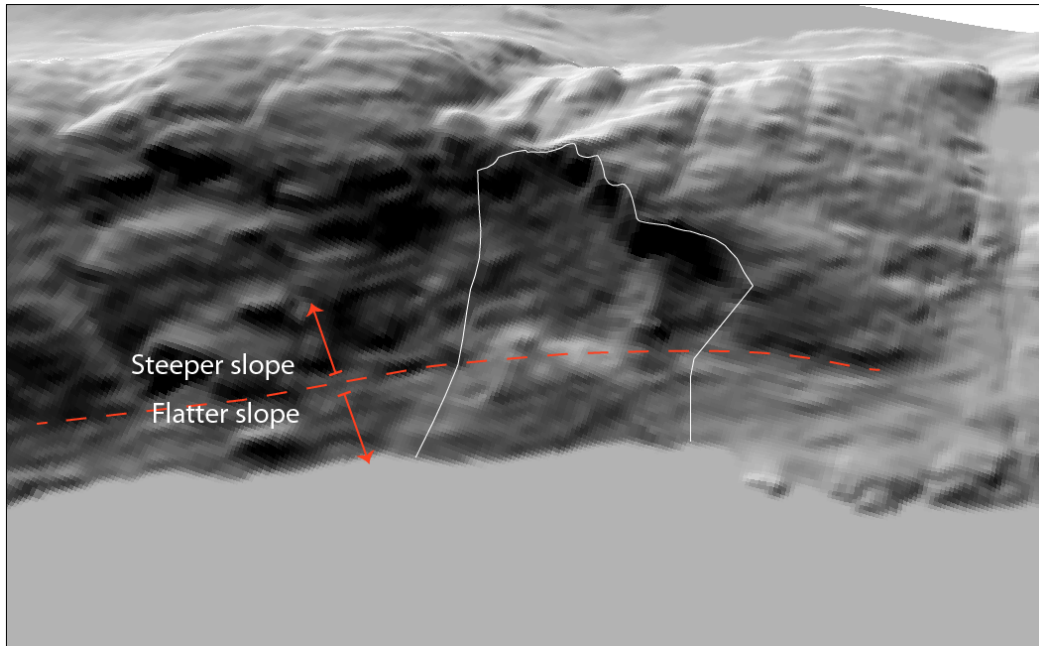
Figure 38: Present-day topography of the Tjellefonna area. Note the sharp morphological difference between steeper and flatter slopes trending parallel to Langfjorden.

6.1.2.   Reconstruction of pre-event topography using PolyWorks

The present topography of Tjellefonna is given in Figure 38. The morphology of the area can be divided into two topographic zones: a steeper upper part and a flatter part near the fjord. The manual reconstructed ante-rockslide topography (ART) from PolyWorks is based on this interpretation, as shown in Figure 39. The ART has similar slope face as the surrounding mountains, and consist of a mean slope angle of around 30°.

6.1.3.   Comparison of ART from SLBL and PolyWorks

Figure 40 gives a comparison of the SLBL and PolyWorks ART results (from profiles 1 to 3). In this figure the reconstructed ART from SLBL, the PolyWorks ART and a possible sliding surface from SLBL are compared. Both the reconstructed profiles from SLBL and PolyWorks seem to correlate well. Profile 1 stands out with a thinner overburden above the interpreted basal surface (blue line), which also corresponds to the field observations from Sandøy (2011b). Figure 41 shows the results from the SLBL cross-sections (Profile 4 to 6).
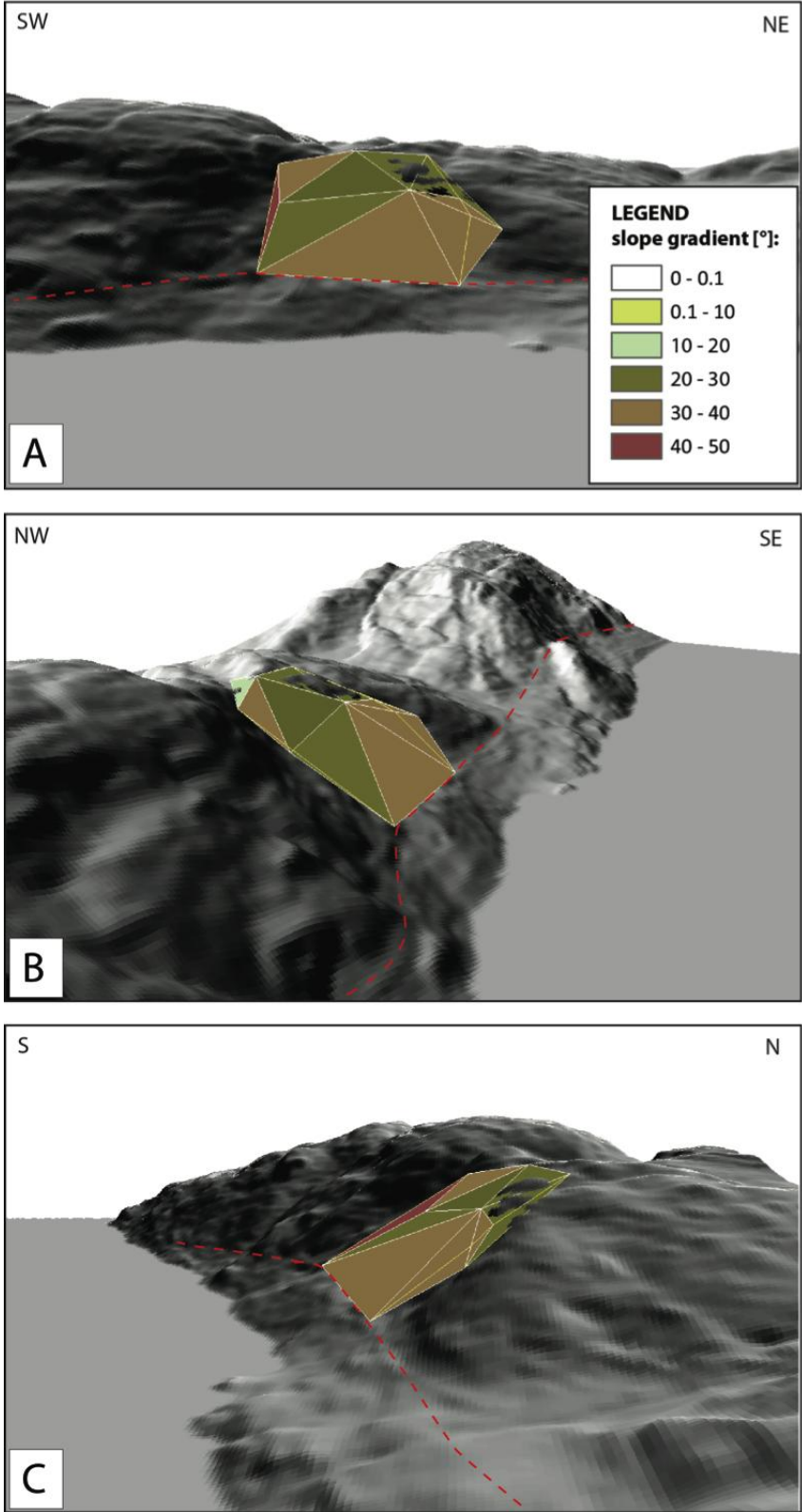
Figure 39: The reconstructed ART (PolyWorks) of Tjellefonna before the 1756 failure. The manual reconstruction is based on the surrounding mountainsides and fieldwork results.

PROFILE 1

PROFILE 2

PROFILE 3
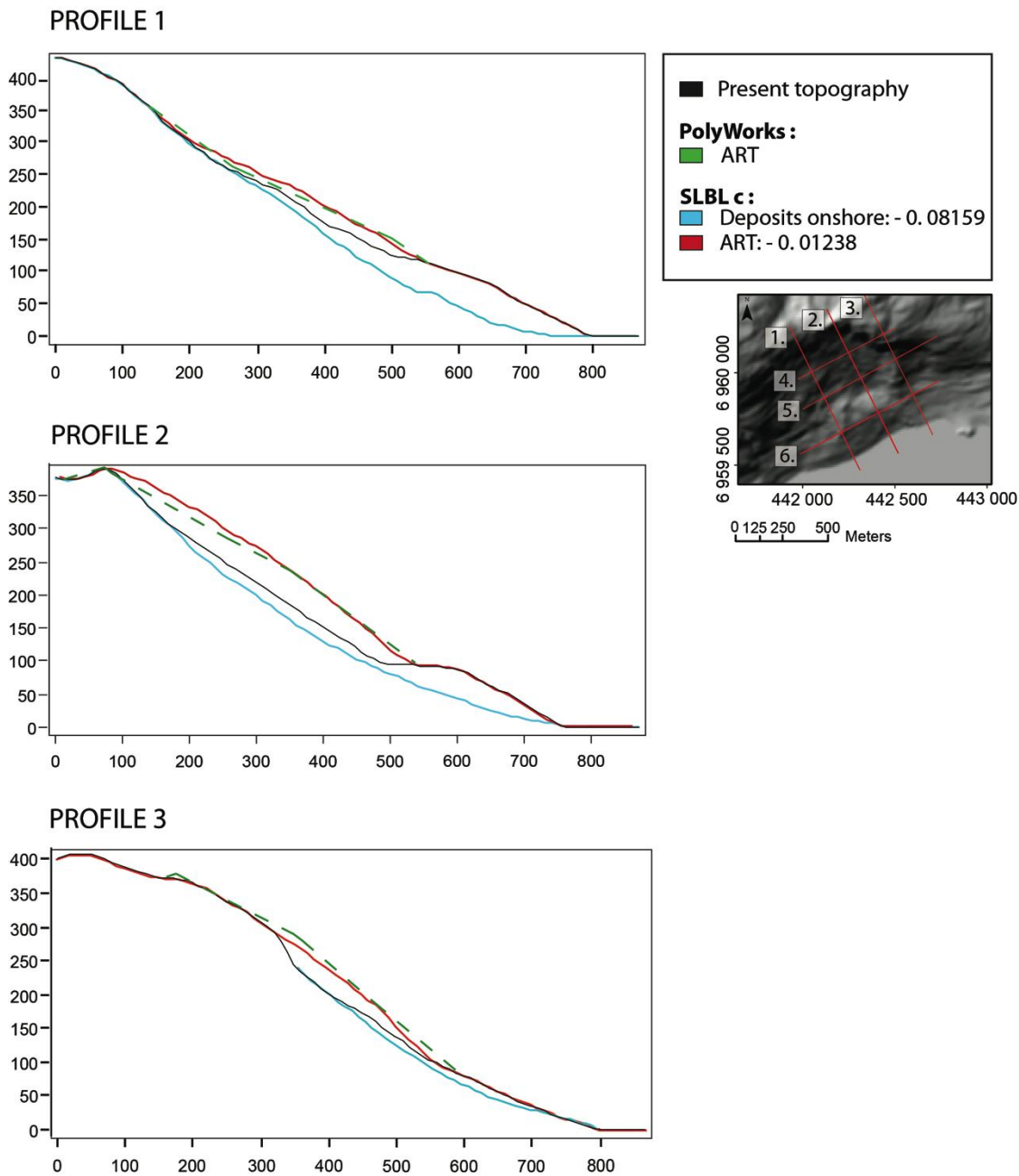
Figure 40: An overview of the SLBL and PolyWorks results. The SLBL red line represents the reconstructed topography and SLBL blue line the possible gliding surface. Results from PolyWorks ART are drawn as green dashed lines. Note that the SLBL and PolyWorks results correlate well.
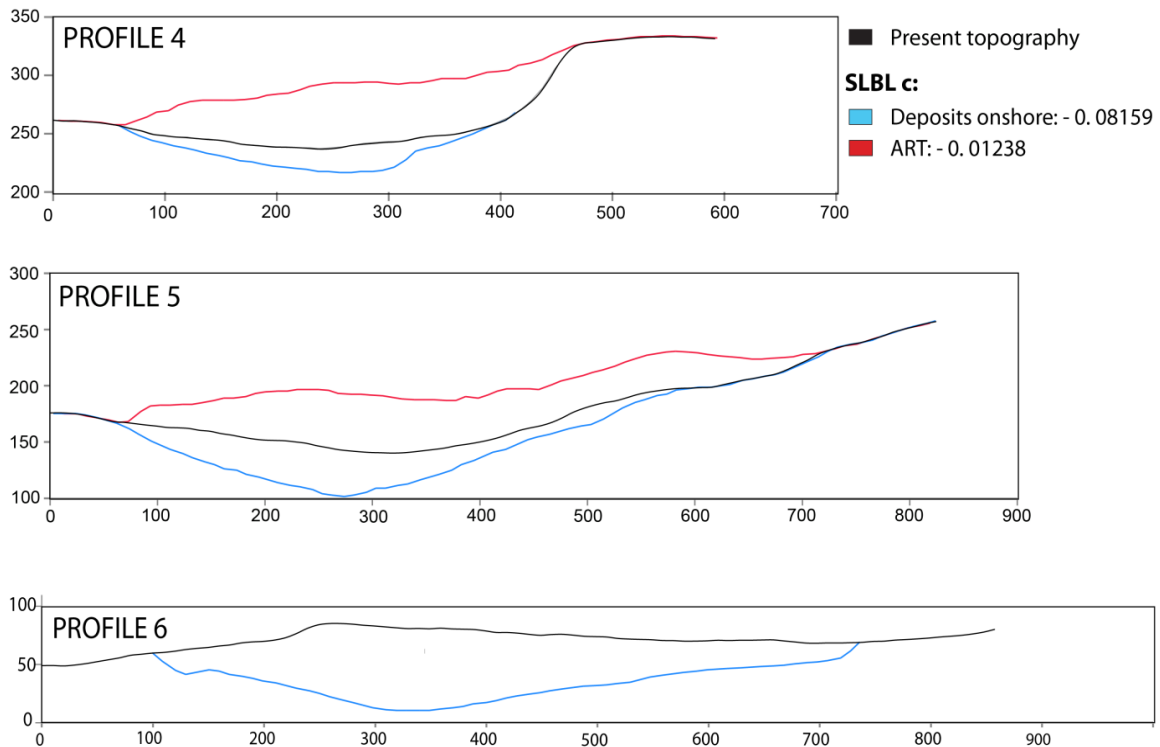
Figure 41: The SLBL results of profile 4 to 6 trending parallel to the back walls and Langfjorden.

6.1.4. Volume results

The final step of the SLBL analysis is to calculate the rockslide volumes. It is calculated that the volume of rock mass that failed is about 9.3 million m^3 (Table 19). It is also estimated that the deposits both onshore and in the fjord makes up a volume of about 11.5 million m^3, which is a volume increase of 24%. This fits well with the 25 % volume increase postulated by Hungr and Evans (2004). The calculations can be found in Appendix 5.

The volume is also estimated using PolyWorks ART in order to compare with the SLBL results, as shown in Table 20. This manual construction estimates the total volume of failed rock mass to be about 10.4 million m^3.

Based on these two methods the volume of failed material during the Tjellefonna slide is estimated to be in the order of 9 to 10 million m^3. Notice that the mean total height between the computed ART and the basal surface (Deposits ART) is estimated to be around 50 meters.

Table 19: The final results of the volume estimations based on SLBL. Figure 27 illustrates the polygons used to estimate the total volume of Tjellefonna.

Polygon:	c :	Max h [m]:	Mean h [m]	Volume [m3]:	Volume tot. [m3]:
ART	-0.01238	61	27	6 066 000	9 248 800
Deposits ART	-0.08159	69	23	3 182 800	
Onshore deposits	-0.08159	69	23	7 562 000	11 485 800
Deposits fjord	-0.0066	37	4	3 923 800	*24% increase

Table 20: Volume estimations based on the results from PolyWorks combined with SLBL deposits ART volume.

Polygon:	c :	Volume [m3]:	Volume tot. [m3]:
PolyWorks model	N/A	7 232 150	10 414 950
Deposits ART	-0.08159	3 182 800	

6.2.   Phase^2 results

6.2.1.   The in-situ stress state

Figure 42 shows the total long-term displacement (as creep) of the slope face, due to the deglaciation and stress release. The modelled highest displacement is below the present sea level (y = - 50 meters). Tension cracks observed at the back-scarp crown may be influenced of such creep. This effect is taken into account in the final setup, as the modelling consists of two stages; first created as a "box" to represent the pre-erosion situation, and secondly excavated to the pre-1756 topography. See chapter 5.3.1 for details.

Figure 43 illustrate the basal surface interpretation based on the strength factors at in-situ state, as recommended from Böhme (2012). This first approximation of the basal surface is conducted by using the post-analysis feature: "Ubiquitous joints", where J1 and J5 strength parameters are included in the Phase[2] interpretation modus. As shown, this proposed basal surface lies above the present-day topography and appears not to be a useful tool in this case.
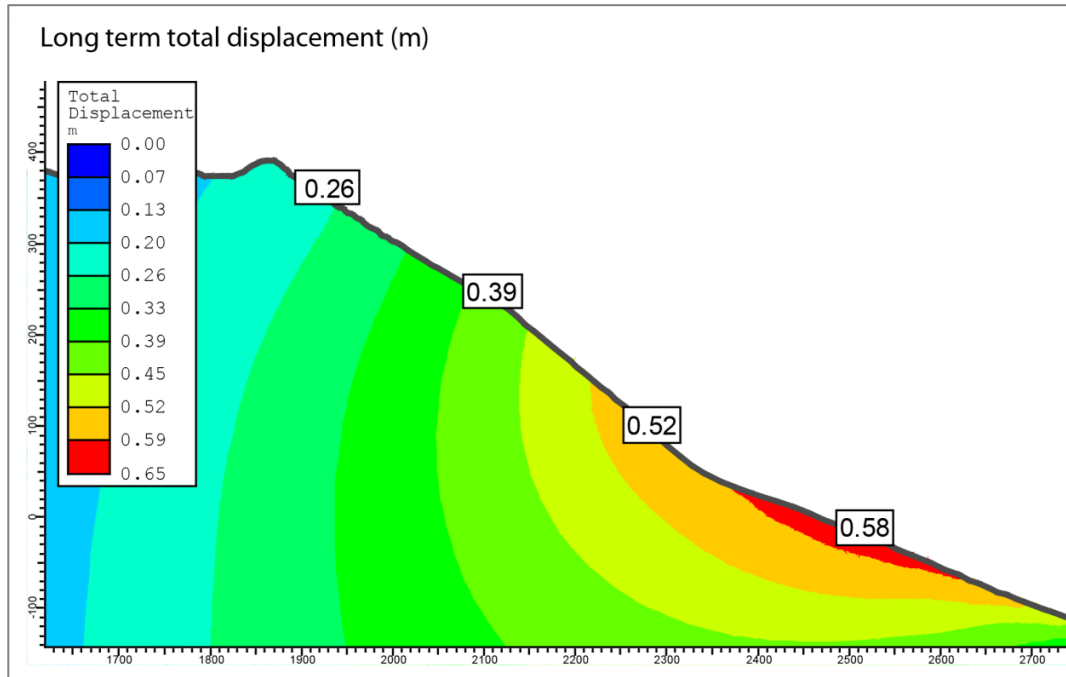
Figure 42: An overview of the long-term historical displacement as a consequence of glacial erosion.
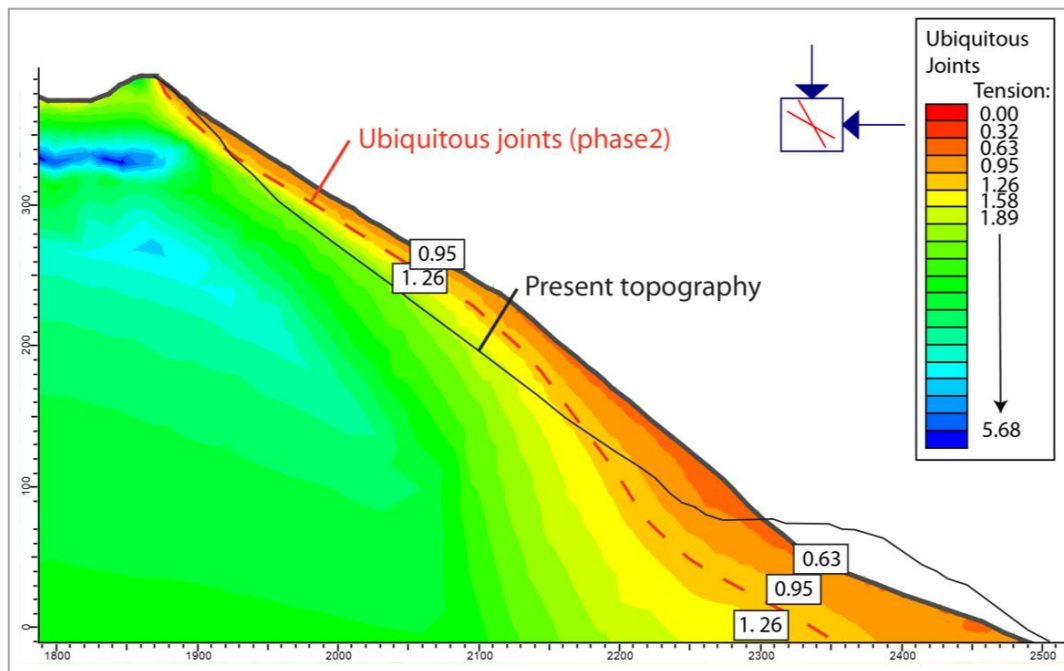
Figure 43: Interpretation of strength factors at in-situ stress state, where "Ubiquitous joints" feature are used. Discontinuities (J1, J5) are included manually into the model in the interpretation modus.

6.2.2.   Elastic – perfectly plastic (EPP)

SSR results

Analysis 1 is conducted as an elastic-perfectly plastic (EPP) setup with residual values equal to peak values for the rock mass and the discontinuities (See chapter 5.3.2: Elastic and plastic materials for more details).

In Analysis 1.1 the impact of faults and fault width on slope stability is tested (Figure 44). As can be seen in Figure 44 the stability decreases only very slightly by adding the faults (see reference stage, grey cross). It also shows that the width of the faults does not affect the outcome of the modelling significantly. The relative influence on the slope stability of the faults compared to the other discontinuities is also tested. As can be seen in Figure 44 the influence of J1 and J5 (red circles) is considerably larger than the faults. A curious outcome arises, however, when combining the faults and the joint sets (Model 2). The calculated SRF for Model 2 is actually higher than when the faults are not included (J1, J5). This is further discussed in chapter: 7.2.3. Also of interest is the impact of Model 2 compared to Model 1. As seen, the SRF decreases considerably when including J5. It is found from this analysis that the largest impact on the stability is the shallow-dipping discontinuity J5 in Model 2.
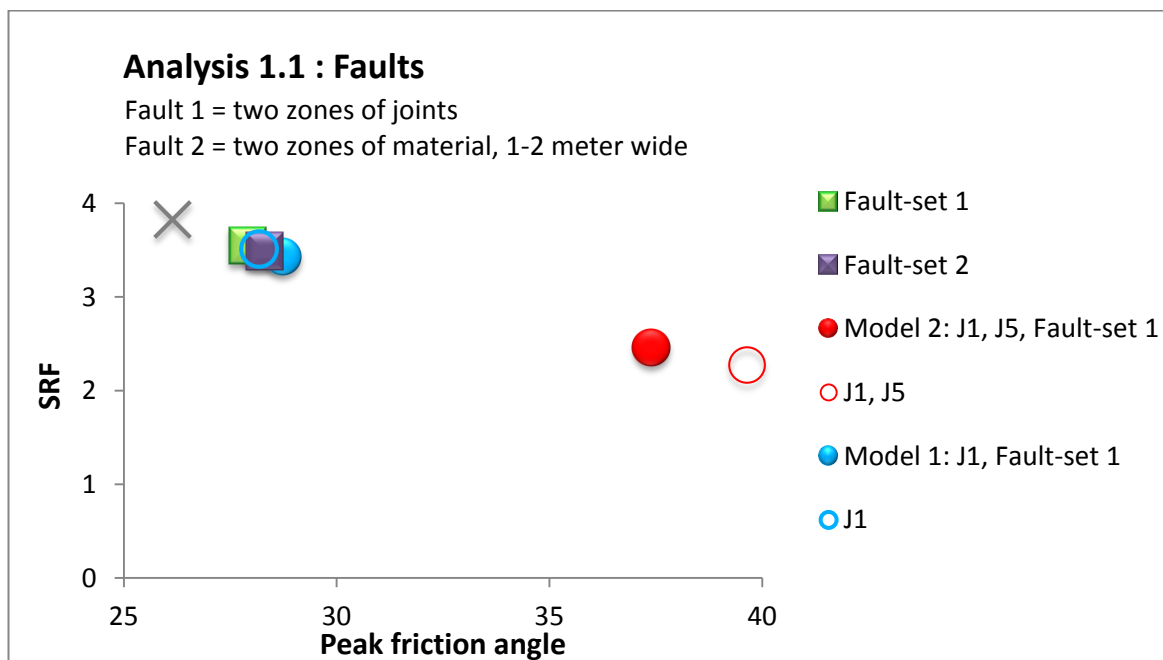
Figure 44: An overview of the impact of faults on the critical SRF. The models are tested with Fault-set 1 (modelled as two joints) and Fault-set 2 (two material zones with wide 1-2 meters).

The assessment of groundwater and earthquake as possible trigger factors are evaluated in Analysis 1.2 and summarized in Figure 45. As also shown in Figure 44, the Model 2 setup (red points) consequently gives lower critical SRF then Model 1 (blue points) and the reference stage (no joints, grey cross). It is found in Figure 45 that groundwater is a very important factor regarding the stability. However, in order for the model to fail a shallow-dipping structure is required. Still, Figure 45 shows that groundwater has a higher influence on reducing the SRF compared to J5 alone (e.g. see Model 2 [red circle] compared to Model 1 with high groundwater [blue unfilled triangle]). Additionally, an earthquake load of magnitude 2.7 (diamante shape) decreases the stability only slightly compared to the influence of groundwater. Note that failure only occurs in Model 2 when applying an earthquake with magnitude 8.25 (k = 0.15). This is discussed later.
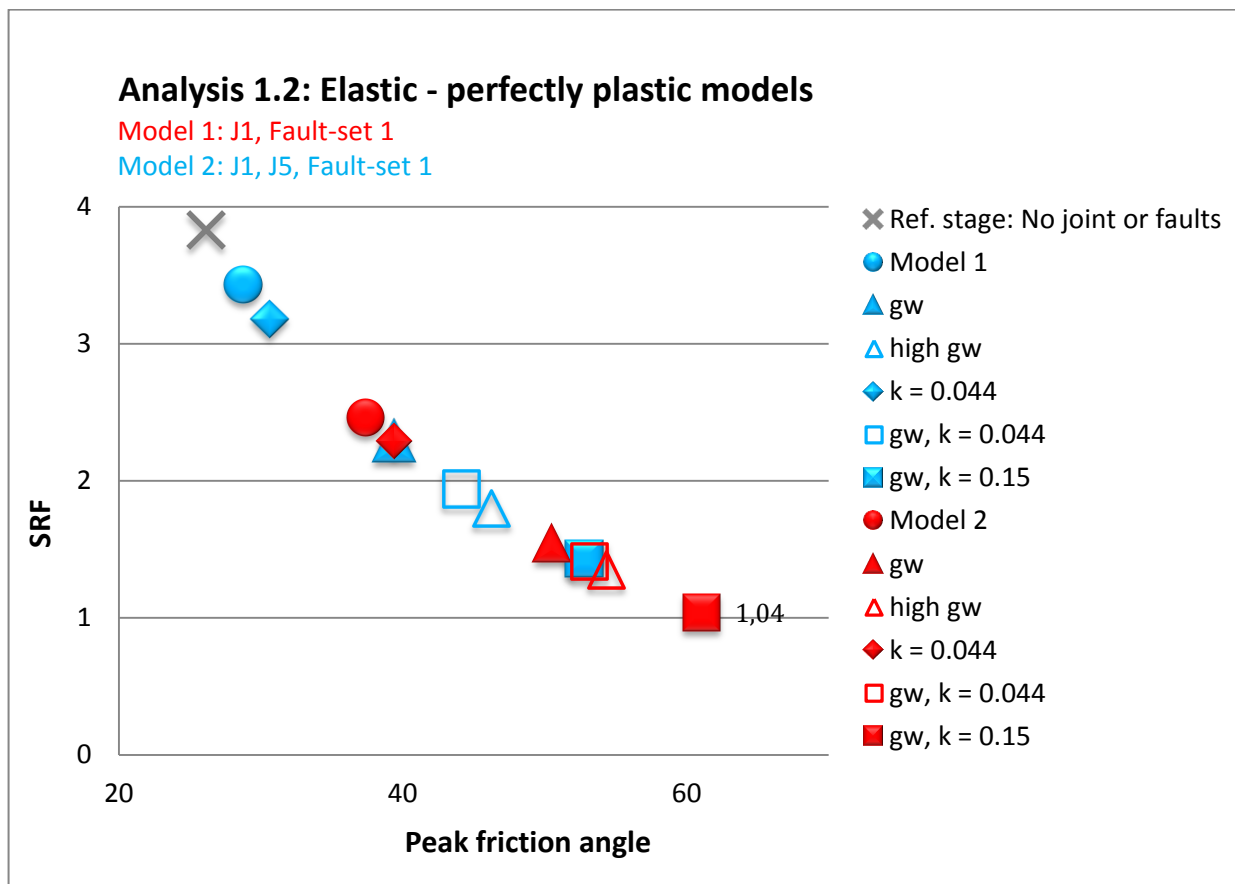
Figure 45: Analysis results of elastic-perfectly plastic model 1 (blue colour: J1, Fault-set 1) and model 2 (red colour: J1, J5, Fault-set 1).

The maximum shear strain interpretations in Analysis 1.2 can be found in Figure 46. A well developed shear strain surface is visible when running the model with no joints (Figure 46A). Yet, the shear surface continues behind the present-day crown and back walls. Figure 46B-C also illustrate that similar shear strain zones as in Figure 46A are seen when adding Fault-set 1 (Figure 46B) and joint set J1 (Figure 46C). However, it seems like that the shear zone developed in between the fault zones have a lower angle compared to the situation in the model without joints (Figure 46A). Furthermore, the shear zones daylight the topography in all 3 models at an attitude of ca. 70 m.a.s.l., which matches the SLBL model (Figure 46B-C, white line). In these settings (Figure 46B-C) the zone of shear strain terminates at the innermost fault. Note that these figures are not showing the situation at the critical SRF, but at a later stage as the surface is highlighted better at higher stages (Rocscience, 2011).

The shear strain results from Model 2 are of less interest, as no visible shear strain is shown. This is because failure in Model 2 takes place only along the discontinuities.
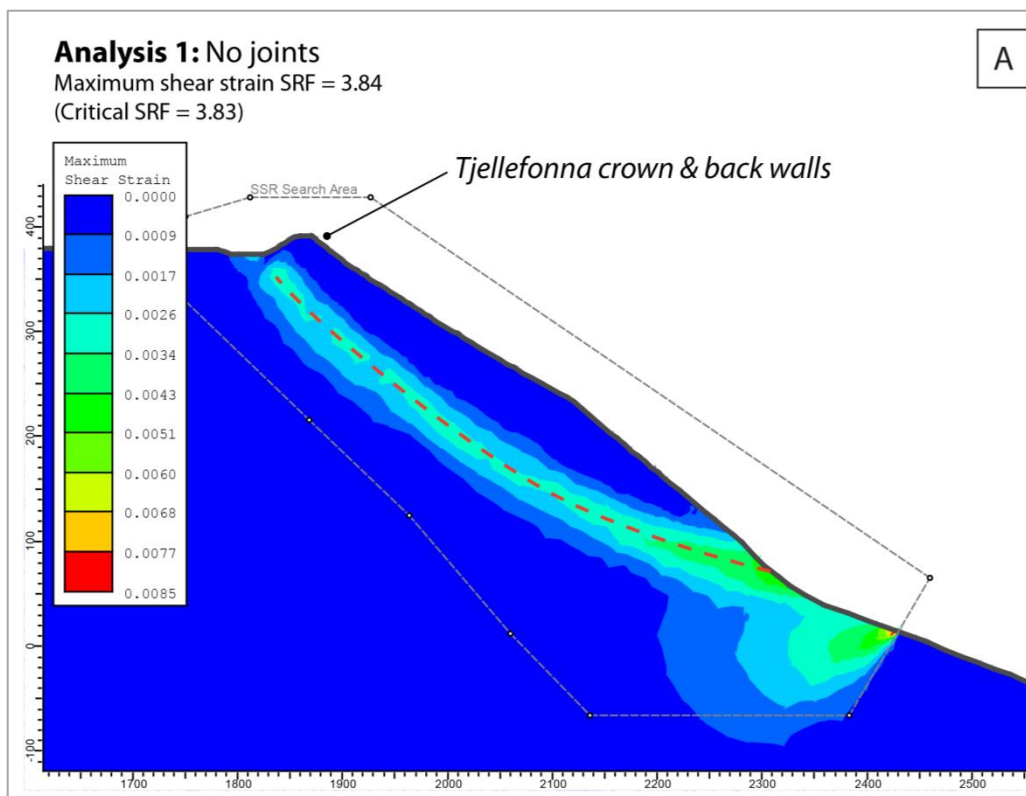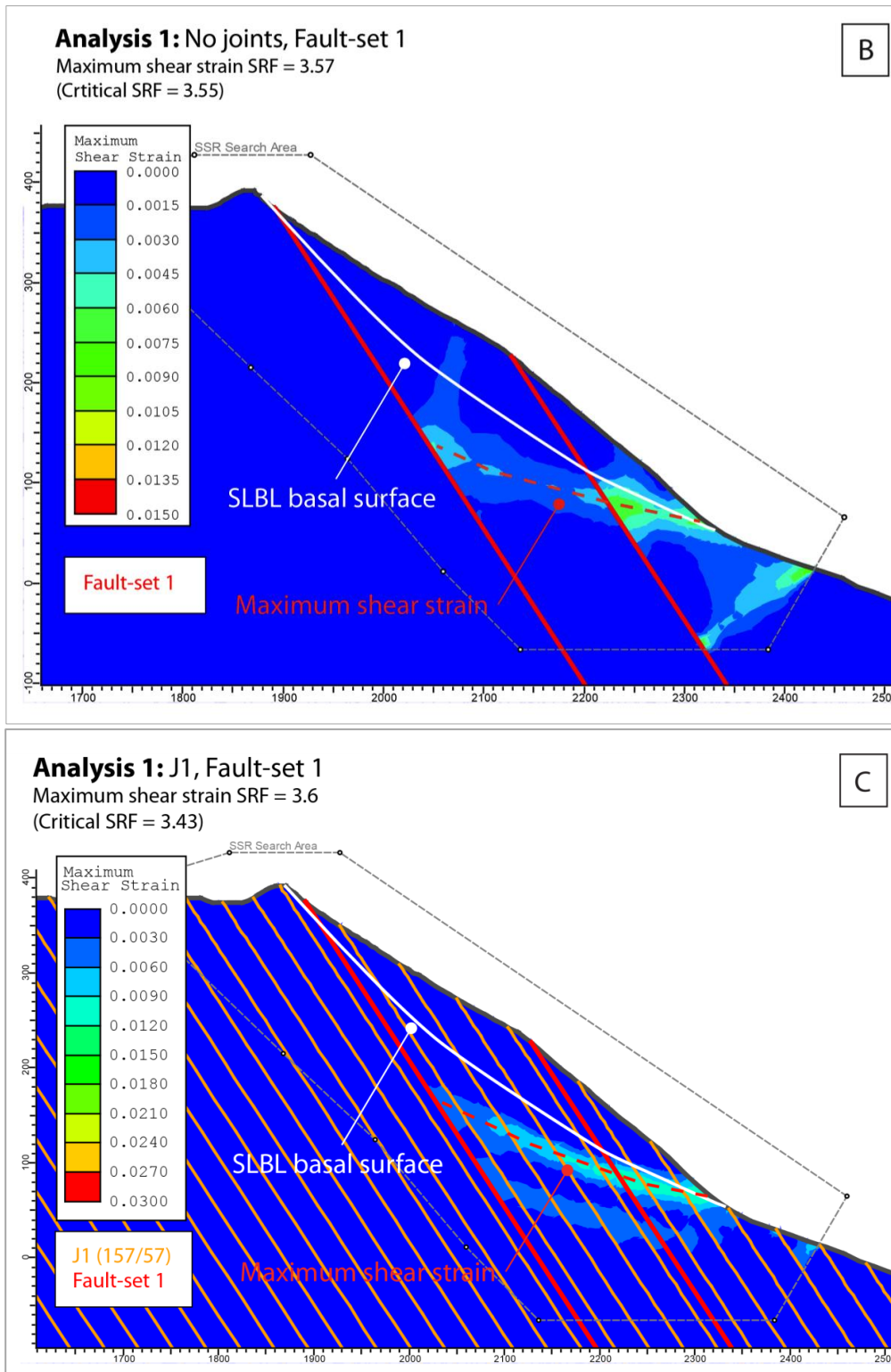
Figure 46: The interpretation of maximum shear strain shown as red dashed line. The white lines in B to C represent SLBL basal surface. A) Model set up without joints. B) Model with Fault-set 1. Shear strain are only developed between the faults. C) Shear strain development of Model 1, which consists of similar shear strain surface as the set up with only Fault-set 1.

The Fault-set 1 has also been studied in the view of total displacement (Figure 47). Figure 47 illustrates that the displacement corresponds to the maximum shear strain surface from Figure 46B, drawn as a red dashed line. The slope displacement is in this case highest between the two fault zones (Fault-set 1), and also above the toe zone where the sliding surface daylights. Note that there is no significant movement behind the faults.
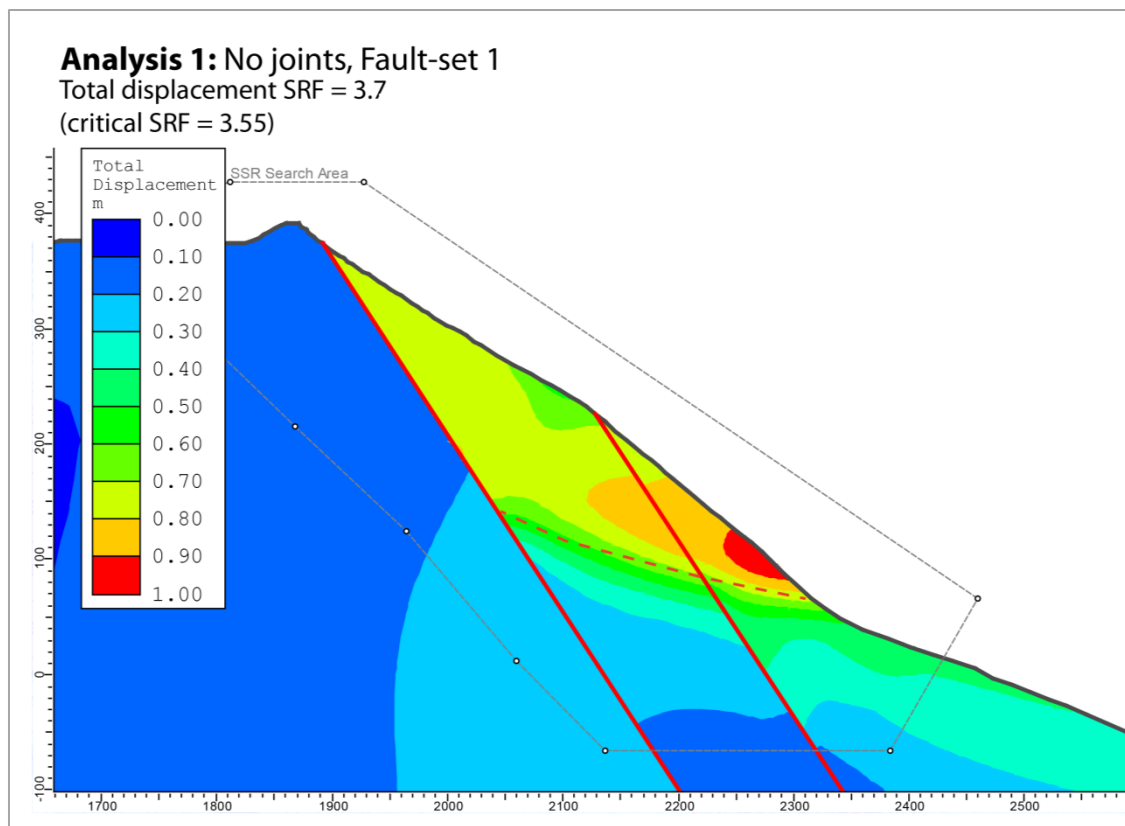
Figure 47: An illustration of displacement interpretation of a setup with Fault-set 1. The shown displacement fits the interpreted shear strain surface from Figure 46B (red dashed line).

6.2.3.   Elastic plastic, stain softening analyses

The strain softening analyses, referred to as Analysis 2 and Analysis 3, include a parameter study of the rock mass and discontinuities residual friction angle (φ_{res}) and cohesion (c_{res}). In Analysis 3 a seismic load (magnitude 2.7) is added in addition to the parameters in Analysis 2 (see 5.3.7 for more details). The historical data from the Tjellefonna rockslide testifies that the failure took place during a period of heavy rain. The large influence of groundwater on the stability is also proven in the previous analysis. Because of this all the strain-softening analyses include either "normal" or a high groundwater table, and are therefore different from Analysis 1.2.

Analysis 2: k = 0

As shown in Figure 48 failure occurs with a 30 % reduction of the residual values in Model 2. It is interesting that Model 1, regardless of the reduction in residual values (even with 50 %), remains stable. This further supports that a sub-horizontal structure (here as shallow-dipping J5) has an important impact on the SRF. Figure 48 also summarizes the relative impact of normal vs. high groundwater. As would be expected high groundwater leads to an additional reduction of the SRF. In Figure 48 it is illustrated that even with high groundwater a 50 % reduction of residual values will not lead to failure as long as there is no shallow-dipping structures present (see Model 1). It is also shown that strain softening is required to model slope failure, as all results without reduced residual strengths are stable (Figure 45).
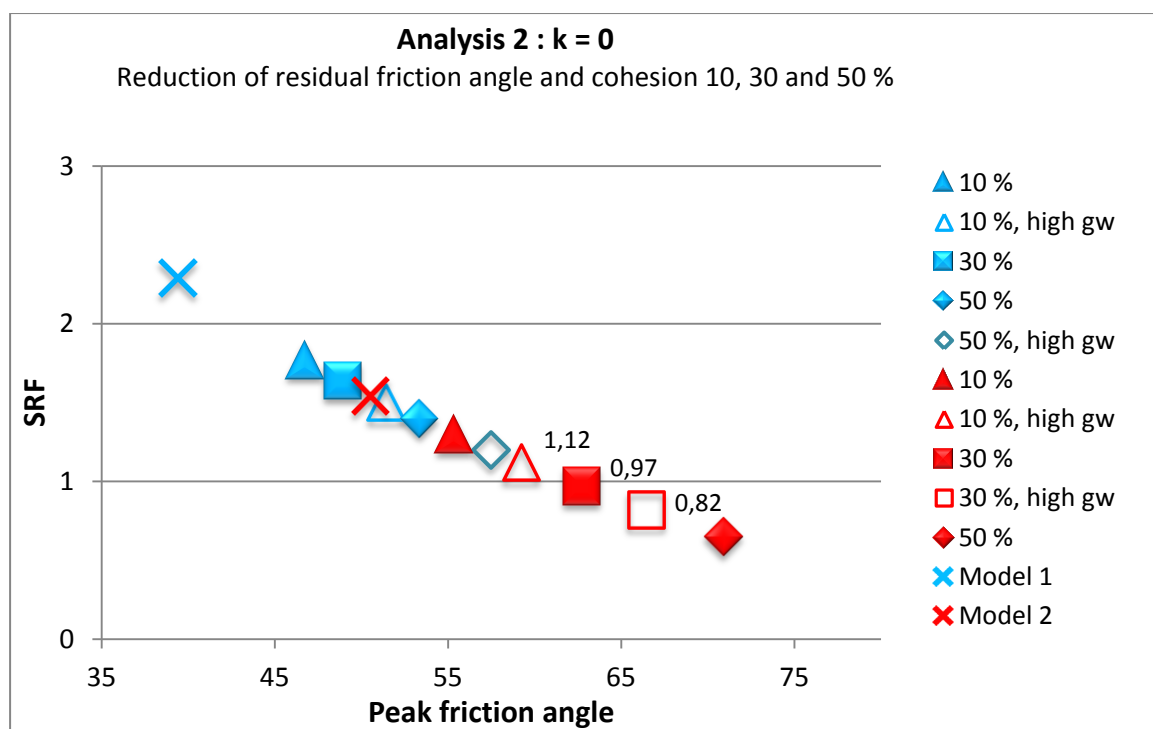
Figure 48: Results of strain softening model without earthquake (k = 0). Model 1 (J1, Fault-set 1, groundwater) in blue points, and Model 2 (J1, J5, Fault-set 1, groundwater) in red points.

Figure 49 Illustrates the total displacement of Model 2 with 30 % reduction of residual values (SRF = 0.97). The highest displacement arises nearest the slope face, with a total displacement of around 0.6 meters. Compared to Figure 47, this result gives no clear borders of the displacement zone. Still,

it looks like the displacement continues also between the fault zones, and to a large extent follows the top of J5.
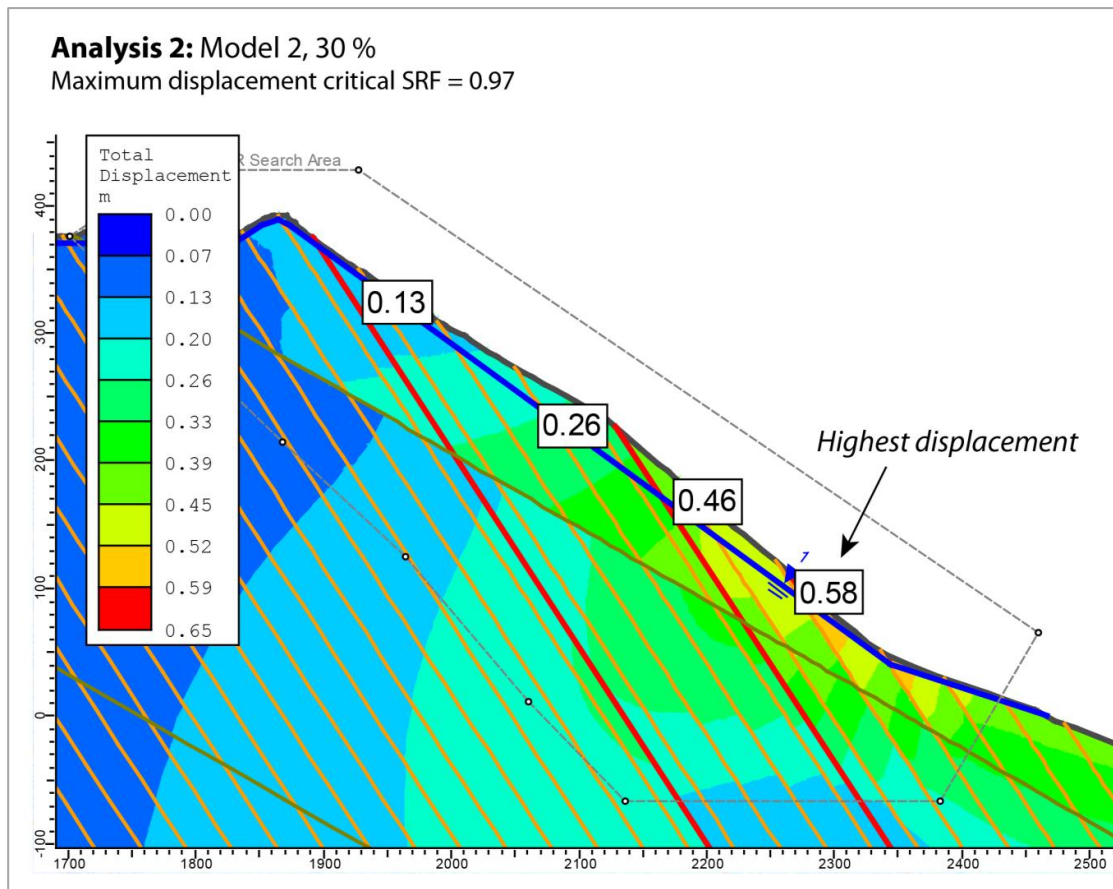
Figure 49: Illustration of total displacement at Model 2 consisting of 30 % strength reduction. This set up includes normal groundwater table.

Analysis 3: k = 0.044

In Analysis 3 a constant earthquake load of magnitude 2.7 is applied (Figure 50). This model setup leads to an additional decrease of the SRF, compared to Analysis 2 (Figure 48). In this case failure occurs at only 10 % reduction of residual values in Model 2, when combined with high groundwater (red triangle, unfilled). Figure 50 also shows that even when applying this seismic load Model 1 does not fail under any of the tested circumstances.
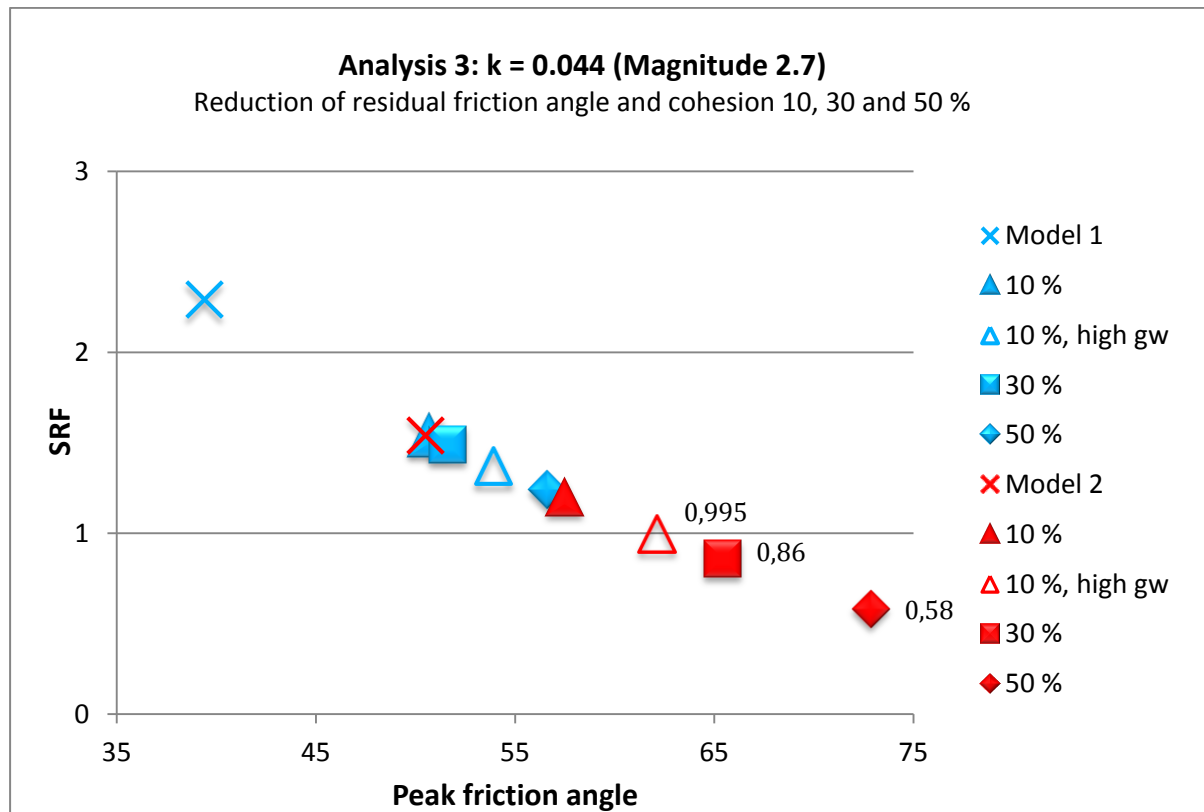
Figure 50: Results of the strain-softening models, with earthquake. Model 1 (blue) consist of: J1, Fault-set 1 and groundwater, and Model 2 (red): J1, J5, Fault-set 1 and groundwater.

Figure 51 illustrates the total displacement of Model 2 in combination with high groundwater, a seismic load of k = 0.044 and a 10% reduction of the residual friction and cohesion values. The total displacement is barely higher than in Figure 49 (run without earthquake), which states that the total movement is only slightly influenced by adding an earthquake load. Similar to Figure 49, the displacement zone is not clearly defined. Still, the movement seems to follow J5 and Fault-set 1.
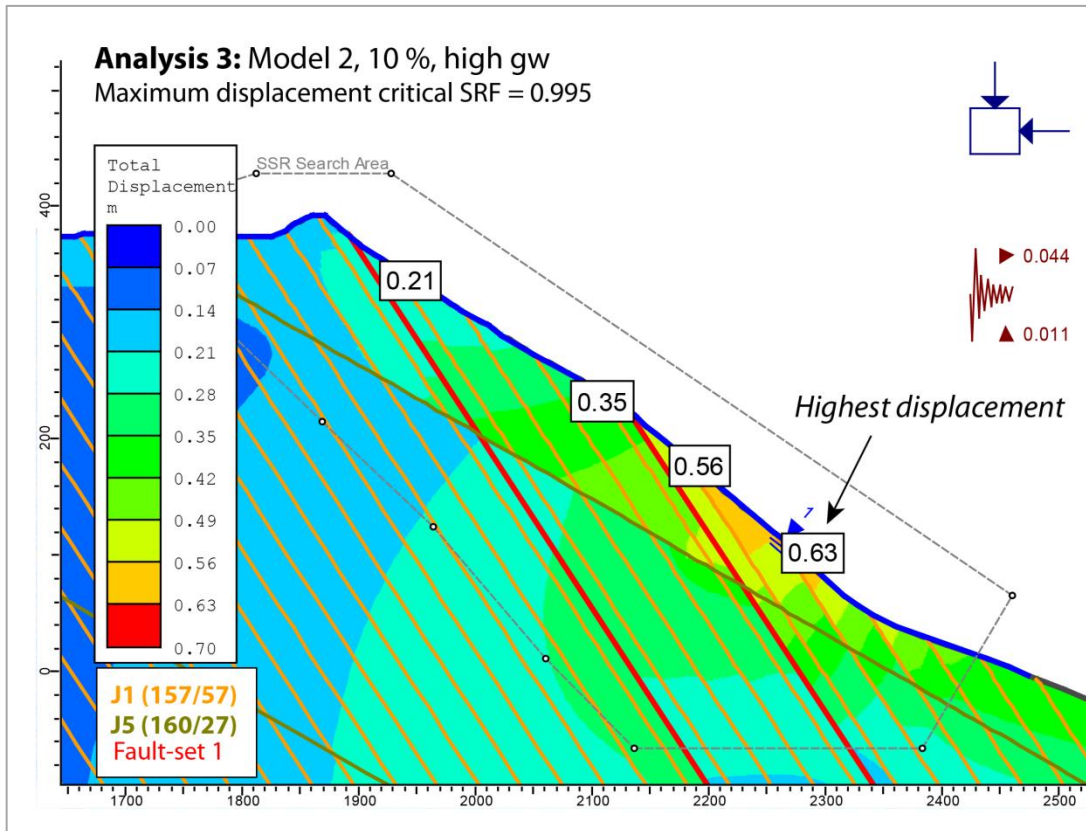
Figure 51: The Phase² interpretation of total displacement when critical SRF = 0.995 at Model 2 (10 % reduction). The model includes high groundwater table and earthquake magnitude of 2.7 (k = 0.044).

6.2.4. Analysis 4: The role of discontinuity set J5 on slope stability

Based on the results above, it is clear that a shallow-dipping structure (J5 in Model 2) seems to play a vital role in order for failure to occur. A more detailed study of the J5 parameters was therefore conducted (Analysis 4). In Analysis 4.1 the impact of friction angle and cohesion of this joint set is studied with Model 2 (set up: residual values equal peak, no groundwater present). The spacing has been investigated in Analysis 4.2 and Analysis 4.3. These analyses consist of Model 2 (spacing 300 meters) and Model 3 (spacing 30 meters). Apart from the spacing the Model 3 is equal to Model 2.

77

A study of chosen friction angle and cohesion

Figure 52 summarizes the results from Analysis 4.1, and illustrates that a reduction of friction angle more significantly reduces the SRF than a similar reduction of the cohesion. While a reduction in friction angle leads to a 26 to 40 % reduction in SRF, the cohesion decreases the safety factor only marginally (from 2.4 to 2.3). See Table 21 and Table 22 for results overview. However, a result of interest is that there is a very little change in SRF when changing the cohesion from c = 0.0632 to c = 0. This clearly states that the Phase^2 SRF results are not comparable to the real-life situation, as c = 0 should give an even lower SRF.
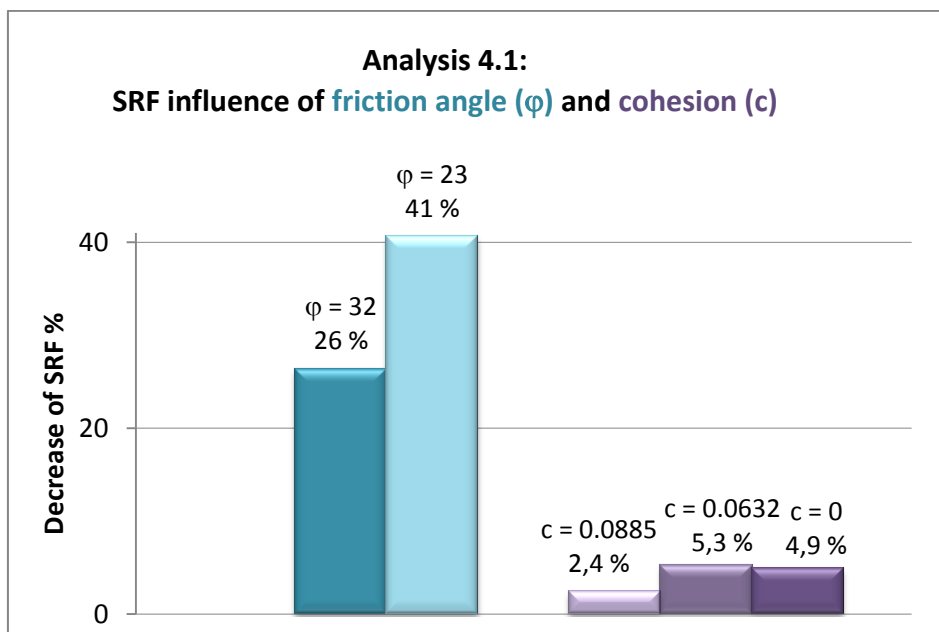
Figure 52: The results of "Analysis 4.1", which shows that the largest impact of decreasing SRF is clearly the friction angle. See Table 21 and Table 22 for more details.

Table 21: Input parameters in "Analysis 4.1". Note that the cohesion is constant during the modelling at c = 0.127.

Friction angle:	Reduction:	SRF:
45	0 %	2,46
32	30 %	1,81
23	50 %	1,46

Table 22: Input parameters in "Analysis 4.1". Note that the friction angle is constant during the modelling at φ = 45°.

Cohesion:	Reduction:	SRF
0.127	0 %	2,46
0.0885	30 %	2,4
0.0632	50 %	2,33
0	100 %	2,34

The Influence of J5 spacing

Figure 53 gives an overview of the results from Analysis 4.2, where the relationship between spacing and different friction angles is illustrated. The figure shows that the friction angle has a larger impact on the reduction of the SRF than the spacing of J5. Still, the spacing seems to have an increasing impact on the SRF as the friction angle is reduced. However, the results show that no failure occurs without including trigger factors such as groundwater and earthquake.
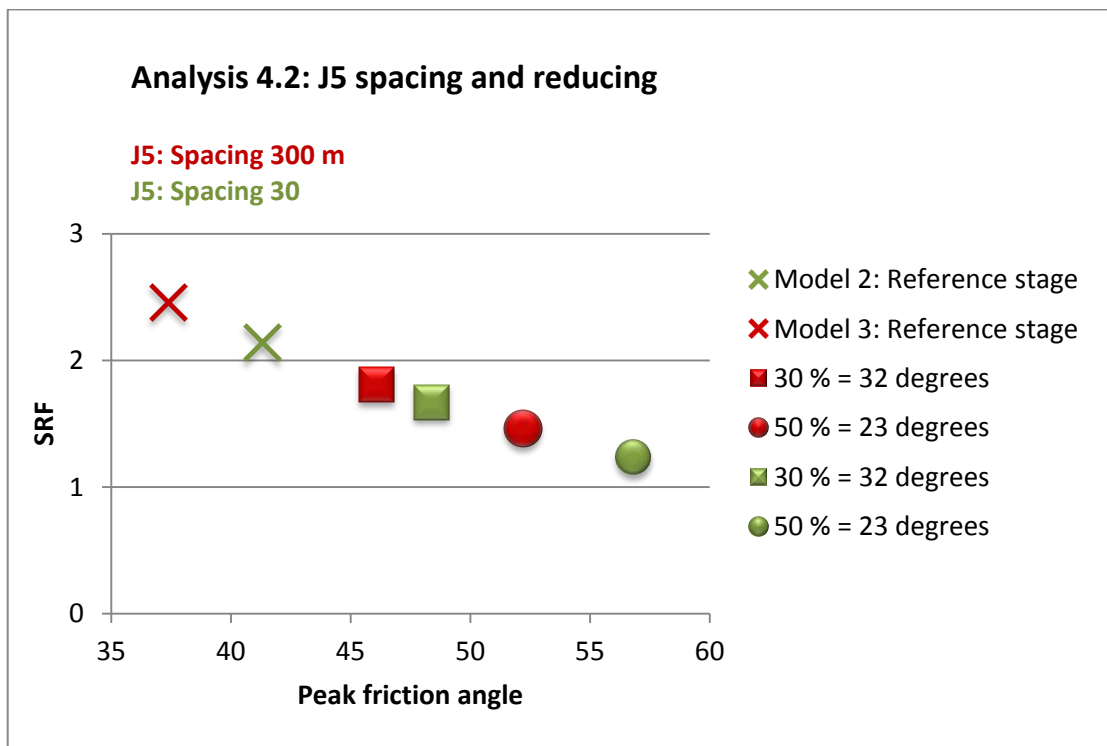
Figure 53: Overview of the impact on SRF of different spacing (Model 2 in red: 300 meters, Model 3 in green: 30 meters) and friction angles. Only J5 friction angle was changed from the reference stage (φ = 45°) to 30 % (φ = 32°) and 50 % (φ = 23°) reduction.

Likewise, the stability impact of decreased spacing and reduced friction angles are evaluated together with trigger factors (groundwater and earthquake) in Analysis 4.3 (Figure 54). Figure 54 shows that failure only occurs in both Model 2 and Model 3 when including high groundwater and reducing the friction angles. When comparing these results to the outcomes in Figure 53, the major role of groundwater on the stability is clearly seen. The most important changes related to the spacing of J5 are listed in Table 23. This table shows that a 10 times decrease of J5 spacing (300 to 30 m) results in a reduction of SRF of about 11 %.

Additionally, Model 3 is very close to failure (SRF = 1.01) when using non-reduced friction angles, but only applying high groundwater table and earthquake. This output reveals that the discontinuities spacing could play an important role in combination with groundwater.
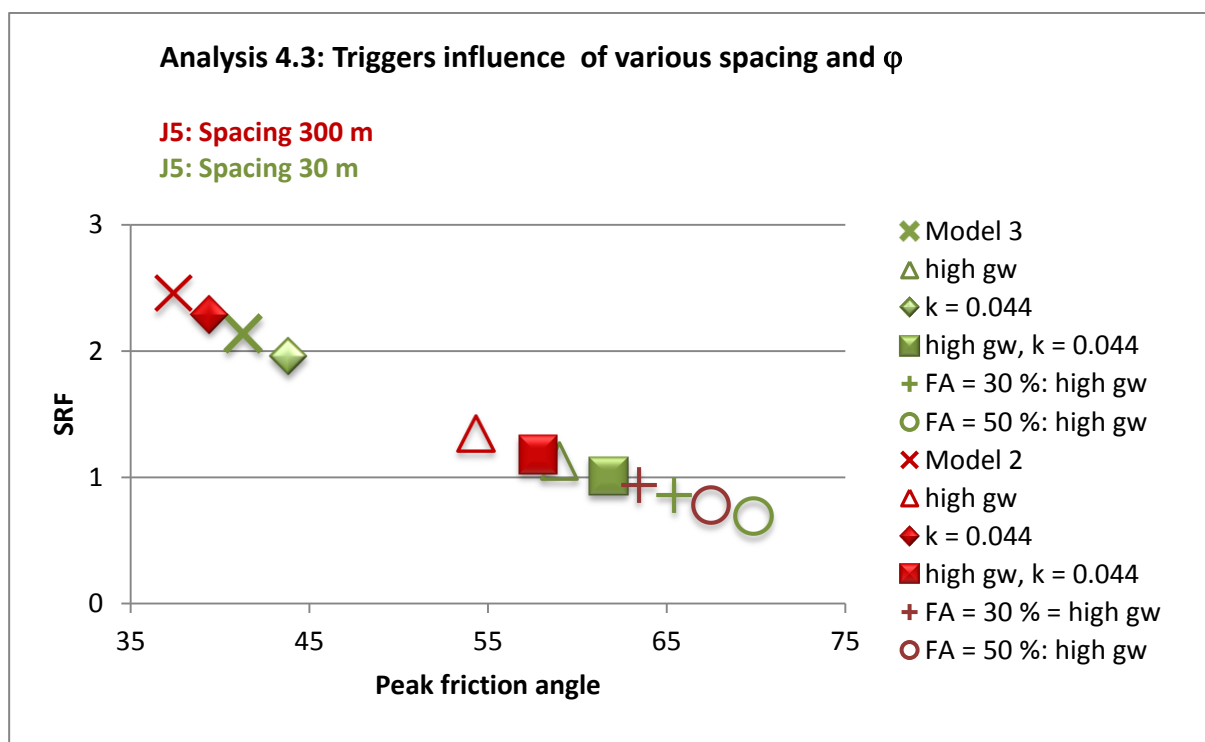
Figure 54: The role of the discontinuity set J5, including triggers like groundwater and earthquake. Model 3 represents a spacing of 30 meters (green plots) and Model 2 spacing of 300 meter (red plots). Both models have equal geological settings with J1, J5 and Fault-set 1.

Table 23: The results of interest in Analysis 4.3 are listed below. Note that Model 3 (spacing 30 meters) gives the lowest SRF. The total mean different between the SRFs is around 11 %.

Set up:	SRF: Model 2	SRF: Model 3	Difference of SRF %:
Reference stage (gw)	2,46	2,33	5 %
High gw	1,35	1,13	16 %
High gw, k = 0.044	1,18	1,01	14 %
FA = 30 %, high gw	0,94	0,86	9 %
FA = 50 %, high gw	0,78	0,69	11 %

6.2.5.   Analysis 5: Influence of sub-horizontal fault

Previous results reveal that the Tjellefonna stability is strongly depended on the presence of groundwater and a shallow-dipping structure, J5. However, the J5 discontinuity set is not as well developed in field as J5 is put in the Phase^2 model. On the other hand, a sub-horizontal fault (Fault-set 3) striking parallel to Langfjorden was observed at an outcrop SW of the lower rockslide limit (Figure 62; Chapter 7.3). Fault-set 3 is included into the set up of Model 1 and Model 2 (Table 24), where the rock mass and discontinuities are run with strain softening models of 10 % reduction. This will be discussed later.

Table 24: Results of SRF when including a sub-horizontal fault.

Model set up:		Triggers:	SRF: No Fault-set 3	SRF: Fault-set 3	Difference (%) :
Model 1 (10 %)	J1, Fault-set 1	-	2.8	1.64	41
		H - gw	1,5	**0.93**	38
Model 2 (10 %)	J1, J5, Fault-set 1	-	2.07	1.6	22
		H - gw	1,12	**0.86**	23

The results in Table 24 show that Model 1 and Model 2 are both unstable when Fault-set 3 and high groundwater is present. The results of Analysis 5 stand out from previous analyses, as Model 1 result in a SRF below 1. Furthermore, comparing the results of Fault-set 3 with a setup without this horizontal fault, the results reveals that Fault-set 3 has a higher influence on the stability than discontinuity set J5. This is seen as a reduction of the SRF of around 40 % in Model 1 and around 20 % in Model 2.

Figure 55 illustrates the total displacement of Model 1 and Model 2 when including Fault-set 3 and high groundwater table. The model has similar movement development as in previous analyses (Figure 49 and Figure 51), in which the displacement seems to be terminated between the faults. When compared to the previous results with strain softening (Analysis 2 and 3), this Model 2 (Figure 55B) has a larger displacement (maximum 1 meter) at the slope toe.
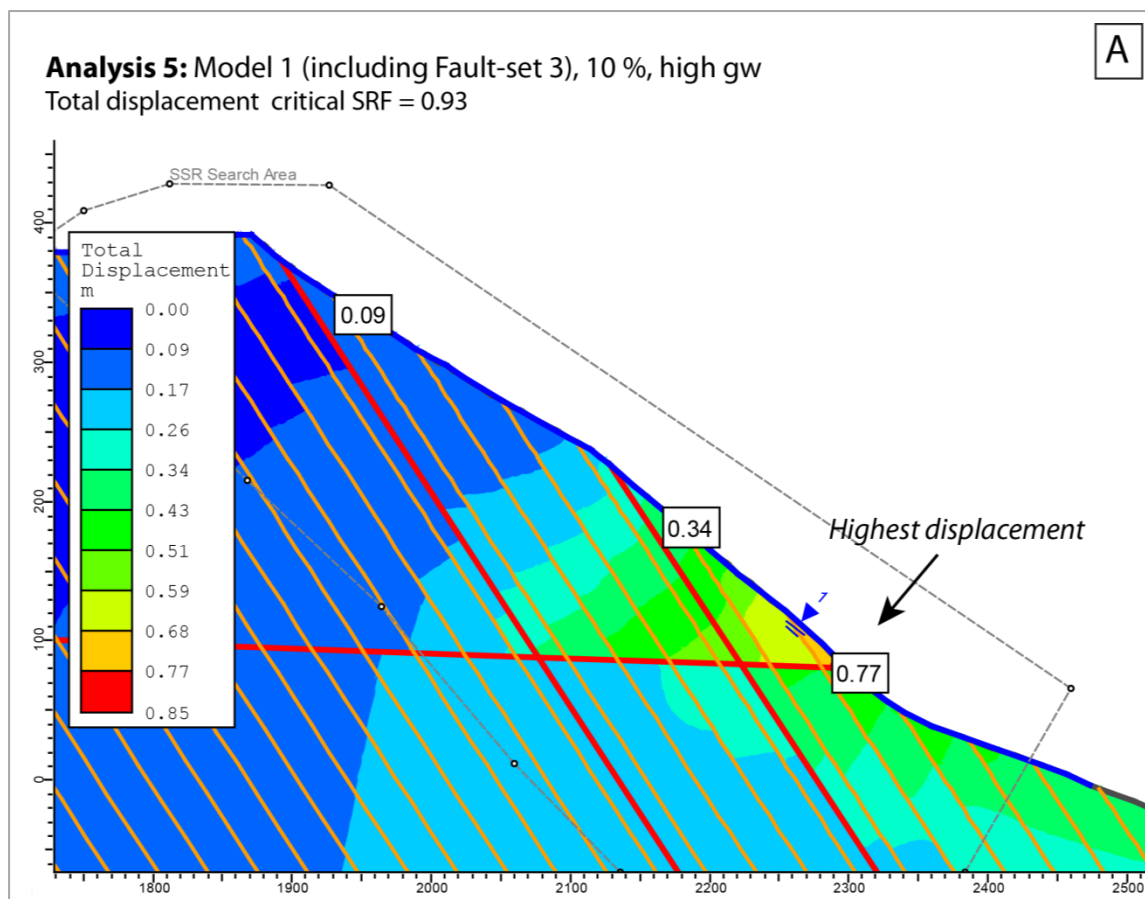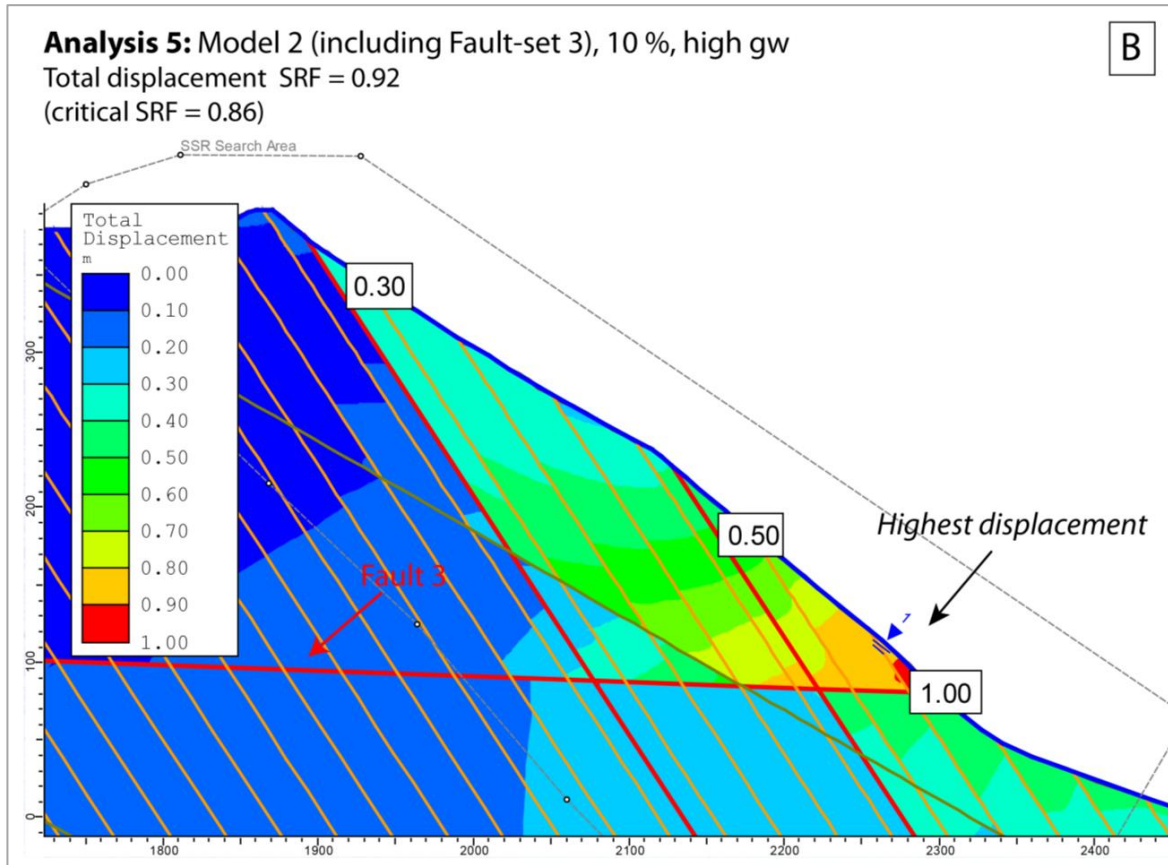
Figure 55: The total displacement of A) Model 1 and B) Model 2, including Fault-set 3 and high groundwater. As seen, the displacement is highest at Model 2 slope face toe.

7. Discussion

7.1. Reconstruction of ART and volume estimations

The chosen curvature values of the SLBL are based on the recommendation by Hungr and Evans (2004) that a 25 % volume expansion is expected because of fragmentation of the rock debris during failure. In this master thesis an increase of 24 % was found to represent the best-fitted solution (Appendix 5, Table 19; Chapter 6.1.4), as the curvature criteria for the onshore deposits was set to -0.08159 to fulfil the field observations (i.e. the deposit thickness observed in field). Yet, there is some uncertainties of this volume increase, as it is assumed that fragmentation produces a volume increase of around 25 % based on a typical range (18 % to 35 %) of measured porosities of loosely placed well-graded crushed rocks. Field estimates of this volume increase are difficult to carry out (require accurate measurement of both deposits and source volume).

Furthermore, the SLBL outputs from CONEFALL are used to evaluate the fit of the chosen curvature (Figure 37; Chapter 6.1.1). As mentioned, one aspect that is of interest is the curvature of the offshore part (curvature of -0.0066). Since the estimated surface does not cover the entire deposit area, but rather smaller zones with larger thicknesses, it may be somewhat underestimated. Nevertheless, this distribution could reflect the real situation and may have developed from either the flow mechanisms of the rockslide debris or through several pulses in the rock avalanche due to the successive failure of different compartments.

The computed ART from SLBL is compared to the manual reconstruction in PolyWorks in Figure 40 (Chapter 6.1.3). As the figure illustrates, both methods seem to correlate well. However, the methods require good geological understanding of a possible sliding surface, as well as of the failed topography. Additionally, as the reconstructions are conducted in several steps (e.g. SLBL based on 6 profiles on both land and fjord, PolyWorks Method 1 or Method 2), the techniques are time consuming and require access to a DEM with a suitable resolution.

The initial failed volume of Tjellefonna is recalculated to be around 9 to 10 million m^3, which is less than what were estimated by Jørstad (1965) and Bugge (1936) (12 million m^3 and 15 million m^3 respectively). The results presented here are based on reconstruction and interpretation of the basal failure surface from both SLBL (9.3 million m^3) and PolyWorks (10.4 million m^3). The fact that both methods result in very similar volumes indicates that the estimations are reliable.

This re-estimated volume has an important consequence for the tsunami modelling by NGI (Harbitz et al., 2011), as the new volume is about 5 million m³ less than used in their modelling. The Tjellefonna event was used to test the accuracy of the model, that aims at predicting wave heights and wave travel distances for new rockslide generated tsunamis. Since the new volume is much less than what was used in the NGI-model, the tsunami modelling is actually underestimating the consequences of future possible rockslide-generated tsunamis (e.g. Åknes).

7.2. Phase^2 results

7.2.1. The uncertainties of parameters

According to the standard, the rebound value R should be obtained from a dry unweathered joint surface, and r from a wet weathered joint surface. This was not entirely possible during the fieldwork as both surfaces were wet, which may cause less difference between the parameters. Also, the mapped parameters (JRC, JCS and rebound values) have some uncertainties as they are only based on a few data sets and localities from a one-day fieldwork (Appendix 1).

One of the most critical steps in the numerical modelling is the determination of the shear strength parameters (φ and c) for the rock mass and discontinuities. The numerical setup used in this master thesis consists of the instantaneous friction angle and cohesion (Appendix 2 and 3).

The instantaneous strength parameters (φ= 62 and c = 0.8 MPa) of the rock mass are based on fieldwork data, which are converted from Hoek-Brown criterion to equivalent instantaneous Mohr-Coulomb strength parameters in RocLab (See chapter 5.3.2). The normal stress (and following strength parameters) may not be exact, as the mean normal stress is based on an interpreted sliding surface (from SLBL profile 2, Figure 40; Chapter 6.1.3). Still, this method is concluded to be the best approach for the fractured rock mass at Tjellefonna (Nilsen, 2012). This theory is supported by using the same input values in RocLab, but without applying the instantaneous method, which in contrast gives an estimate of φ = 34° and c = 9 MPa (failure envelope range similar to instantaneous). When Figure 56 from Wyllie and Mah (2004) is taken into consideration a rock mass cohesion of 9 MPa is too high. This cohesion is more suitable for a weak rock type without joints, or relative strong rock mass without present of joints (Nilsen, 2012). Still, even as Tjellefonna shear parameters is outside the chart it is consider reasonable as Figure 56 only shows a range of literature value.
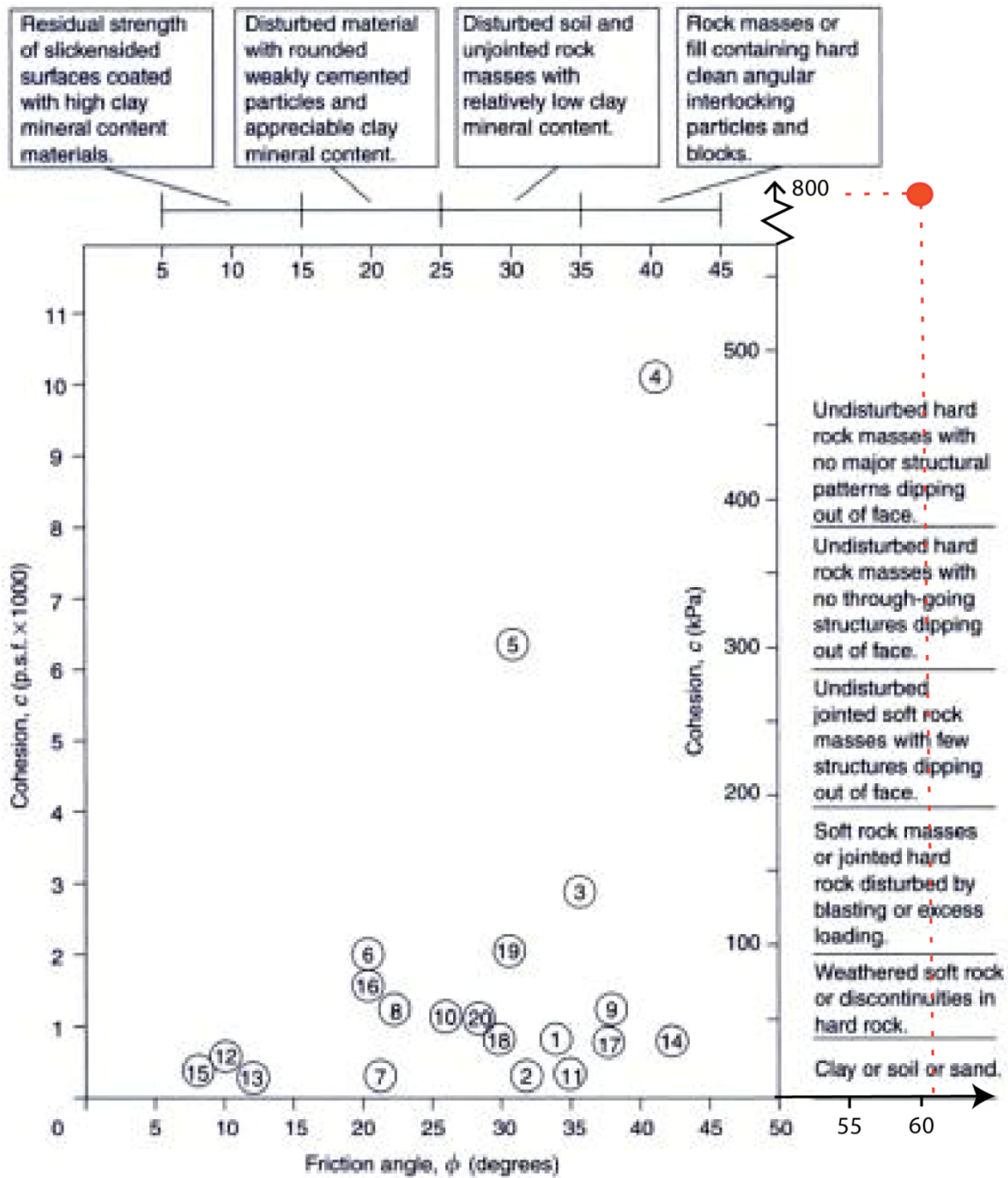
Figure 56: Overview chart showing the results of rock mass back analysis of slope failures. Tjellefonna rock mass is given with a friction angle of 62° and cohesion of 800 KPa, which is shown as the red circle. Figure from Wyllie and Mah (2004).

The instantaneous friction angle and cohesion is also applied to the discontinuities by the equations from Hoek (2007). Converting the Barton-Bandis parameters (φ_b, JRC, JCS) into instantaneous Mohr-Coulomb parameters (φ_i and c_i) gave reasonable results within a common range of values (Nilsen, 2012). The results from this conversion are realistic and matches the guidelines of Wyllie

and Mah (2004). The output results for φ are typical for discontinuities in high friction (34° to 40°) rock surfaces like basalt, granite and limestone.

The values used for stress field input come from analyses carried out in nearby areas, as there are no stress measurements available from Tjellefonna. Because of this approximation supplementary experiments were run with also other values (ratio equivalent for in and out of plane: 0.2 and 1). However, these experiments showed that varying input parameters only had a very small influence on the SSR analysis. This indicates that the chosen field stress parameters are appropriate for the modelling.

The input parameters of joint stiffness (normal and shear) are compared to obtained literature values in Table 25. It was not possible to find values from similar rock type as at Tjellefonna, still they may be used to evaluate the chosen joint stiffness values. Table 25 shows that J1 and J5 are modelled with reasonable values. Considering the stiffness of the faults, the assumed values are based on that clay infilling generally leads to lower strengths. This is supported by the user manual from UDEC, which shows that the normal stiffness for joints with clay-infilling ranges from 10 to 100 MPa/m (Wines and Lilly, 2003).

Table 25: Overview of some literature values of joint stiffness

K_n (MPa/m):	K_s (MPa/m):	Rock type:	Sources:
10 000	1000	Diorite	Fischer et al. (2010)
5000	1000	Paleozoic-Mesozoic sedimentary rocks	Brideau et al. (2010)
6000	2600	Meta-rhyolite	Loftesnes (2010)
7235	**2170**	Granitic-granodioritic gneiss	J1: calculated from laboratory work and RocLab
2989	**897**		J5: calculated from laboratory work and RocLab
100	**100**	Faults	Böhme (2012), Wines and Lilly (2003).

7.2.2. Model setup

The fieldwork from Sandøy (2011b) reveals that the back walls at Tjellefonna consist of sub-parallel joint sets J1 (157/59), J3 (352/47) and when well developed, also the undulating foliation (158/62, 338/70). The lateral boundaries of the scarp are defined by joint set J2 (076/81) and J4 (211/88). Also a set of shallow-dipping structures (J5, 160/27) that are parallel to J1, were mapped. However, this joint set was not observed in the scarp area during field mapping.

The main geological setup in Phase[2] consists of joint set J1 (spacing 30 meters), J5 (spacing 30 and 300 meters) and two parallel fault zones. Additionally, also a sub-horizontal fault was included. Joint set J3 are left out due to both long computing time and observations in field indicating that this set is less penetrative and persistent (compared to J1). The numerical setup neither includes the foliation, as it for the most part is poorly developed (rather LS- to L-tectonites). Besides, it is also difficult to implement the undulating foliation in Phase[2], as the folding pattern is rather complex. The outcrops at the shoreline of Tjellefonna support this, as the foliation here dips quite steeply (~ 60º), just like at the back-walls. Phase[2] computes the scenarios only in 2D sections, and because of this the joint sets defining the lateral borders (J2, J4) were not included.

The region of Tjellefonna has through geological time been a tectonically highly active area (see Chapter 2), as observed by mapping of several faults with varying characteristics and core widths (ranging from millimetre to several meters) (Sandøy, 2011b). Also the development of complex folding and observations of mineral lineations testify to this. The mapped faults at Tjelle were mainly parallel to J1 and the foliation (when present). It was only observed one fault zone (Tjelle fault) in the lateral back-wall of Tjellefonna. This one is included in the model as the fault zone nearest the slope face (Figure 57: red dashed line, Figure 33; Chapter 5.3.7). The Tjelle fault may be linked together with the so-called "Rød fault", as well as the back scarp of possible old landslides and a proposed DSGSD (Deep-seated Gravity Slope Deformation) at the Purka mountain (Sandøy, 2011b).
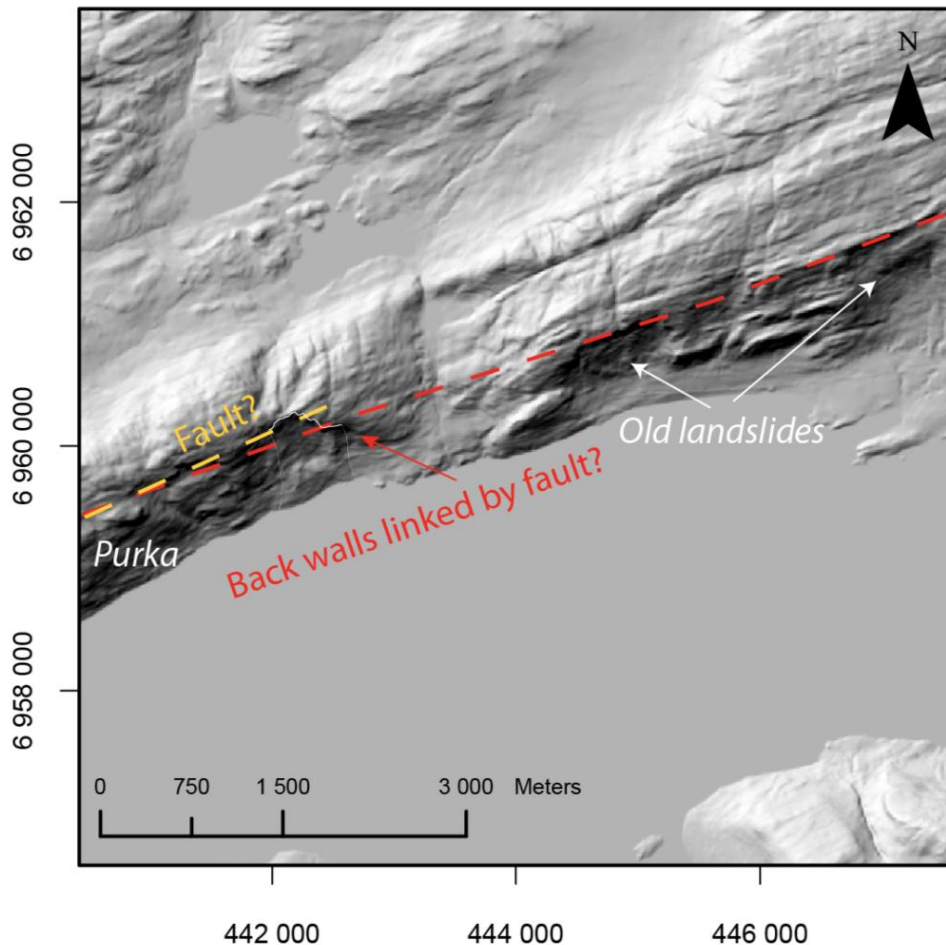
Figure 57: An overview map of Tjellefonna and the two main fault zones (Fault-set 1) used in the Phase² model. The location of the faults is based on the location of the Tjelle fault (red dashed line) and an interpreted fault near the present crown (orange dashed line). Note that the Tjelle fault seem to continue towards the present potential instable rock slope at Purka (SW), and to the NE towards two assumed older landslide back-scarps. See Sandøy (2011b) for more details.

A fault zone is also included below the present crown (Figure 57: orange dashed line, Figure 33; Chapter 5.3.7), although a fault core was not observed in field. This could be because the area consists of quite challenging topography and heavy vegetation. However, the rocks here are strongly influenced by a reddish alteration (red feldspar) (Sandøy, 2011b), indicating at least the presence of hydrothermal fluids (fluidization) and possibly also the influence of a deformation zone. These two fault zones are included in the different scenarios as Fault-set 1 and 2. Additionally, a sub-horizontal fault (Fault-set 3) was observed at an outcrop SW of the rockslide limit (Figure 62). The impact of this structure on the slope stability is investigated in the last numerical modelling (Analysis 5).

The groundwater table is included in the numerical modelling based on manual interpretation of the topography. It is difficult to predict how high the groundwater table normally is at the Tjellefonna area, which produces some uncertainties regarding the SRF results. Still, this approximation is considered appropriate to evaluate the groundwater influence on the stability. A very high groundwater table is also included in the analysis to model the effect of heavy rainfall over longer period. This follows the descriptions of the weather in the days leading up to the Tjellefonna failure, stating that there was about 14 days of heavy rain. To model this the groundwater table was drawn parallel to the surface.

Also the effect of pseudostatic earthquake is added based on historical sources. Such pseudostatic analyses have some drawbacks, like implementing the earthquake as a permanent body force and assuming the force to be constant, only acting in a direction that promotes slope failure. For this reason, the seismic coefficients are generally selected to be some fraction of the peak acceleration, as the peak acceleration in reality only acts briefly. Selection of the seismic coefficient is one of the most important aspect of the stability analysis, and one of the most difficult ones (Jibson, 2011). The database from NORSAR (Table 4; Chapter 4.1) shows that earthquakes in Møre & Romsdal ranges from a minimum of 1.6 to a maximum of 4.6, in between 1981 to 2010 (span of 29 years), with a mean magnitude of 2.7. The numerical modelling is based on this mean value, represented by the fraction (k=0.044) of this peak acceleration. Additionally, a magnitude 8.25 earthquake, representing a worst-case scenario, was included to test the influence of very large earthquakes on the stability. Nevertheless, a 8.25 magnitude earthquake is not regarded to be very plausible for the 1756 failure, as no historical accounts of such an event is recorded in nearby areas.

The doctoral thesis of Grøneng (2010) includes a Phase^2 slope modelling of the presently unstable rock slope at Åknes in Storfjorden (Møre & Romsdal). This study describes that elastic material is suitable for the evaluation of the in-situ stresses, while plastic materials can be used to identify potential failure planes. Through a discussion with Böhme (2012) it was clarified that assigning a plastic material to the model will force SSR to create a "sliding plane", which is not the goal. Based on this, an *elastic-plastic* and *strain-softening* model is applied to the rock mass, without any definition of a plastic material.

7.2.3.   Shear strength reduction (SSR) analyses

The numerical modelling is conducted through shear strength reduction (SSR) analysis. The traditional limit equilibrium method (LEM) is not carried out, as an numerical approach is considered to be more suitable when the basal failure surface is unidentified (Willie and Mah, 2004). In contrast to LEM, the SSR method can compute a critical sliding surface, even without specifying the shape of the slide surface (e.g. circular, planar) (Willie and Mah, 2004). Nevertheless, both of the methods are highly depended on subjective geological interpretations of the scenario. The methods also require a lot of field mapping and laboratory work to obtain a geological setup and parameters that is as close to reality as possible.

The impact of fault widths

The impact of fault width is investigated in Analysis 1.1 (Figure 44; Chapter 6.2.2). The results show that the SRF is not particularly influenced by the thickness of the faults, as Fault-set 1 (modelled as two joints) and Fault-set 2 (two material zones of 1-2 meters) gives almost the same results. Yet, there are some uncertainties related to this fault analysis because the slope stability is higher for the Model 2 setup (SRF = 2.46) contra a setup of only J1 and J5 (SRF = 2.27). This is a good example of the uncertainties associated with numerical modelling, as fault zones with low strength parameters (φ = 25, c = 0) should obviously weaken the model. A possible explanation of these results may be that the faults are not daylighting, and therefore not contributing to destabilizing the model. The rest of the analyses are based on Fault-set 1, as the widths of the fault zones apparently do not play a vital role in this version of Phase^2. Another reason is that Fault-set 1 has some shorter computing time.

The influence of strain softening

The first models were constructed with residual values equal to peak values, to test whether slope failure could occur without strength reduction. The interpretation from Analysis 1.2 is shown in Figure 45 (Chapter 6.2.2). All in all, the results reveal that an elastic-perfectly plastic model is not suitable for the Tjellefonna slide, as slope failure was not reached even at extreme conditions. The model is close to fail (SRF = 1.01) when Model 2 is supplemented with normal groundwater and an

earthquake magnitude of 8.25 (k = 0.15). Still, an earthquake magnitude of around 8 would cause enormous damage in an area of hundreds of kilometre around the epicentre. As mentioned earlier, this is obviously not the case as no written sources have described such damages.

It is therefore evident that for the present modelling some amount of strength reduction is necessary for the slope to fail. The main focus of the strain-softening scenarios (Analysis 2 and 3) was thus to investigate the impact of reduced residual values on the stability. The fault parameters were, however, decided to remain constant (φ = 25, c = 0), as the parameters were already quite low.

An overview of the strain-softening results is given in Table 26. In both analyses failure is only possible when including joint set J5 (Model 2). However, it requires a 30% strength reduction to fulfil the criterion of SRF < 1. Even with a high groundwater table included, the model will not fail with a strength reduction of 10 %. When including a seismic load in addition to this high groundwater table a reduction of 10 % is, however, sufficient. These analyses state that the failed rock mass and discontinuities require lower residual values than peak values. This is also supported in theory, as such large-scale rock mass generally exhibit brittle (strain softening) behaviour, consisting of residual strength that is lower than peak (Manfredinim et al., 1975).

Table 26: The results of strain-softening model of residual friction angle and cohesion.

Scenario:	Model:	Set up:	SRF:
Analysis 2: k = 0	2	30 % reduction	0.97
		10 % reduction, high groundwater*	1.12
Analysis 3: k = 0.044	2	10 % reduction, high groundwater	0.99
		30 % reduction	0.86

In general, and as can be seen in Table 27, the reduction of the rock mass residual strength is in the range of 10 to 15 % of the peak values. Based on these studies, a 30 % reduction of the rock mass at Tjellefonna might be too much. However, as the rock mass strength is extremely high and the instability of the slope is strongly related to the discontinuities, a 30 % reduction in the rock mass and the discontinuities together is regarded as realistic. This is supported by the observations in field that the rocks around the crown area are regularly highly blocky in character.

A 30 % strength reduction (Table 16, Table 17; Chapter 5.3.7) of the residual friction angle and cohesion of the discontinuities is high, but may be representative if rough surfaces are transformed

into smooth planes with no irregularities during creeping (Nilsen, 2012). Furthermore, Table 27 gives an overview of some residual friction angles obtained from literatures result of conducted laboratory tests. It can be seen in this table that clay infilling would also give a 20 - 30 % reduction. The joint sets seen in field consist of rock-to-rock contact, but gouge is frequently observed in the faults and wider fractures zones. A very widespread influence of gouge seems to be unrealistic. Nevertheless, the outcome of the analyses presented in Table 26 clearly shows that a relatively large reduction of the residual strength parameters is required.

Table 27: The shear strength of filled discontinuities and materials.

Rock:	Peak [°]	Residual [°]:	Difference:	Sources:
Coal measure rocks (infilled with clay mylonite seams)	16	11.5	**28**	After Barton (1973) in Hoek (2007)
Montmorillonite (80 mm seams of montmorillite clay in chalk)	14	11	**21**	
Conglomerate, sandstone, mudstone	58	51.8	**11**	Cai et al. (2007)
	5.8	51	**12**	
Porphrite	59.2	54.8	**7**	

Table 28: Comparisons of calculated peak friction angle (Barton-Bandis field data) to residual friction angle (tilt test).

	φ Peak [°]: (calculated*)	φ Residual [°]: (Tilt test)	Reduction of peak value:		
			10 %	30 %	50 %
J1	36	25	32	25	18
J5	45	21	41	32	23

The peak values of the discontinuities are as mentioned earlier based on a conversion of the Barton-Bandis field data to Mohr-Coulomb, from the equations by Hoek (2007). Comparing these to the residual values obtained from the tilt test (Table 28) gives a 28 % (J1) and 53 % (J5) reduction from

the peak friction angles. A 30 % reduction may be reasonable regarding J1, but a 50 % reduction of J5 may be too high, as the mean JRC value for this set is only moderate (9 of 20).

The role of the J5 discontinuity set on the slope stability

The comparison of Model 1 and Model 2 reveals that a shallow-dipping discontinuity (here as J5) has the highest structural impact (higher than J1 and the faults) on the critical SRF. Because none of the analyses of Model 1 fails, it strongly suggests that a shallow-dipping structure has to been present. This is in contrast to the field observations, which did not reveal any particularly pervasive flat or shallow-lying discontinuities. The J5 joint set was observed only locally, and is not characterized as very penetrative. Still, as the modelling shows, the presence of this joint set greatly reduces the critical SRF. In order to understand the influence of this joint set independently a series of analyses were preformed.

The impact of the chosen friction angle and cohesion for J5 is investigated in Analysis 4.1 (Figure 52; Chapter 6.2.4). The final overview illustrates that the friction angle has a much higher influence on SRF (reduced ~25 to 40 %) than the cohesion (reduced ~3 to 5 %). However, this very low impact of cohesion on the SRF seems to be somewhat underestimated, as the cohesion is in real-life connected to the friction angle contribution (Nilsen, 2012). Another result of interest is that the SRF reduction decreases when running the parameter study with c = 0 (friction angle constant, SRF = 2.34) compared to c = 0.0632 (SRF = 2.33), which give no geological sense. These results indicate that some improvements of Phase^2 might be required. Yet, the influence of cohesion on the stability of slopes is commonly much less important than the friction angle (Terzaghi, 1962). This is seen in the Mohr-Coulomb criterion (equation 10; Chapter 5.3.2), as cohesion is included as a constant while the friction angle varies more greatly (i.e. larger influence).

Because rather few field observations of J5 were made (Sandøy, 2011b), the impact of joint spacing is studied in Analysis 4.2 (Figure 53; Chapter 6.2.4). At a spacing of 30 meters the joints daylight the slope face of Tjellefonna, representing the worst-case scenario (Figure 34; Chapter 5.3.7). In contrast, when using a 300 meters spacing the applied joints do not daylight (Figure 33; Chapter 5.3.7). The analysis shows that the SRF decreases with decreasing spacing, but does not fail. It is interpreted that this reduction in SRF between the two models to a large extent is related to whether the discontinuities daylight or not. The analysis shows that the friction angle has a higher influence on the reduction of SRF than spacing.

Table 29: An overview of some critical results from Analysis 4.3

Model:	Set up:	SRF
2 (spacing = 300 m)	30 %, high groundwater	0.94
4 (spacing = 30 m)	30 %, high groundwater	0.86

Table 29 outlines the setups of Analysis 4.3 that yielded a critical SRF below 1. Both of the spacing distances give a SRF < 1 when reducing the friction angles by 30 % (φ= 32°) and 50 % (φ = 23°) in combination with high groundwater table. These "new" peak friction angles are compared to laboratory results from the tilt test (Sandøy, 2011b), which gave a basic friction angle (φ_b) of 29°. As J5 is composed of a JRC of around 9 (rough surface), peak friction angles of 32° or 23° is not very reasonable as they are close to the basic friction angle, representing a smooth planar surface. Furthermore, Table 23 (Chapter 6.2.4) shows that the mean difference between the critical SRF is only 11 %. It seems that the spacing has less influence when reducing the friction angles to 30 % and 50 % (difference 9 % and 11 %), compared to running the models with constant friction angles of 45º (difference 14 % and 16 %)

7.2.4.   Summary of trigger mechanisms

Historical sources testify that the Tjellefonna failure took place after a long period of heavy rain. In addition to observations of water running down into the tension cracks from the marsh, these observations indicate that the presence of water must have been an important triggering mechanism of this large-scale rock slide (see chapter: 1.4). All numerical analyses (Analyses 1.2 to 5) support the importance of high groundwater. For example it is in Analysis 1.2 shown that the presence of groundwater drastically reduces the SRF (~ 30% to 50%) (Figure 58). It is also revealed in Figure 58 and 59 that the influence of groundwater is significantly higher than the effect of an earthquake load (7 % to 27 %). The figures also state that the presence of groundwater is more important than the impact of the shallow-dipping joint set J5.

Analysis 4.3 (Figure 54; Chapter 6.2.4) investigates the SRF influence of trigger factors at different spacing and friction angles of J5. A critical SRF almost below one (SRF = 1.01) was obtained at

96

spacing of 30 meters with a friction angle of 45°, high groundwater and a seismic load (k = 0.044).

Comparing this result to the results in Analysis 4.2 (Figure 53; Chapter 6.2.4) shows that failure did not occur at a spacing of 30 %, even with a 50 % reduction of the friction angle (SRF = 1.23). This clearly shows that additional triggering factors are essential to promote failure.

Although an earthquake magnitude of 2.7 is feasible to occur along the coastal areas of Norway, an earthquake magnitude of around 6, which is normally considered as the lower limit for triggering rock failures, is uncommon (Jibson, 1994; Keefer, 1984). An earthquake magnitude around 3 could be felt by people, but would not cause damage to the surroundings (USGS, 2012). Morsing (1756) describes that household objects where shaken down on the floor at houses located near the fjord, and specified that an earthquake must have preceded the rockslide. However, as a magnitude of around 3 is too low to shake down items indoor, this either means that the earthquake magnitude was higher (4 to 5; (USGS, 2012), or that the shaking from the collapsing rock mass was mistaken for an earthquake. As all of the accounts of an earthquake comes from close to Tjelle, it is inferred that the rock failure of Tjellefonna was not triggered by an earthquake, and that the shaking experienced came from the tumbling rock mass. That a rockslide can create earthquake-like signals is stated in a study of Dammeier et al. (2011), where seismic data is used for remote characterization of rock slope failures.

In sum the most important triggering factor is considered to be the presence of groundwater. Additionally, the analyses show that the influence of groundwater is more important than the shallow-dipping structure (here as J5).
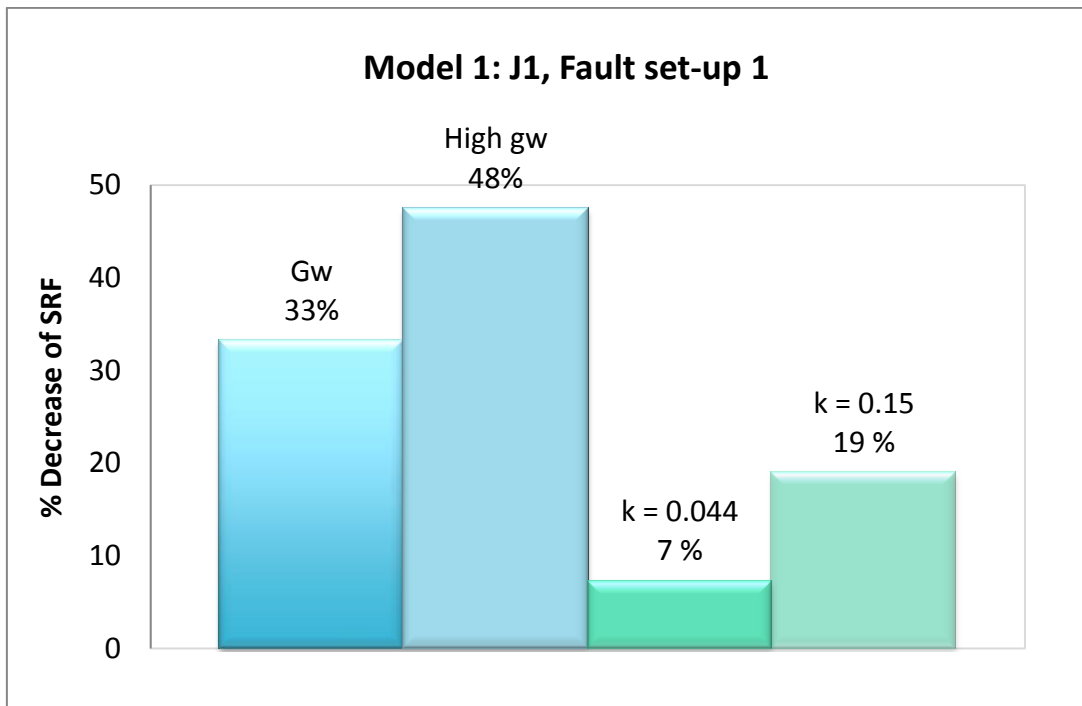
Figure 58: An overview of the SRF decrease (%) of model 1 when including triggering factors.
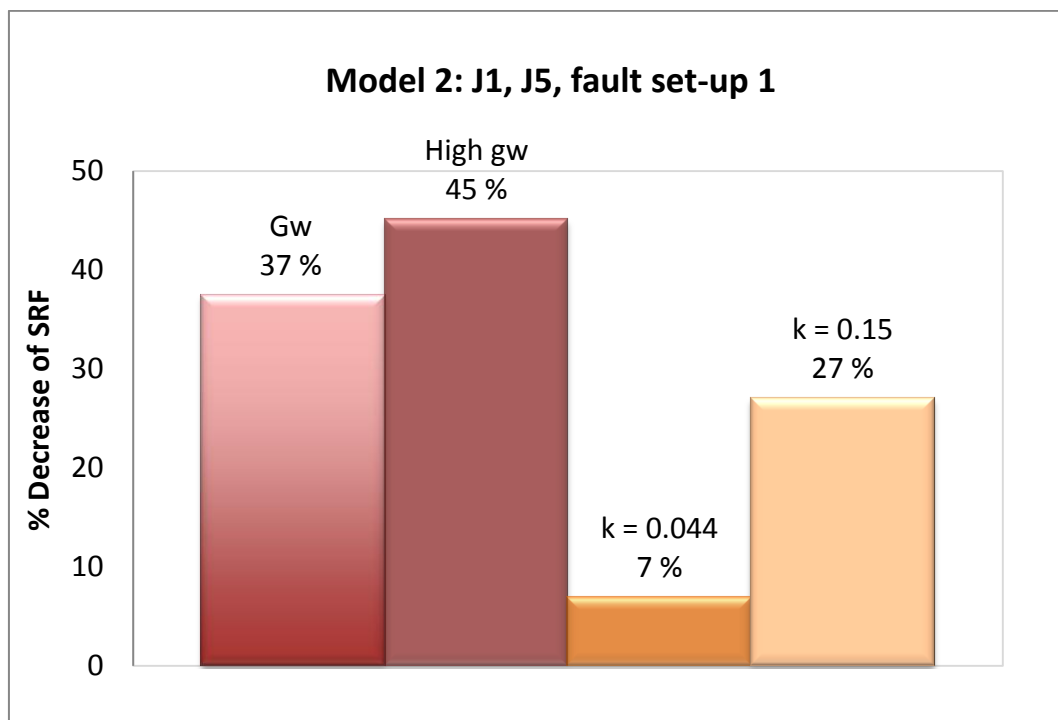
Figure 59: An overview of the SRF decrease (%) of model 2 when including triggering factors

7.3. Comparison and discussion of sliding planes

Figure 60 shows the interpreted sliding surfaces based on SLBL and Phase[2] (maximum shear strain and ubiquitous joints). It seems like both the maximum shear strain (shown as red dashed line) and SLBL methods (blue continues line) have similar daylight zones (Figure 60). However, the location of the maximum shear strain, in the model with no discontinuities goes deeper (~100 meter) and also extends further behind the observed back scarp (Figure 46A; Chapter 6.2.2). The results of the shear strain development when including J1 and Fault–set 1 gives a similar location of the shear strain zone, but now only limited by the backmost fault (Figure 46B-C; Chapter 6.2.2). From Figure 60 it can be stated that the SLBL method is more precise, but that the shear strain development is useful as a first approximation to determine basal failure surfaces.
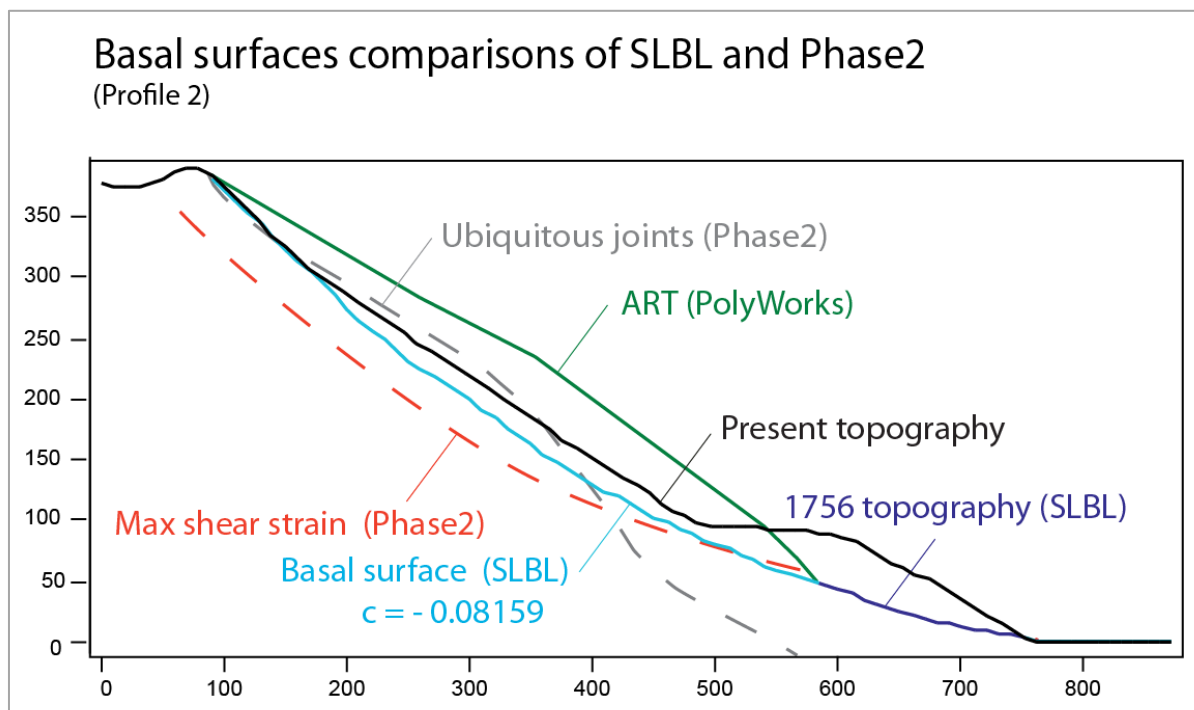
Figure 60: The interpreted gliding surfaces from SLBL method and Phase[2]. The initial failed area is drawn in green, based on manual ART reconstructed in PolyWorks. Black line represents the present topography.

When running Phase[2] without SSR analysis an interpretation of the safety factor is conducted by the "ubiquitous joints"-tool. A comparison of the interpreted basal surface based on the strength factors is given in Figure 60 (grey dashed line). The expressed sliding surface lies locally above the present-

day topography (black continuous line) and therefore appears not to be a useful tool in this case study. Nevertheless, it fits better at the present back-scarp compared to the maximum shear strain development.

The computed SLBL sliding surface seems to give the most reasonable results, as it corresponds well with field observations at the present crown area and of the deposit thicknesses. Still, the lack of observation of possible sliding surfaces and the diverging modelling results indicate that the basal surface of the Tjellefonna slide could be more complex.

Bugge (1936) proposed that the Tjellefonna consisted of similar structures as in the Loen rock failure, which was build up of steep fracture sets combined with a less steep gouge-filled fracture-set. The numerical Phase^2 modelling results support this theory, since failure requires the presence of some sub-horizontal structure that daylights in the rock slope.

The only mapped joint set that may match Bugge`s suggestion is J5, but this is as earlier mentioned rarely seen in field. Given the characteristics of J5, having a small extent (~ 5 to 15 cm) and being only slightly penetrative, it is considered that this joint set could not alone build up the basal failure surface of Tjellefonna. This is also supported by a structural analysis of the back scarp using terrestrial laser scans (Figure 61) conducted in the Coltop3D software (Oppikofer, 2012). In this analysis it was not discovered any flat structures, showing that this joint set has too low persistency and occurrence to have a major influence. The only "flat" structure present in the Coltop3D analysis of the back walls is the folded foliation, which reaches a minimum dip of around 40º (Figure 61). Yet, J5 may be important in the rock failure as a whole, since shear failure could proceed along the J5 paths and into potential existing intact rock bridges. J5 could also locally be parallel to the undulating foliation (when we-developed), as seen in Figure 63.

Field mapping of the deposits (Sandøy, 2011b) reveals that some of the blocks have well developed undulating and planar surfaces following the banding. This indicates that the foliation could act locally as a sliding surface, but it is in general not sufficiently developed to alone cause a failure. This statement is based on the field mapping, which showed that the foliation is predominantly steep dipping (~ 60°), both in the crown area and all the way down to the shoreline. However, it should be taken into consideration that the steep foliation may be folded underneath the present deposits (mean thickness of 23 meters), and therefore not possible to map. A conceptual illustration of this structural scenario is given in Figure 63.

100
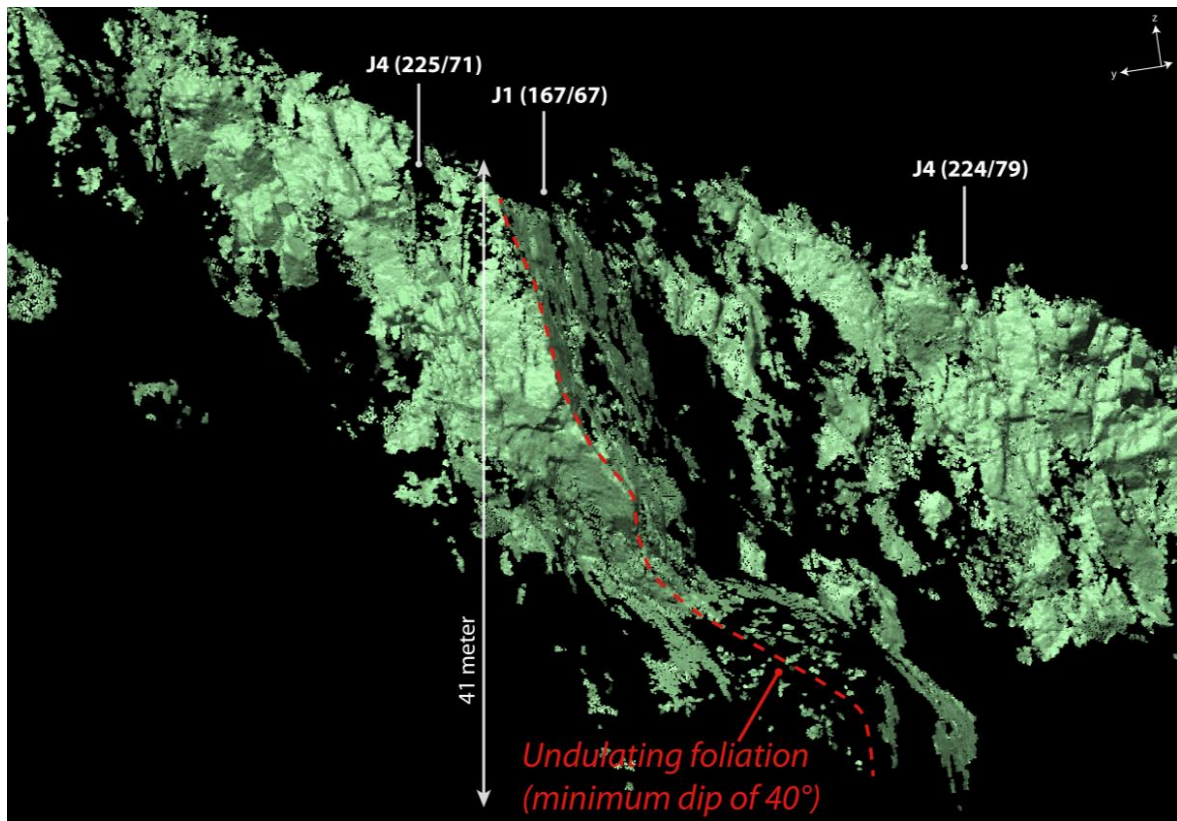
Figure 61: The results of the terrestrial laser scans (TLS) modified from Sandøy (2011b). Note that the red dashed line represents the undulating foliation, which is running parallel to J1 at the upper parts, while in the lower parts consisting of undulating surface with minimum dip of around 40⁰.

A structural feature that is of great interest in this matter, and which could be very important for understanding the destabilization of the Tjellefonna rock mass, is a sub-horizontal fault (Figure 62A-E) located a few tens of meters southwest of the toe area (Sandøy, 2011b). This sub-horizontal fault consists of an undulating surface varying between 350/20, 172/12 and 000/02, but for the most part striking parallel to Langfjorden. It extends across an outcrop that is around 20 meters wide and consists of fractured rocks and fault gouge with a thickness of around 2 to 7 cm (Figure 62C). It is interesting to notice that the rocks in the overlying block are strongly normal faulted (Figure 62B, D), while the lower block appears to be more intact. The normal faults are oriented sub-parallel to the J2 and J4 joint sets. Figure 62B illustrates how these rotated normal fault blocks terminates along the basal low-angle fault. Mineral lineation along one of these normal faults indicates that the sub-surface movement was oblique-dip slip towards southwest (Figure 62B, D). The heavy fracturing and clay-infilling of these overlaying rocks would contribute to a greatly reduced residual strength, as has been shown in Phase[2] to be important. A discussion with Redfield (2012) also confirmed that this

structure must have been formed as a brittle fault at depths, as a horizontal zone would not develop such an open crack clay in-filling at later stages.

Numerical modelling includes this horizontal fault (Fault-set 3) in Analysis 5, and it is assumed this fault zone continues across the rockslide (Figure 62E). When combining this fault setup with a strain softening of 10 % and high groundwater failure occurs in both Model 1 and Model 2. These results prove that this sub-horizontal fault zone could play a vital role in explaining the Tjellefonna failure, as failure occurs even without including joint-set J5 (Model 1). Additionally, the character of the fractured rock mass overlying the flat-lying fault poses as a key to understand the complex failure at the slope toe. The nature of this locality indicates that compartmentalization of the rock mass, created during faulting episodes, might be an important aspect of the Tjellefonna failure.

It seems that the sliding surface does not consist of a uniform plane, but rather stepped pathways of more or less intact rock bridges formed by the discontinuities (J1, J3, J5), the foliation and the fault zones. This conceptual model of the step-path failure surface is illustrated in Figure 63. The sliding plane in large-scale rockslides is in most cases not uniform, but a combination of unfilled joints, gouge-filled faults and intact rock bridges. Such complex sliding surface is interpreted at the Vaiont slide (1963, Italia) and at the presently unstable rock slope at Åknes, Norway (Grøneng, 2010; Oppikofer et al., 2011). A complex basal surface composition of Tjellfonna is in accordance with the kinematic analysis carried out by Sandøy (2011b), where no clear failure mechanism was possible to obtain.
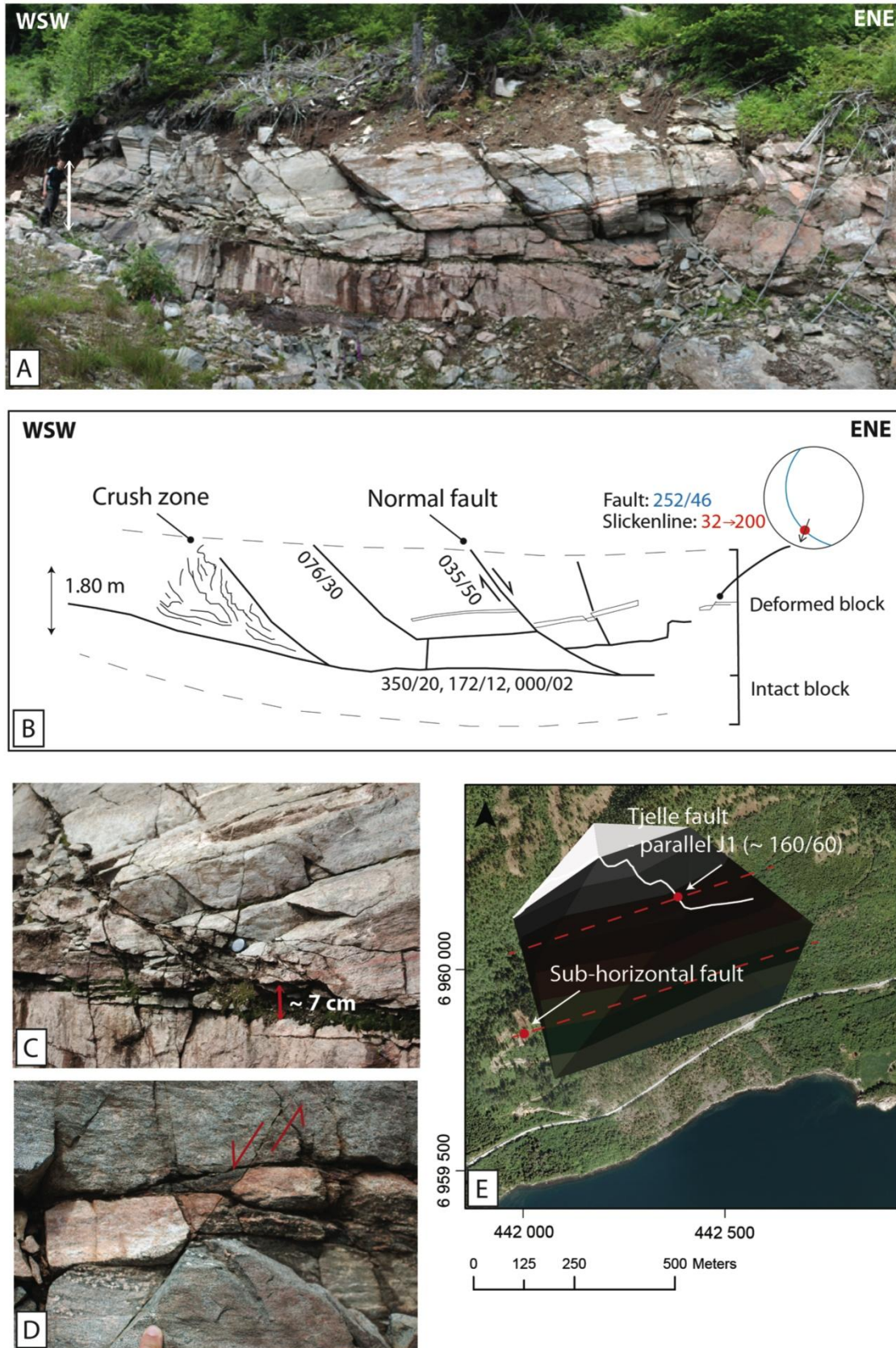
Figure 62: An illustration of the sub-horizontal fault, where A) is an overview picture, B) a sketch of the block structures, C) a close-up of fault gouge, D) a normal fault and E) the location of this sub-horizontal fault, SW of rockslide limit.
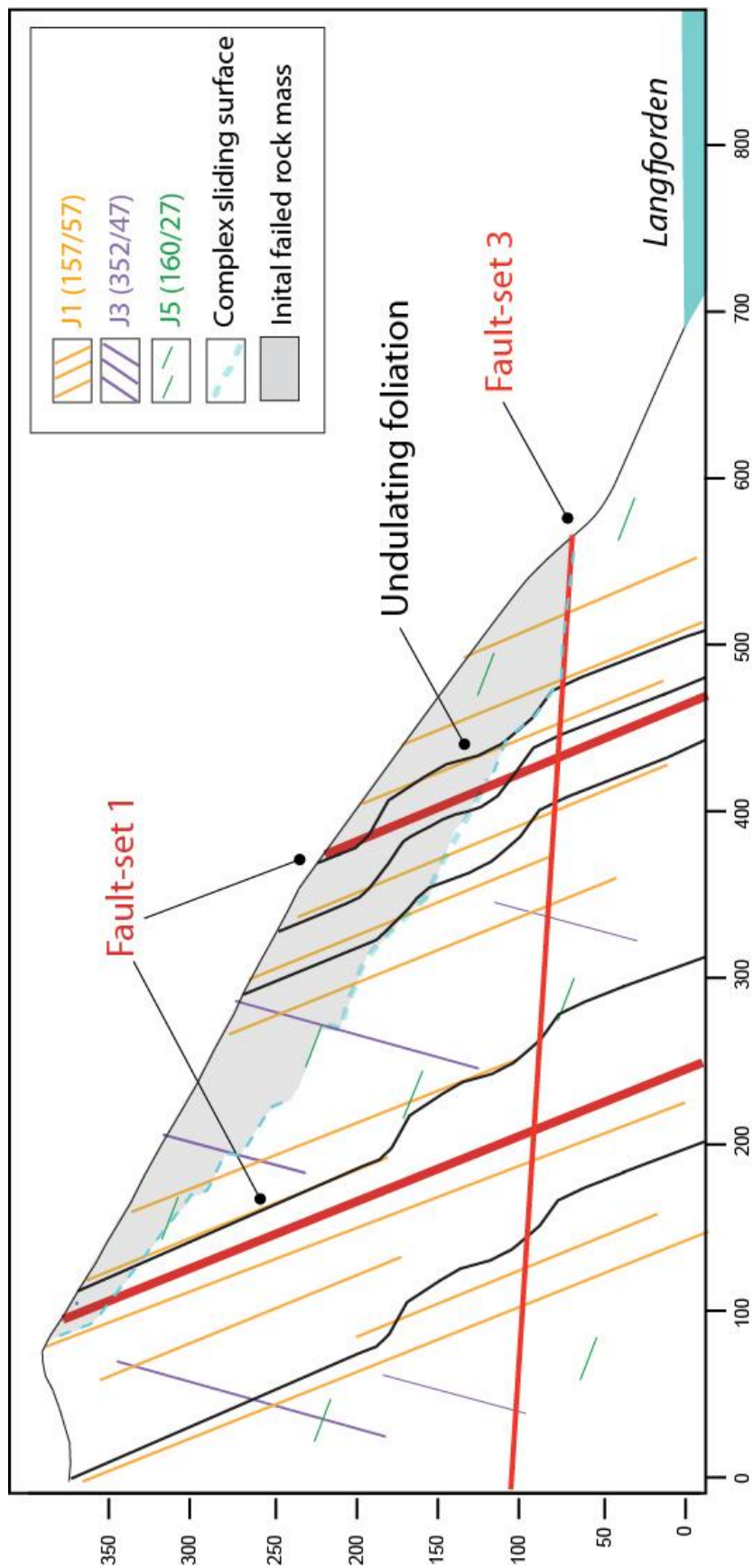
Figure 63: A conceptual model based on fieldwork and numerical results.

7.3.1. Summary of the failure conditions

Table 30 summarizes all of the model setups that lead to possible failure. As seen, there are several different scenarios promoting instability, but of these a setup with high groundwater and 10 % reduction of the residual values, as well as a setup with a 30 % reduction without groundwater dominate.

Also of interest is Model 3 in Analysis 4.3, which has no reduction of strength parameters, and fails with only a reduced spacing of J5 (30 meters) in combination with high groundwater and a 2.7 magnitude earthquake. This stats the importance of a sub-horizontal structure, however, such high frequency of J5 may not to be reasonable as it is rarely observed in field. The worst-case scenarios occur when including an additional sub-horizontal structure in Analysis 5 (Fault-set 3), in combination with high groundwater table. As both Model 1 and Model 2 becomes unstable in Analysis 5, this sub-horizontal fault may be a very important reason for the 1756 failure. Notice also that this scenario results in the lowest SRF compared to the other similar setups (i.e. 10 % reduction of residual values).

Table 30: An overview of the Phase^2 analyses that gave SRF below (or very close to 1).

Scenario:	Model:	Set up:	SRF
Analysis 1.2	2	Groundwater, earthquake (k = 0.15)	1.01
Analysis 2: k = 0	2	30 % reduction*	0.97
		10 % reduction*, high groundwater	1.12
Analysis 3	2	10 % reduction*, high groundwater, k = 0.044	0.99
		30 % reduction*	0.86
Analysis 4.3	2	30 % reduction (φ), high groundwater	0.94
	3	High groundwater, k = 0.044	1.01
	3	30 % reduction (φ), high groundwater	0.86
Analysis 5	1	10 % reduction*, Fault-set 3, high groundwater	0.93
	2	10 % reduction*, Fault-set 3, high groundwater	0.86

*= Strain softening: Residual values of rock mass and joints reduced 10 % or 30 % of peak values.

A question of interest is also why the failure took place in February 1756. Eberhard et al. (2001) suggested that in order to evaluate this question a consideration of two factors is needed: (1) The initial slope conditions (or system processes) and (2) the triggering mechanisms. For large scale slope failures it is important that there is a component of strength degradation with time (e.g. creep, fracture propagation, stress changes and weathering) (Eberhard et al., 2001). These factors will reduce the strength (lower residual values) between locked joint surfaces and/or intact rock bridges between the discontinuities. When the rock mass is sufficiently weakened failure may be initiated by one or more triggering mechanisms.

It is suggested that the Tjellefonna failure is considered as an initial *progressive accumulation* of rock weakening (strain softening) acting to degrade the equilibrium state of the slope. This initial incremental hillside creep was attained through hundreds of years of freezing-thaw cycles (Redfield and Osmundsen, 2009), by glacier erosion, by glacio-isostatic burial and uplift, and through long-term water infiltration. Additionally, the region is, and has been, effect by low-magnitude earthquakes, which could through time also lead to a progressively weakening (Figure 15; Chapter 4.1.1). This progressive reduction of the effective strength of the rock mass and intact rock bridges resulted in incremental creep as was observed as tension cracks developed on the top of the present crown. In the end the loosely intact rock mass was finally triggered by a 14 day period of heavy precipitation.

8. Conclusions

This master thesis uses field and laboratory data acquired during the fall 2011, and presented in a project report in December 2011, to do a back-analysis of the 1756 Tjellefonna rockslide. The following key points combine to give a better understanding of the mechanisms related to this historical failure as well as similar large-scale rockslides.

- It is found that a realistic back-analysis (reconstruction of topography and volume estimation) of ancient rockslides is possible by the use of GIS software in combination with SLBL and PolyWorks.

- When applying the SLBL and PolyWorks techniques it is essential to use both methods in order to evaluate the accuracy of the final ante-rockslide topography (ART), and the following volume estimations. The profile set up is highly depended on subjective geological interpretations, as both methods require a number of assumptions.

- Well-constrained basal failure surface (SLBL) and reconstructed topography (SLBL and PolyWorks) is also important for subsequent numerical modelling, as the final profile is used in Phase^2.

- Using the ante-rockslide topography and basal failure surface the volume of the initial 1756 rockslide is recalculated to have been around 9 to 10 million m^3, which is lower than previous estimation (12 to 15 million m^3). This has consequences for the modelling of rockslide-generated tsunamis in Norway (e.g. Åknes).

- The SLBL method produces more realistic basal surfaces than the methods in Phase^2 (maximum shear strain, ubiquitous joints). However, interpretation of maximum shear strain when excluding geological structures gives a good first estimation of a possible failure surface.

- Numerical modelling is associated with uncertainties regarding the input parameters and the individual geological interpretations. The results show that friction angle has significantly more influence than cohesion on the critical SRF value. It is clear that some amount of strain softening has to be associated with the failure, and perhaps as much as 30 %.

- The Phase[2] results of Tjellefonna reveal that a sub-horizontal structure is required for failure to occur. This could be represented by either the shallow-dipping J5 discontinuity set or a sub-horizontal fault (Fault-set 3). Based on field observations and Phase[2] modelling the sub-horizontal fault is regarded to be the most important of these.

- Field experience and modelling shows that the complex basal surface is composed of intact rock bridges in combination with unfilled and gouge-filled joints (influenced by faulting). It is proposed that the failure surface of the 1756 Tjellefonna slide is a combination of all the structural features present (joint sets J1, J3 and J5, the foliation and the faults). It is, however, obvious that the Tjellefonna failure is closely depended on the presence of faults. This is also illustrated by the difference in number of historical rock failures between the northern and southern part of Langfjorden. All rock failures around Langfjorden have occurred on the northern side, in which is significantly more influenced by tectonic deformation than the rocks on the southern side.

- The numerical modelling demonstrates that the 1756 failure could not have taken place without the presence of a high groundwater table. This fits well with the historical sources. It is shown that groundwater has a much larger influence on the shear reduction factor (SRF) than the seismic load from an earthquake.

- It is unlikely that an earthquake triggered the rockslide. Modelling shows that an earthquake with magnitude of 2.7 could not be a trigger on its own. As an earthquake magnitude of 6 is normally required to trigger a rockslide, and as there are no accounts of such an event in Møre & Romsdal at this time, an earthquake is ruled out as a trigger mechanism. It is more likely that the shaking from the tumbling rock mass was mistaken as an earthquake.

- A combination of heavy rainfall, freezing thawing cycles and the presence of earthquake (triggering over long time) would weaken the rock mass significant. Tjellefonna failure is most likely a consequence of *progressive accumulations,* which generated hillside creep and fracturing of the intact rock bridges. This progressive creep would explain the observation of growing tension cracks located at the present crown prior to the failure.

- Numerical modelling using Phase^2 is only one method to recreate the 1756 failure. The 2D modelling includes several simplifications, as excluding foliation and discontinuities running parallel to the model. The simplifications and uncertainties of the results are shown by the example where discontinuities in combination with fault zones lead to an increased stability relative to the faults alone. Still, the modelling is very useful to get a better understanding of the relative importance of the different factors related to this large-scale rockslide.

9. Perspectives

Even though the Tjellefonna has been intensively studied during the project assessment in autumn 2011 and this master thesis, several important topics still require further investigation. The following points give suggestions for future work and improvements:

- A seismic survey of Langfjorden was carried out by NGU in the autumn of 2011, but the seismic data was not processed in time to be used in this thesis. Further work should include comparison of the seismic results of the offshore-debris thickness to the SLBL results. Possible re-calculation of the volume is required if the new seismic data does not correspond to the interpreted debris limits and the SLBL results.

- Another topic that requires attention is the characterization of the sliding surface. A more detailed field mapping of the sub-horizontal fault is necessary. A study of the mineral lineations would give more understanding of the deformation story. Additionally, the extent of this sub-horizontal fault should be investigated, e.g. through refraction seismic.

- Develop a Phase^2 model setup with rock bridges of J1, J5 and J3. This may be done by calculating joint set properties based on a combination of discontinuities and intact rock properties, as developed by Jennings (1970) and used recently in Fischer et al. (2010). It is also recommended to construct a 3D graph of the input parameters (SRF, friction angle and cohesion), which requires running the model several more times.

- A numerical discontinuum model by using e.g. the UDEC software should be performed to supplement and compare the Phase^2 results, since there was not enough time for this during this thesis.

- The collected seismic surveys of Langfjorden should also be used to see if the Tjellefonna failure occurred in different compartments.

- Update the tsunami model from NGI using new volume estimations of the deposits.

10. References

Andersen, T.B., Jamtveit, B., **1990**. *Uplift of deep crust during 456 orogenic extensional collapse: a model based on field studies in 457 Sogn-Sunnfjord reion, W-Norway*. Tectonics 9, 1097 - 1111.

Austrigard, B., **1976**. *Nytt om Tjellefonna*, in: Hola, O. (Ed.), Romsdalsmuseets årbok 1976. pp. 45 - 51.

Ballantyne, C.K., **2002**. *Paraglacial geomorphology*, Quaternary Science Reviews pp. 1935 - 2017.

Barton, N., **1973**. *Review of a new shear strength criterion for rock joints*. Eng. Geol., 287 - 332.

Barton, N., Choubey, V., **1977**. *The shear strength of rock joints in theory and practice*. Rock Mechanics 10, 1 - 54.

Barton, N., Lien, R., Lunde, J., **1974**. *Engineering classification of rock masses for the design of tunnel support* Rock Mechanics 6 (4), 189 - 236.

Bauck, S.M., **2010**. *Fault rock assemblages and fault architecture in the Møre - Trøndelag Fault Complex*. NTNU, Trondheim, p. 97.

Blikra, L.H., Braathen, A., Anda, E., Stalsberg, K., Longva, O., **2002**. *Rock avalanches, gravitational bedrock fractures and neotectonic faults onshore northern West Norway: Examples, regional distribution and triggering mechanisms*. NGU, Trondheim, p. 48.

Blikra, L.H., Longva, O., Braathen, A., Anda, E., Dehls, J.F., Stalsberg, K., **2006a**. *Rock slope failure in Norwegian fjord areas: examples, spatial distribution and temporal pattern*, in: Evans, S.G., Mugnozza, G.S., Strom, A., Hermanns, R.L. (Eds.), Landslides from Massive Rock Slope Failure. Springer, Dordrecht, pp. 475 - 494.

Blikra, L.H., Longva, O., Braathen, A., Anda, E., Dehls, J.F., Stalsberg, K., **2006b**. *Rock slope failures in Norwegian fjord areas: examples, spatial distribution and temporal pattern*, in: Evans, S.G., Mugnozza, G.S., Strom, A., Hermanns, R.L. (Eds.), Landslides from Massive Rock Slope Failure. Springer, pp. 475 - 496.

Braathen, A., Blikra, L.H., Berg, S.S., Karlsen, F., **2004**. *Rock-slope failures in Norway; type, geometry, deformation mechanisms and stability*. Norwegian Journal of Geology Vol. 84, 67 - 88.

Brekke, H., **2000**. *The tectonic evolution of the Norwegian Sea continental margin, with emphasis on the Vøring and Møre Basins*, in: Nøttvedt, A. (Ed.), Dynamics of the Norwegian Margin. Geological Society of London, pp. 327 - 378.

Brideau, M., Pedrazzini, A., Stead, D., Froese, C., Jaboyedoff, M., van Zeyl, D., **2010**. *Three-dimensional slope stability analysis of South Peak, Crowsnest Pass, Alberta, Canada*. Landslides 8 (2), 139 - 158

Brückl, E.P., **2001**. *Cause-Effect Models of Large Landslides*. Natural Hazards 23 (2), 291 - 314.

Bugge, A., **1936**. *Fjellskred Fra Topografisk Og Geologisk Synspunkt*. Norwegian Journal of Geology, 342 - 360.

Böhme, M., **2012**. *Personal communication about phase2*, Trondheim.

Cai, M., Kaiser, P.K., Tasaka, Y., Minami, M., **2007**. *Determination of residual strength parameters of jointed rock masses using the GSI system*. International Journal of Rock Mechanics and Mining Sciences 44, 247 - 265.

CDMG, **1997**. *Guidelines for evaluating and mitigating seismic hazards in California*. California Division of Mines and Geology.

Dammeier, F., Moore, J.R., Haslinger, F., Loew, S., **2011**. *Characterization of alpine rockslides using statistical analysis of seismic signals*. Journal of Geophysical research Vol. 116.

Derron, M.H., Jaboyedoff, M., Blikra, L.H., **2005**. *Preliminary assessment of rockslide and rockfall hazards using a DEM (Oppstadhornet, Norway)*. Natural Hazard and Earth System Sciences, 285 - 292.

Duncan, J.M., **1996**. *State of the art: Limit equlibrium and finite-element analysis of slopes*. Journal of Geotechnical Engineering 122 (7), 577 - 596.

Eberhard, E., **2003**. *Rock Slope Stability Analysis - Utilization of Advanced Numerical Techniques*. University of British Columbia (UBC), p. 39.

Eberhard, E., **2006**. *From cause to effect: Using numerical modelling to understand rock slope instability mechanisms*, in: Evans, S.G., Mugnozza, G.S., Strom, A., Hermanns, R.L. (Eds.), Landslides from massive rock slope failure and associated phenomena. Springer, Dordrecht, The Netherlands, pp. 85 - 101.

Eberhard, E., Willenberg, H., Loew, S., Maurer, H., **2001**. *Active rockslides in Switzerland - understanding mechanisms and processes*, LANDSLIDES - Causes, Impacts and Countermeasures, Davos, Switzerland, pp. pp. 25 - 34.

Elgin, M., **2005**. *Creating and using digital elevation models*. Beca International Consultants Ltd.

ESRI, **2011**. *ArcGIS Resource Center Desktop 10 online help* Downloaded from: http://help.arcgis.com/en/arcgisdesktop/10.0/help/.

Etzelmüller, B., Romstad, B., Fjellanger, J., **2007**. *Automatic regional classification of topography in Norway*. Norwegian Journal of Geology 87, 167 - 180.

Evans, S.G., Hungr, O., Clague, J.J., **2001**. *Dynamics of the 1984 rock avalanche and associated distal debris flow on Mount Cayley, British Columbia, Canada; implications for landslide hazard assessment on dissected volcanoes*. Engineering Geology 61 (1), 29 - 51.

Farsund, T.Ø., **2011**. *Geological and numerical stability modelling of Mannen Romsdalen*, Department of Geology and Mineral Resources Engineering NTNU, Trondheim.

Fischer, L., Amann, F., Moore, J.R., Huggel, C., **2010**. *Assessment of periglacial slope stability for the 1988 Tschierva rock avalanche (Piz Morteratsch, Switzerland)*. Engineering Geology 116 (1-2), 32 - 43.

Furseth, A., **2006a**. *Tjellafonna - norgeshistoriens største fjellskred*, Skredulykker i Norge. Tun Forlag, pp. 151 - 155.

Furseth, A., **2006b**. *Tjellefonna - 250 år etter*, Årbok for Romsdal Sogelag, Molde, pp. 7 - 30.

Gee, D.G., **1975**. *A tectonic model for the central part of the central part of the Scandinavian Caledonides*. American Journal of Science 275-A, pp. 468 - 515.

Goodman, R.E., **1989**. *Introduction to rock mechanics*. John Wiley & Sons.

Gorum, T., Gonencgil, B., Gokceoglu, C., Nefeslioglu, H.A., **2008**. *Implementation of reconstructed geomorphologic units in landslide susceptibility mapping: the Melen Gorge (NW Turkey)*. Natural Hazards 46, 323 - 351.

Grøneng, G., **2010**. *Stability Analyses of the Åknes Rock Slope, Western Norway*, Department of Geology and Mineral Resources Engineering. NTNU, Trondheim, p. 55.

Grønlie, A., Naeser, C.W., Naseser, N.D., Mitchell, J.G., Sturt, B.A., Ineson, P., **1994**. *Fission track and K/Ar dating of tectonic activity in a transect across the Møre - Trøndelag Fault Zone, Central Norway*. Norw. J. Geol. 74, 24 - 34.

Grønlie, A., Nilsen, B., Roberts, D., **1991**. *Brittle deformaion history of fault rocks on the Fosen Peninsula, Trøndelag, Central Norway*. Norges Geologiske Undersøkelse Bulletin 421, 39 - 57.

Grønlie, A., Roberts, D., **1989**. *Resurgent strike-slip duplex development along the Hitra-Snåsa and Verran Faults, Møre - Trøndelag Fault Zone, Central Norway*. Journal of Structural Geology 11 (3), 295 - 305.

Hacker, B.R., Andersen, T.B., Johnston, S., Kylander-Clark, A.R.C., Peterman, E.M., Walsh, E.O., Young, D., **2010**. *High - temperature deformation during continental - margin subduction & exhumation: The ultrahigh-pressure Western Gneiss Region of Norway*. Tectonophysics 480 (1-4), 149 - 171.

Hammah, R.E., Curran, J.C., Corkum, B., **2004**. *Stability analysis of rock slopes using the finite element method*. Eurock 2004 & 53rd Geomechanics Colloquium.

Hammah, R.E., Yacoub, T.E., Corkum, B.C., Curran, J., **2006**. *A comparison of finite element slope stability analysis with conventional limit equilibrium investigation*, Proceedings of the 58th Canadian Geotechnical and 6th Joint IAH-CNC and CGS Groundwater Specialty Conferences Saskatoon, Saskatchewan, Canada.

Hanssen, T.H., **1998**. *Rock Stresses and tectonic activity*, in: Alten, T., Hermann, S., Beitnes, A., Berg, K. (Eds.), Fjellspregningsteknikk Norsk jord- og fjellteknisk forbund, Oslo, pp. chapter 29.21 - 29.21.

Harbitz, C.B., Glimsdal, S., Løvholt, F., **2011**. *Numerical simulations of tsunamis from potential and historical rock slides in Storfjorden: Hazard zoning and comparison with 3D laboratory experiments*. Unpublished work, NGI.

Hicks, E., Lindholm, C., Bungum, H., **2000**. *Stress inversions of earthquake focal mechanism solution from onshore and offshore Norway*. Norsk Geologisk Tidsskrift 80, 235 - 250.

Hoek, E., **2007**. *Practical rock engineering: Shear strenght of discontinuities*, Avaliable online at http://www.rocscience.com. Rocscience.

Hoek, E., Bray, J.W., **1981**. *Basic mechanics of slope failure*, in: Hoek, E., Bray, J.W. (Eds.), Rock Slope Engineering The Institution of Mining and Metallurgy, London.

Hoek, E., Read, J., Antonio, K., Chen, Z.Y., **2000**. *Rock slopes in Civil and Mining Engineering*, International Conference on Geotechnical and Geological Engineering. GeoEng2000, Melbourne.

Hungr, O., **1981**. *Dynamics of rock avalanches and other types of mass movement*, Ph.D. thesis, Amsterdam.

Hungr, O., Evans, S.G., **2004**. *Entrainment of debris in rock avalanches: An analysis of a long run-out mechanism*. Geological Society of America Bulletin 116, 1240 - 1252.

Høst, J., **2006**. *Store fjellskred i Norge*, in: uarbeid i samarbeid med: Norges geologiske undersøkelse, D.f.s.o.b., Statens landbruksforvaltning, Statens vegvesen, Jernbaneverket og Statens kartverk (Ed.), Trondheim.

InnovMetric, **2007**. *Polyworks V10 beginner's guide*. InnovMetric Software Inc. , Québec, Canada, p. 115.

ISRM, **1978**. *Suggested methods for determining hardness and abrasiveness of rocks*, in: Ulusay, R., Hudson, J.A. (Eds.), The Complete ISRM Suggested Methods for Rock Characterization, Testing and Monitoring:1974-2006. ISRM & ISRM Turkish National Group.

ISRM, **2007a**. *Part 1: Suggested Methods for Determining Compressive Strenght and Deformability of Rock Materials*, in: Ulusay, R., Hudson, J.A. (Eds.), The Complete ISRM Suggested Methods for Rock Characterization, Testing and Monitoring:1974-2006. ISRM & ISRM Turkish National Group, p. 137.

ISRM, **2007b**. *Part 2: Suggested Method for Determining Deformability of Rock materials in Uniaxial Compression*, in: Ulusay, R., Hudson, J.A. (Eds.), The Complete ISRM Suggested Methods for Rock Characterization, Testing and Monitoring:1974-2006. ISRM & ISRM Turkish National Group, pp. 138 - 140

Jaboyedoff, M., **2003**. *Conefall - User´s guide*, in: Quanterra (Ed.), Open - Report - Soft - 01, Lausanne, p. 15.

Jaboyedoff, M., Baillifard, F., Couture, R., Derron, M.H., Locat, J., Locat, P., **2005**. *Coupling of kinematic analysis and sloping local base level criterion for large slope instabilites and large rockslides hazard assessment - a GIS approach*, in: Hungr, O., Fell, R., Couture, R., Eberhardt, E. (Eds.), Landslide Risk Management: Proceeding of the International Conference on Landslide Risk Management Taylor & Francis Group, London, Vancouver, pp. 615 - 622.

Jaboyedoff, M., Baillifard, F., Couture, R., Locat, J., Locat, P., **2004**. *Toward preliminary hazard assessment using DEM topopgraphic analysis and simple mechanical modeling by means of sloping*

local base level, in: Lacerda, W.A., Fontoura, A.B., Ehrlich, M., Sayão, A. (Eds.), Landslides: Evaluation and Stabilization. Taylor & Francis, London.

Jaboyedoff, M., Derron, M.H., **2005**. *A new method to estimate the infilling of alluvial sediment of flacial valleys using a sloping local base level*. Geogr. Fis. Dinam. Quat. 28, 37 - 46.

Jaboyedoff, M., Labiouse, V., **2003**. *Preliminary assessment of rockfall haard based on GIS data*, 10th International Congress on Rock Mechanics ISRM 2003 - Technology roadmap for rock mechanics. South Africa Institute of Mining and Metallurgy, Johannesburgh, South Africa, pp. 573 - 578.

Jennings, J.E., **1970**. *A mathematical theory for the calculation of the stability of open cast mines*, in: van Rensburg, P.W.J. (Ed.), Planning Open Pit Mines. Sout African Institute of Mining and Metallurgy, Johannesburg, pp. 87 - 102.

Jibson, R.W., **1994**. *Using landslides for Palaeoseismic analysis*, in: McCalpin (Ed.), Paleoseismology. Academic press, pp. 397 - 438.

Jibson, R.W., **2011**. *Methods for assessing the stability of slopes during earthquakes - A retrospective*. Engineering Geology 122 43 - 50.

Jørstad, F., **1965**. *Fjellskredet ved Tjelle*. Naturen Vol. 80, 323 - 333.

Jørstad, F., **1968**. *Waves generated by landslides in Norwegian fjords and lakes*, Norwegian Geotechnical Institute, Oslo, pp. 13-32.

Kanji, M.A., **2004**. *Geologic Factors in Slope Stability*, in: Ortigao, J.A.R., Sayao, A.S.F.J. (Eds.), Handbook of Slope Stabilisation. Springer-Verlag, pp. 5 - 25.

Keefer, D.K., **1984**. *Landslides caused by earthquakes*. Geological Society of America Bulletin 95, 406 - 421.

Krabbedam, M., Dewey, J.F., **1999**. *Exhumation of UHP rocks by transtension in the western Gneiss Region, Scandinavia Caledonides*, in: Holdsworth, R.E., Strachan, R.A., Dewey, J.F. (Eds.), Continental Transpressional and Transtensional Tectonics. Spec. Publ. - Geologial Society, London, pp. 159 - 181.

Kveldsvik, V., Nilsen, B., Einstein, H.H., Nadim, F., **2007**. *Alternative approaches for analyses of a 100 000 m3 rock slide based on Barton - Bandis shear strenght criterion*. Landslides Vol. 5, 161 - 176.

Köthe, R., **2000**. *Definitions: DTM etc.* Scienic landscapes,.

Loftesnes, K., **2010**. *Svaddenipun, Rjukan - Stability analysis of potentially unstable mountainside*, Department of Geology and Mineral Resources Engineering. NTNU, Trondheim.

Lorig, L., **1999**. *Lessons learned from slope stability studies*, in: Detournay, C., Hart, R. (Eds.), FLAC and Numerical Modeling in Geo- mechanics (Proceedings of the Conference), Minneapolis, pp. 17 - 21.

Lutro, O., Thorsnes, T., Tveten, E., **1996**. *Berggrunnsgeologiskkart M 1:250000*. NGU, Trondheim.

Manfredinim, G., Martinetti, S., Ribacchi, R., **1975**. *Inadequacy of limiting equilibrium methods for rock slopes design*, Design Methods in Rock Mechanics, Proceeding of the 16th Symposium on Rock Mechanics. American Society of Civil Engineers, University of Minnesota, Minneapolis, pp. 35 - 43.

Mora, P., Baldi, P., Casula, G., Fabris, M., Ghirotti, M., Mazzini, E., Pesci, A., **2003**. *Global Positoning Systems and digital photogrammetry for the monitoring of mass movements: application to the Ca'di Malta landslide (northern Apennines, Italy).* Engineering Geology 68 (1-2), 103 - 121.

Moraes, R., **2011**. *Numerical codes used to model failure in large fractured scale and jointed rock slopes in hydropower projects*, 6th International conference on dam engineering, Lisbon.

Morsing, C., **1756**. *En kortileg beskrivelse over Jordskiælvet, og Fieldets Nedfald Som skede udj Nesset Præstegiæld i Romsdahls Provstie, og Trondhiems Stift udj Norge, nest afvigte Aar, Natten til dend 23 February 1756.* Norsk Historisk Kjedskrift Institutt, København.

Myrvang, A., **2001**. *Bergmekanikk.* Institutt for geologi og bergmekanikk, NTNU, Trondheim.

Nilsen, B., **2000**. *New tends in rock slope stability analyses* Bulleting Eng Geol Env 58, 173 - 178.

Nilsen, B., **2012**. *Personal communication about phase2*, Trondheim.

Nilsen, B., Broch, E., **2009**. *Ingeniørgeologi-berg grunnkurskompendium.* NTNU, Trondheim.

Nilsen, B., Lindstrøm, M., Mathiesen, T.K., Holmøy, H.K., Olsson, R., Palmstrøm, A., **2011**. *Veileder for bruk av Eurocode 7 til bergteknisk prosjektering*, in: bergmekanikkgruppe, N. (Ed.), p. 7.

Nordgulen, Ø., Andresen, A., **2007**. *The Western Gneiss Region*, in: Ramberg, I.B., Bryhni, I., Nøttvedt, A., Ragnes, K. (Eds.), The Making of a land - Geology of Norway. Geological Society og Norway, Trondheim, pp. 112 - 118.

NORSAR, **2010**. *Database of earthquakes in Møre & Romsdal between 1981 - 2010*. NORSAR, Online database: http://www.jordskjelv.no.

NTNU, **2009**. *Procedure for determining input parameters for Barton-Bandis joint shear strenght formulation*, Report from department of geology and mineral resources engineering NTNU, Trondheim.

Oppikofer, T., **2009**. *Detection, analysis and monitoring of slope movements by high-resolution digital elevation models*, Faculty of Geosciences and Environment Université de Lausanne (UNIL), Lausanne, p. 183.

Oppikofer, T., **2012**. *Personal communication: Reconstruction of Tjellefonna topography using PolyWorks and SLBL. Guidings of volume estimations.*, Trondheim.

Oppikofer, T., Jaboyedoff, M., Pedrazzini, A., Derron, M.H., Blikra, L.H., **2011**. *Detailed DEM analysis of a rockslide scar to characterize the basal sliding surface of active rockslides*. Journal of Geophysical research Vol. 116.

Pascal, C., Roberts, D., Gabrielsen, R.H., **2010**. *Tectonic significance of present-day stress relief phenomena in formerly glaciated regions*. Journal of the Geological Society, 363 - 371.

Popescu, M.E., **2002**. *Landslide Causal Factors and Landslide Remedial Options*, Proceedings 3rd International Conference on Landslides, Slope Stability and Safety of Infra-Structures, Singapore, pp. 61-81.

Redfield, T.F., **2012**. *Personal communication about sub-horizontal fault mapped at Tjellefonna*, Trondheim.

Redfield, T.F., Osmundsen, P.T., **2009**. *The Tjellefonna fault system of Western Norway: Linking late-Caledonian extension, post-Caledonian normal faulting, and Tertiary rock column uplift with the landslide-generated tsunami event of 1756*. Tectonophysics 474, 106 - 123.

Redfield, T.F., Osmundsen, P.T., Gradmann, S., Bauck, S.M., Ebbing, J., Nasuti, A., **2011**. *TopoScandiaDeep Field Trip, Tectonic Topography of Norway`s MTFC*. Geological Survey of Norway, Trondheim, p. 47.

Rocscience, **2009**. *2D Finite Element Modelling Excavation in Blocky Rock Masses using Phase2*, American rock mechanics association. ARMA, Asheville.

Rocscience, **2011**. *Phase2 online user manual*, Downloaded from http://www.rocscience.com/downloads/phase2/webhelp/phase2.htm.

Røsjø, B., **2005**. *Norges vakreste trussel*, GEO. GeoPublishing AS.

Saintot, A., Pascal, C., **2010**. *A contribution to the kinematics of the Møre-Trøndelag Fault Complex (Western Norway)*. Geophysical Research Abstracts Vol. 12, 1.

Sandøy, G., **2011a**. *Engineering Geological Laboratory Methods - TGB4505*. NTNU, Trondheim, p. 44.

Sandøy, G., **2011b**. *Tjellefonna - Mapping of factors affecting rock slope stability*, Department of Geology and Mineral Resources Engineering NTNU, Trondheim.

Sandøy, T., **2011c**. *Use of remote sensing methodology in assessing landslide susceptibility at the upstream catchment of Tamakoshi 3 hydroelectric project, Nepal*, Department of Geology and Mineral Resources Engineering NTNU, Trondheim.

Scheldt, T., **2002**. *Comparison of continuous and discontinuous modelling for computational rock mechanics*. Norwegian University of Science and Technology, Trondheim.

Schøning, G., **1778**. *Reise igiennem en Deel af Norge i de Aar 1773 - 75*, in: Utg. 1778 og nye utg. Thr. 1910 (Ed.).

Seed, H.B., **1979**. *Considerations in the eartquake-resistant design of earth and rockfill dams*. Geotechnique 29, 215 - 263.

SeNorge.no, **2011**. *Weather data from Eresfjorden, delivered by Meterologisk Institutt*.

Séranne, M., **1992**. *Late Paleozoic kinematics of the Møre - Trøndelag Fault Zone and adjacent areas, central Norway*. Norsk Geologisk Tidsskrift 72, 141 - 158

Sheorey, P.R., **1994**. *A theory for in-situ stresses in isotropic and transversely isotropic rock*. International Journal of Rock Mechanics and Mining Sciences & Geomechanics Abstracts 31 (1), 23 - 34.

Sherard, J.L., Woodward, R.J., Gizienski, S.F., Clevengerm, W.A., **1963**. *Earth and eart-rock dams*. John Wiley and Sons, New York.

Statens Kartverk, **2011**. *Norges kart over Tjelle*.

Stead, D., Eberhard, E., Coggan, J.S., **2006**. *Developments in the characterization of complex rock slope deformation and failure using numerical modelling techniques*. Engineering Geology 217 - 235.

Strahler, A.H., Strahler, A., **2002**. *Introduction Physical Geography*.

Svendsen, G., Werswick, K., **1961**. *Tjeldefjellet går ut*, Fjellene dreper. Tiden Norsk Forlag, Oslo, pp. 83 - 85.

Terzaghi, K., **1950**. *On the nature of reservoir-induced seismicity*. Pure and Applied Geophysics 150 (3), 473 - 492.

Terzaghi, K., **1962**. *Stability of Steep Slopes on Hard Unweathered Rock*. Géotechnique Vol. 12, 251 - 270.

USGS, **2012**. *The Ricther Magnitude Scale*, in: http://earthquake.usgs.gov/learn/topics/richter.php (Ed.). United States Geological Survey`s (USGS).

Varnes, D.J., **1978**. *Slope movement types and processes*, in: Robert, L.S. (Ed.), Landslides, Analysis and Control. Transportation Research Board, Washington, pp. 11 - 33.

Watts, L.M., **2001**. *The Walls Boundary Fault Zone and the Møre-Trøndelag Fault Complex: a Case Study of Two Reactivated Fault Zones*. University of Durham, Durham, p. 550.

Willie, D.C., Mah, C.W., **2004**. *Rock slope engineering: civil and mining* Spon Press, London.

Wines, D.R., Lilly, P.A., **2003**. *Estimated of rock joint shear strength in part of the Fimiston open pit operation in Western Australia*. Internastional Journal of Rock Mechanics & Mining Sciences, 929 - 937.

Wyllie, D.C., Mah, C.W., **2004**. *Rock Slope Engineering. Civil and Mining.* Spon Press, Taylor and Francis Group.

Wyrwoll, K.H., **1977**. *Causes of rock-slope failure in a cold area: Labrador-Ungava*. Geological Society of America Reviews in Engineering Geology 3, 59 - 67.

11. Appendix

Appendix 1: Field results and estimations of Barton-Bandis parameters

Appendix 2: RocLab results of instantaneous friction angle and cohesion(rock mass)

Appendix 3: Calculation of instantaneous friction angle and cohesion (joints)

Appendix 4: Estimation of joint stiffness of J1 and J5

Appendix 5: Volume calculations

Appendix 6: Uploaded Phase^2 data files

Appendix 1:
Field results and estimations of Barton-Bandis parameters

Estimation of r/R

Joint set : J1				Joint set: J5			
r	r_corr	R	R_corr	r	r_corr	R	R_corr
J1/50		J1/60		J5/20		J5/11	
48	**49**	52	**55**	38	**34**	50	**52**
45	**44**	52	**55**	37	**32**	51	**54**
42	**39**	52	**55**	33	**26,5**	43	**41**
40	**36**	52	**55**	33	**26,5**	44	**42,5**
40	**36**	52	**55**	33	**26,5**	46	**46**
39		48		32		51	
38		48		32		46	
36		48		30		45	
35		42		30		48	
32		40		28		47	
J1/50		J1/50		J5/20		J5/11	
44	**43**	50	**52**	42	**39**	52	**55**
44	**43**	49	**51**	36	**31**	50	**52**
42	**39**	48	**49**	30	**22**	49	**51**
42	**39**	48	**49**	36	**31**	49	**51**
42	**39**	46	**45**	28	**20**	48	**49**
41		46		30		48	
38		46		30		47	
36		44		32		46	
35		43		20		46	
34		42		22		45	

40,6	**40,7**	48,5	**52,1**	33,2	**28,9**	47,9	**49,4**

RESULTS:

	r/R corr	ϕr
J1	**0,78119**	25
J5	**0,5846**	29

Estimation of JRC

Joint set:	**J1**			
L [m]:	A[mm]:	Direction:	JRC	Guideline_JRC:
0,5	6	p.dipdir	5	5,6: 8 - 12
0,5	9	p.strike	8	
0,5	7	45	6	
0,5	8	45	7	
0,3	4	p.strike	5,5	5: 8 - 10
0,3	3	p.dipdir	4	
0,3	4	45	5,5	
0,2	3	45	6	
		Mean	**5,9**	

Joint set:	**J5**			
L [m]:	A [mm]:	Direction:	JRC	Guideline_JRC:
0,3	4	p.strike	5,5	4: 6 - 8
0,1	2	p.dipdir	8	
0,25	5	45	8	
0,2	2	45	4	
0,3	8	p.strike	11	5: 8 - 10
0,2	7	p.dipdir	14	
0,3	10	45	14	
0,3	5	45	7	
		Mean	**8,9**	

RESULTS:

	JRC
J1	**5,9**
J5	**8,9**

Estimation of JCS

Schmidt hardness

Joint set: **J1**			
J1/60		J1/50	
54	50	55	46
54	50	50	45
53	48	50	45
52	48	49	44
52	48	48	44
52	48	48	44
52	44	48	44
52	42	46	43
52	40	46	42
51	38	46	42

Joint set: **J5**	
J5/11	
51	47
51	47
50	47
50	46
49	46
48	46
48	46
48	45
48	44
47	43

Mean:	J1	J5
Sch_hardness	48,87	49,0
JCS [MPa]	**155**	**150**

Appendix 2:
RocLab results of instantaneous friction angle and cohesion (rock mass)

Hoek-Brown Classification
  intact uniaxial comp. strength (sigci) = 161 MPa
  GSI = 50   mi = 26   Disturbance factor (D) = 0.5
  intact modulus (Ei) = 63000 MPa

Hoek-Brown Criterion
  mb = 2.404   s = 0.0013   a = 0.506

Mohr-Coulomb Fit
  cohesion = 8.800 MPa   friction angle = 33.64 deg

Rock Mass Parameters
  tensile strength = -0.085 MPa
  uniaxial compressive strength = 5.528 MPa
  global strength = 32.853 MPa
  deformation modulus = 9257.35 MPa

sign=0.9795,sigtau=2.756
c=0.885,phi=62.36

Shear stress (MPa)

0

Figure A1: Conversion the Hoek-Brown parameters for the Tjellefonna rock mass (granitic to granodioritic gneiss).

Appendix 3:
Calculation of instantaneous friction angle and cohesion (joints)

Barton-Bandis results:

	J1	J5
φb	29	29
r5/R5	0,781190019	0,584599797
JRC	5,9	8,9
JCS	155	150
φr	25	21
PHIR (φr)	25	21
JRC	5,9	8,9
JCS	155	150
SIGNMIN	3,15828E-06	0,003709793

Instantanceous cohesion and friction:
Cell formulas:
Hoek (2007)

J1				
Normal stress [Mpa] SIGN	Shear strenght [Mpa] TAU	dTAU sSIGN (DTDS)	φ [degrees] (PHI)	c [Mpa] (COH)
0,8	0,628	0,712	35,465	0,058

J5				
0,8	0,928	1,002	45,044	0,127

RESULTS:

	φ [degrees]	c [Mpa]
J1	35,465	0,058
J5	45,044	0,127

Appendix 4:
Estimation of joint stiffness of J1 and J5

The joint stiffness (normal and shear) where estimated according to Rocscience (2011), while the rock mass shear modulus (G_m) and intact rock mass shear modulus (G_i) following equations found in Myrvang (2001).

The used equations are listed below in Table A4.1, and overview of the joint stiffness results in Table A4.2.

Table A4.1: Equations used to estimate stiffness and shear modulus.

Normal stiffness:	$$K_n = \frac{E_i \cdot E_m}{L(E_i - E_m)}$$
Shear stiffness:	$$K_s = \frac{G_i \cdot G_m}{L(G_i - G_m)}$$
Rock mass shear modulus:	$$G_m = \frac{E_m}{2(1 + v)}$$
Intact rock shear modulus:	$$G_i = \frac{E_i}{2(1 + v)}$$

Table A4.2: Calculated results of joint stiffness and shear modulus.

	J1	J5	
Poissons ratio (v)	0,21	0,21	
2 (1+v)	2,42	2,42	
Gm (MPa)	3825,4	3825,4	
Gi (MPa)	26033,1	26033,1	
Em (MPa)	9257,4	9257,4	
Ei (MPa)	63000	63000	
Average spacing (m)	1,5	5	
Kn (Mpa/m)	7234,6	2170,4	*Normal stiffness*
Ks (Mpa/m)	2989,5	896,9	*Shear stiffness*

Appendix 5:
Volume calculations

Volum: Tjellefonna reconstructed and scar deposits

	0	-0,00572	-0,006929	-0,01238
Reconstructed:				
Scar_deposits:	5335600	5669700	5702700	6066000
0	271 400	271 400	271 400	271 400
-0,05161	1 649 800	1 649 800	1 649 800	1 649 800
-0,05882	2 045 600	2 045 600	2 045 600	2 045 600
-0,08159	3 182 800	3 182 800	3 182 800	3 182 800

	-0,01238	6066000
	-0,08159	3 182 800
	tot	9248800

Not possible: scar_deposits c=0

Volum: Deposits fjord and onshore

	0	-0,0066	-0,0098	-0,01312	-0,01646	-0,01982	-0,02
Deposits fjord:							
Deposits onshore:	2942400	3 923 800	4 640 800	5678100	7222000	11470700	12652200
0	1 650 800	1 650 800	1 650 800	1 650 800	1 650 800	1 650 800	1 650 800
-0,05161	4 665 100	4 665 100	4 665 100	4 665 100	4 665 100	4 665 100	
-0,05882	5 349 800	5 349 800	5 349 800	5 349 800	5 349 800	5 349 800	
-0,08159	7 562 000	7 562 000	7 562 000	7 562 000	7 562 000	7 562 000	

	-0,0066	3 923 800
	-0,08159	7 562 000
	tot	11485800

Not possible: deposits and fjord c=0

Volume total: Tjellefonna reconstructed

	0	-0,00572	-0,006929	-0,01238
Reconstructed:				
Scar_deposits:	5335600	5669700	5702700	6066000
0	5 607 000	5 941 100	5 974 100	6 337 400
-0,05161	6 985 400	7 319 500	7 352 500	7 715 800
-0,05882	7 381 200	7 715 300	7 748 300	8 111 600
-0,08159	8 518 400	8852500	8 885 500	9 248 800

Volume total: Deposits on fjord + onshore

	0	-0,0066	-0,0098	-0,01312	-0,01646	-0,01982	-0,02
Deposits fjord:							
Deposits onshore:	2942400	3 923 800	4 640 800	6066000	7222000	11470700	12652200
0	4 593 200	5 574 600	6 291 600	7 328 900	8 872 800	13 121 500	14303000
-0,05161	7 607 500	8 588 900	9 305 900	10 343 200	11 887 100	16 135 800	17317300
-0,05882	8 292 200	9 273 600	9 990 600	11 027 900	12 571 800	16 820 500	18002000
-0,08159	10 504 400	11 485 800	12 202 800	13 240 100	14 784 000	19 032 700	20214200

Volume increas of 25 % : Total volume of fjord and onshore deposits

Criterion: deposits onshore have a best fit when equal -0.08159

0 Deposits fjord:

Deposits onshore:	0	-0,0066	-0,00982	-0,01312	-0,01646	-0,01982	-0,02
0	0,82	0,99	1,12	1,31	1,58	2,34	2,55
-0,05161	1,09	1,23	1,33	1,48	1,70	2,31	2,48
-0,05882	1,12	1,26	1,35	1,49	1,70	2,28	2,44
-0,08159	1,23	1,35	1,43	1,55	1,74	2,23	2,37

-0,00572 Deposits fjord:

Deposits onshore:	0	-0,0066	-0,00982	-0,01312	-0,01646	-0,01982	-0,02
0	0,77	0,94	1,06	1,23	1,49	2,21	2,41
-0,05161	1,04	1,17	1,27	1,41	1,62	2,20	2,37
-0,05882	1,07	1,20	1,29	1,43	1,63	2,18	2,33
-0,08159	1,19	1,30	1,38	1,50	1,67	2,15	2,28

-0,006929 Deposits fjord:

Deposits onshore:	0	-0,0066	-0,00982	-0,01312	-0,01646	-0,01982	-0,02
0	0,77	0,93	1,05	1,23	1,49	2,20	2,39
-0,05161	1,03	1,17	1,27	1,41	1,62	2,19	2,36
-0,05882	1,07	1,20	1,29	1,42	1,62	2,17	2,32
-0,08159	1,18	1,29	1,37	1,49	1,66	2,14	2,27

-0,01238 Deposits fjord:

Deposits onshore:	0	-0,0066	-0,00982	-0,01312	-0,01646	-0,01982	-0,02
0	0,72	0,88	0,99	1,16	1,40	2,07	2,26
-0,05161	0,99	1,11	1,21	1,34	1,54	2,09	2,24
-0,05882	1,02	1,14	1,23	1,36	1,55	2,07	2,22
-0,08159	1,14	1,24	1,32	1,43	1,60	2,06	2,19

Appendix 6:
Uploaded Phase^2 data files

The Phase^2 results files used in this master thesis are digital uploaded in DAIM (Phase2_results.zip).